EURASIAN PHYSICAL TECHNICAL JOURNAL

phtj.buketov.edu.kz

Journal Founder:

E.A. BUKETOV KARAGANDA UNIVERSITY

Е.А.БӨКЕТОВ АТЫНДАҒЫ ҚАРАҒАНДЫ УНИВЕРСИТЕТІ

КАРАГАНДИНСКИЙ УНИВЕРСИТЕТ имени Е.А.БУКЕТОВА

Eurasian Physical Technical Journal, 2022, Vol. 19, No. 3(41)

CONTENTS

Dear authors and readers!
Dear Colleagues!

Traditionally, in the Preface we inform you about the scientometric indicators achieved at this moment by the "Eurasian Physical Technical Journal".

Indeed, the ranking of the Eurasian Physical Technical Journal as a peer-reviewed scientific journal indexed in the Scopus database continues to strengthen. As of September 5, 2022, the CiteScoreTracker is 1.0. Now the dynamics of this indicator, which depends on the publication activity of authors and readers, can be observed monthly on our website - https://phtj.buketov.edu.kz/index.php/EPTJ/index.

Since 2022, all stages of preparing articles to publication in "Eurasian Physical Technical Journal" (uploading and receiving the manuscript and all the necessary information, examination, peer review and literary editing) are carried out online. The site contains all the necessary instructions for authors on the correct input of the manuscript necessary materials, strict observance of which contributes to the publication quality.

The work carried out by members of the editorial board and programmers made it possible to upload in the Archives published in the period 2000-2022 articles not only in PdF-format, but also in a convenient interactive form with reference data in 3 languages. So, under preparing an article for publication in another journals, authors using the "How to cite" option can quickly and without errors convert the data of their article according to 10 standard formats of bibliographic references.

In this issue, the readers are offered the results of scientific research aimed at solving modern topical problems in physics and technology. Practice shows that without optimization of production processes, development and implementation of efficient technologies, it is impossible to achieve any scientific and technological progress.

The Materials Science section presents the results with practical importance, for example: the method of possible variation of the "pore diameter of copper oxide from several tens of nanometers to hundreds of microns" with a simultaneous change in film thickness; technology for obtaining bulk nanostructured materials; the established fact that "the graphene nanoribbon and the electric field determine the self-assembly of molecules of nematic liquid crystals in the biaxial state"; regularities of "temporal kinetics of the electronic subsystem of yttrium iron garnet after exposure to fast heavy ions"; method of "magnetron sputtering for deposition of protective high-entropy multi-element coatings", etc.

Articles of the Energy section are devoted to solving the most urgent problems of modern energy and their environmental aspects, such as the development of: a way to reduce the carbon content in gas emissions by using methanol as a fuel; a method for improving the photovoltaic parameters of solar cells by influencing TiO_2 on the efficiency of a functionalized dye; a new efficient version of the Bi-Darrieus type wind turbine, which makes it possible to significantly increase the coefficient of wind energy utilization; the method of cooling the corium to ensure effective localization of the melt of the core of a nuclear reactor.

Important technical and innovative developments are given in the next 2 sections. The workability and wear resistance of triboconnections, the wear of which depends on the conditions of contact interaction and the state of the surface layer, are analyzed. In order to ensure the transmission of messages without distortion and loss of information due a result of fractal analysis of the model network, an efficient cluster router based on eccentricity has been developed and its information dimensions have been calculated.

The use of the FOCUS CPM software allowed the authors to fairly accurately assess the influence of the design features of the devices on their electro-optical characteristics.

We are grateful to our authors for the provided scientific papers with the importance results that undoubtedly will be of interest to scientists, teachers, researchers, doctoral students and undergraduates.

We are appreciated to qualified and valuable our reviewers work, which contributes to the quality assurance of articles.

We will be glad to see you among our readers and authors of the next issues.

Best wishes,
Editor-in-chief, professor Sakipova S.E.
September, 2022

INVESTIGATION OF THE INFLUENCE OF ANODIZING MODES OF COPPER OXIDE FILMS ON THEIR MORPHOLOGY

Smirnov V.[1], Kadir M.[2], Alpysbayeva B.[2], Nemkayeva R.[2]

[1]Forschungszentrum Jülich (FZJ), Germany

[2]al-Farabi Kazakh National University, Almaty, Kazakhstan, kadir.meruyert@gmail.com

This work presents experimental data on the surface morphology of Cu_2O films obtained by single-stage electrochemical anodization. The process was carried out at a constant applied potential of 50V and at a temperature of 13°C (90 seconds) in an electrolyte based on phosphoric acid. During the experimental work, the optimal synthesis parameters were determined. The morphology of copper porous films was studied using atomic force microscopy Ntegra Therma. The effect of the main anodizing parameters on the morphology of the nanoporous Cu_2O film was investigated. According to the results of experimental work, it was found that, depending on the parameters of the anodizing process, it is possible to vary the pore diameter of copper oxide from several tens of nanometers to hundreds of microns, while it is also possible to change the film thickness.

Keywords: nanoporous, copper oxide, electrochemical anodizing, phosphoric acid, atomic force microscopy.

Introduction

Recently, one of the most rapidly developing scientific areas is the production of new nanostructured materials. Such materials include nanomaterials based on copper oxide. Copper oxide is a narrow bandgap semiconductor material with a high absorption coefficient in the visible region. Low cost, environmental friendliness, richness of resources makes copper oxide promising for use in sensors [1], hydrogen production [2], energy conversion [3, 4], supercapacitors [5], semiconductor catalysis [6, 7], and biosensors [8, 9], etc.

In connection with the method of synthesis of nanostructured copper oxide, the direction of research for optical and electronic devices increases significantly [10]. Numerous methods have been used to synthesize Cu_2O nanostructures [11-13]. However, the above methods have their drawbacks such as expensive equipment, expensive reagents, harsh reaction conditions, uncontrolled structures, and complicated experimental setup.

Among the methods, the most effective is the anodizing process. Anodizing is a scalable, versatile, economical (technological equipment cost is low) method for obtaining oxide coatings for metals. In addition, by changing the main parameters of the anodizing process, such as electrolyte composition, etching voltage, and anodizing duration, it is possible to control the morphology and size of the copper oxide nanostructure [14, 15]. Recently, nanostructures of copper oxides have been synthesized based on the anodizing process [14-16]. For example, in [17], copper oxide nanostructures were synthesized by anodizing copper deposited on glass from tin oxide doped with fluorine, and the thickness of the deposited copper was 500 nm. In [18], nanostructured Cu_2O thin films with different morphologies were fabricated by anodizing in an ethylene glycol electrolyte containing 0.15M potassium hydroxide, 0.1M ammonium fluoride with 3 wt. % deionized water. In this study, a mechanism for the formation of a thin Cu_2O film was proposed and the effect of anodizing voltage and electrolyte temperature on morphology was investigated.

Using the anodizing process, Cu_2O nanostructures with different morphologies can be easily synthesized, which can help expand the scope of this material.

1. Experimental part

During the experimental work, a copper plate (99.61%) with a thickness of 40 μm was used as the starting material. The process of one-stage anodizing was carried out at a constant applied potential of 50V in an electrolyte of 0.4M H_3PO_4 at a temperature of T=13°C for 35-90 seconds. Before starting the anodizing process, the copper plate was preliminarily annealed in a muffle furnace at a temperature of T= 400°C for 60 minutes. The surface morphology of the nanoporous copper oxide was studied by Ntegra Therma (NT-MDT)

atomic force microscopy and scanning electron microscopy (Quanta 200i 3D FEI). To study porous copper films, we used a semicontact AFM and an NSG30 type cantilever. Elemental analysis was carried out on the basis of energy dispersive X-ray analysis (EDAX).

2. Results and discussion

The process of formation of a porous structure and the degree of ordering primarily depend on the chemical purity of the initial copper. To study the influence of the chemical purity of the initial copper on the structure of the obtained films, elemental analysis was carried out on a scanning electron microscope (fig. 1). Elemental analysis was carried out on the basis of energy dispersive X-ray spectroscopy. As the results of the analysis showed, the composition of the original copper plate contains oxygen impurities. Figures 2 (a, b, c) show the SEM image of copper before heat treatment, after thermal annealing at 400°C in the air, and after the anodizing process. As can be seen from figure 2 c, there will be much fewer areas with orders pores on the surface of copper films. Therefore, before carrying out studies on the production of copper oxide films, it is necessary to select a starting material with a high chemical purity.

a)   b)
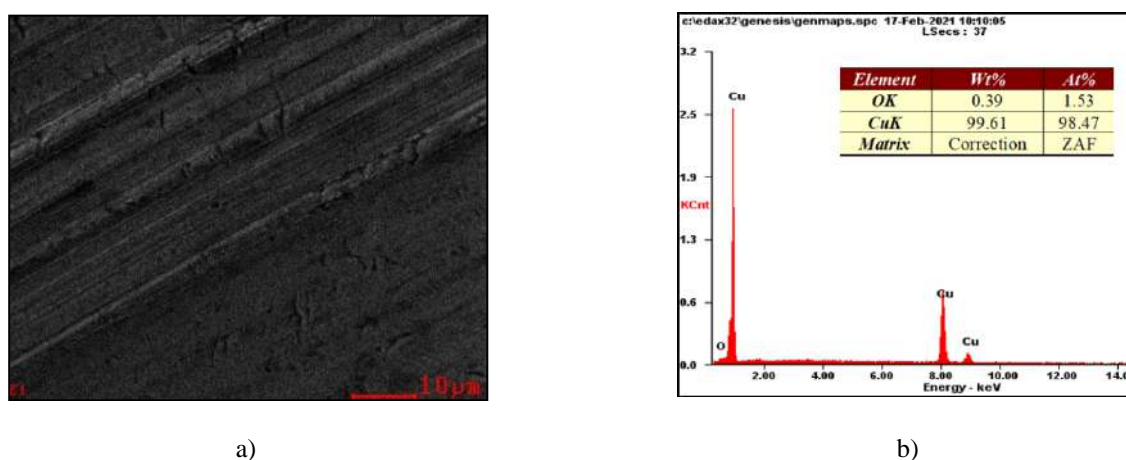
Fig. 1. Results of elemental analysis of a copper plate: a – SEM micrograph, b – EDX spectrum and table for the weight percent and atomic percent

a)   b)   c)
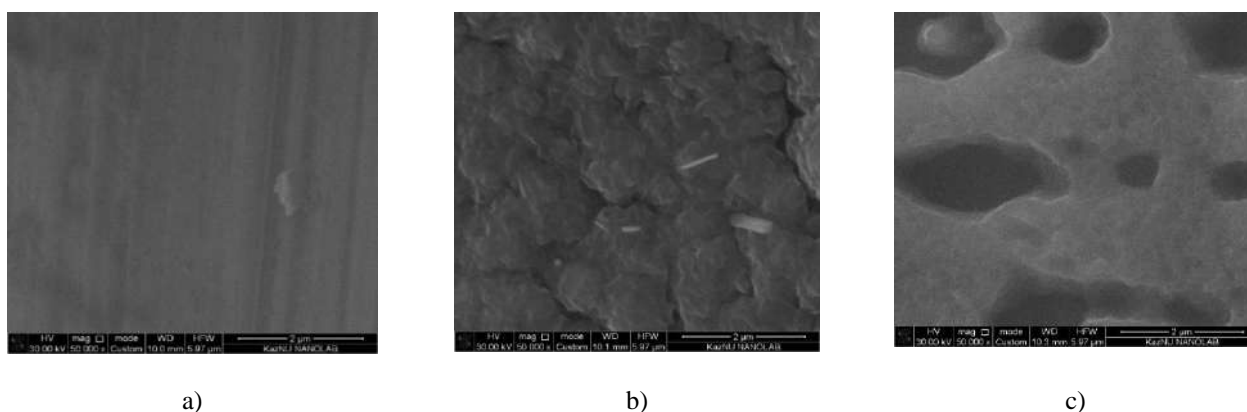
Fig. 2. SEM image of copper: a-pure; b-after the annealing process; c-after anodizing process

The main parameters affecting the structure of the synthesized Cu_2O are the temperature and time of the anodizing process, the composition of the electrolyte, and the applied voltage. Depending on the choice of electrolyte composition, primarily on the type of acid, it is possible to form pores with different pore sizes. As already noted, in the present work, porous copper oxide was obtained at a temperature of 13°C. Stabilization of the electrolyte temperature during the anodizing process is necessary in order to avoid local heating in the layer of electrolyte contact with the surface of the original copper. At sufficiently low temperatures, the electrolyte can freeze and the anodizing process slows down, which, accordingly, leads to a

slowdown in the formation of the pores themselves. Consideration must be given to the importance of temperature stabilization during the anodizing process. Voltage is another key parameter of the anodizing process that determines the porosity and the morphology of the nanostructured copper film. Anodizing at a voltage of 50 V, a nanoporous film is formed on the Cu wafer. At voltages above 50 V, a highly oriented porous film is formed [18]. In general, it should be noted that the porosity of the nanostructured film increases with an increase in the anodizing voltage. Figure 3 shows AFM images of porous copper after anodization, , where the pore size and their structural features can be estimated.
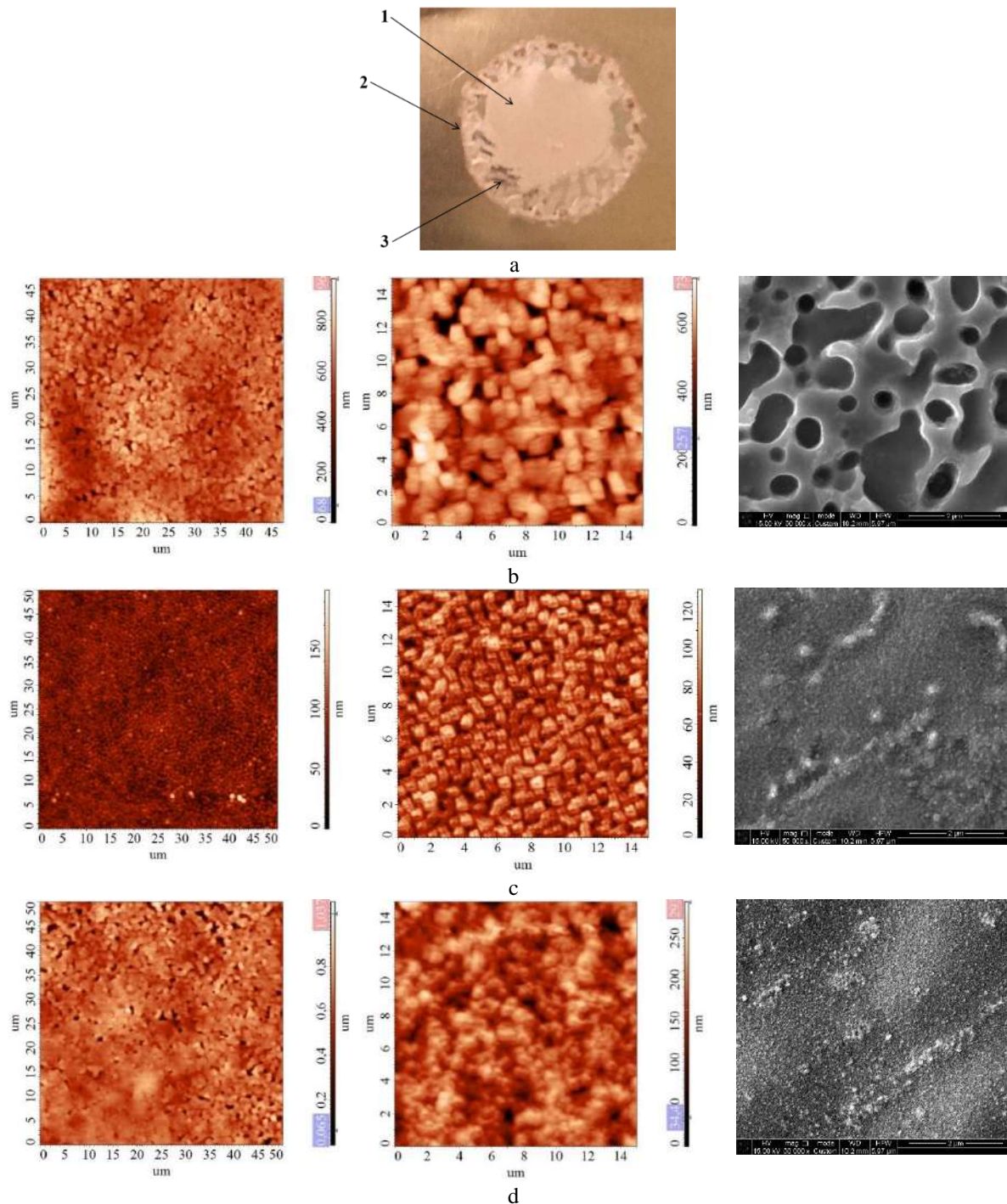
Fig. 3. AFM and SEM images of copper films after anodizing:
a-copper plate; b- matte area (a1); c - dark area (a2); d- oval area (edge, a3)

Figure 3a shows the sample itself, as can be seen from the figure, the anodizing process is unstable over the entire surface of the plate and, accordingly, have a different morphology (fig. 3 b, c, d). This may be due to different chemical bonds on the surface and in the volume of copper. In addition, experimental data show that the formation of a porous structure and the degree of ordering are affected by the chemical purity of copper. As a result of the study, it was found that porous structures begin to form on the copper surface and with different pore diameters, depending on the anodizing parameter. The pore diameters ranged from several tens of nm to hundreds of microns. Such porous structures are formed under the following anodizing process conditions: U = 50-100V, T = 13-16°C, t = 35 s, 60 s, 90 s.

Conclusion

Based on the results of the study, the following conclusions can be drawn:

1. Nanostructured copper oxide films were synthesized using single-stage electrochemical anodization in 0.4M H_3PO_4 electrolyte at a temperature of T=13°C at a voltage of 50 V.

2. Technological conditions for the synthesis of Cu_2O samples have been worked out. It was found that, depending on the parameters of the anodizing process, it is possible to control the thickness and vary the pore diameter from several tens of nm to hundreds of microns. The average thickness of the synthesized nanoporous films is 1 μm.

3. The surface morphology of the obtained samples was studied by atomic force microscopy and scanning electron microscopy. As the results of the study showed, the degree of pore ordering depends not only on the process parameters, but also on the chemical purity of the initial copper.

REFERENCES

1   Deng S., Tjoa V., Fan H.M., Tan H.R., Sayle D.C., Olivo M., Mhaisarkal S., Wei J., Sow C.H. J. Reduced Graphene Oxide Conjugated Cu_2O Nanowire Mesocrystals for High-Performance NO_2 Gas Sensor. *Journal of the American Chemical Society.* 2012. Vol.134, No.10, pp. 4905–4917, doi:10.1021/ja211683m.

2   De Jongh P.E., Vanmaekelbergh D., Kelly J.J.D. J. Photoelectrochemistry of Electrodeposited Cu_2O. *Journal of The Electrochemical Society*. 2000. Vol.147, No.2, pp. 486, doi:10.1149/1.1393221.

3   Musselman K.P., Wisnet A., Iza D.C., Hesse H.C., Scheu C., Macmanus-Driscoll J.L., Schmidt-Mende L. Strong Efficiency Improvements in Ultra-low-Cost Inorganic Nanowire Solar Cells. *Adv. Mater.* 2010, pp. 22:254-258, doi: 10.1002/adma.201001455.

4   Bhaumik A., Haque A., Karnati P., Taufique M., Patel R. and Ghosh K. Copper oxide based nanostructures for improved solar cell efficiency. *Thin Solid Films.* 2014, pp. 572, pp. 126–133, doi:10.1016/j.tsf.2014.09.056.

5   Dong X., Wang K., Zhao C., Qian X., Chen S., Li Z., Liu H., Dou S. J. Direct synthesis of RGO/Cu_2O composite films on Cu foil for supercapacitors. *Alloy. Compd.* 2014, pp. 586:745-753, doi:/10.1016/j.jallcom.2013.10.078.

6   Poreddy R., Engelbrekt C. and Riisager A. Catal. Sci. Technol. Copper oxide as efficient catalyst for oxidative dehydrogenation of alcohols with air. *Catalysis Science & Technology.* 2015. Vol.5, No.4, pp. 2467–2477, doi:10.1039/c4cy01622j.

7   Wang H.Y. and Fan C.G. Copper oxide nanostructures: Controlled synthesis and their catalytic performance. *Solid State Sciences*. 2013, pp.16, pp. 130–133, doi:10.1016/j.solidstatesciences.2012.11.009.

8   Xu L., Yang Q., Liu X., Liu J. and Sun X. One-dimensional copper oxide nanotube arrays: biosensors for glucose detection. *RSC Adv*. 2014. Vol.4, No.3, pp. 1449–1455, doi:10.1039/c3ra45598j.

9   Gao J., Li Q., Zhao H., Li L., Liu C., Gong Q. and Qi L. One-Pot Synthesis of Uniform Cu2O and CuS Hollow Spheres and Their Optical Limiting Properties. *Chemistry of Materials.* 2008. Vol.20, No.19, pp. 6263–6269, doi:10.1021/cm801407q.

10   Kar P., Farsinezhad S., Zhang X., Shankar K. Anodic Cu2S and CuS nanorod and nanowall arrays: preparation, properties and application in CO2 photoreduction. *Nanoscale,* 2014. Vol.6, No.23, pp. 14305–14318, doi:10.1039/c4nr05371k.

11   Khanehzaei H., Ahmad M.B., Shameli K., et al. Characterization of Cu@Cu2O Core Shell Nanoparticles Prepared in Seaweed Kappaphycus alvarezii Media. Int. *J. Electrochem. Sci*. 2015. Vol.10, pp. 404 – 413.

12   Wu X., Bai H., Zhang J., Chen F.E., Shi G. J. Copper Hydroxide Nanoneedle and Nanotube Arrays Fabricated by Anodization of Copper. *The Journal of Physical Chemistry B*. 2005. Vol. 109, No. 48, pp. 22836–22842, doi:10.1021/jp054350p.

13   Wang P., Wu H., Tang Y., Amal R., Ng Y.H. J. Electrodeposited Cu2O as Photoelectrodes with Controllable Conductivity Type for Solar Energy Conversion. *The Journal of Physical Chemistry C*. 2015. Vol.119, No.47, pp. 26275–26282, doi:10.1021/acs.jpcc.5b07276.

14   Allam N.K., Grimes C.A. Electrochemical fabrication of complex copper oxide nanoarchitectures via copper anodization in aqueous and non-aqueous electrolytes. *Materials Letters.* 2011. Vol.65, No.12, pp. 1949–1955, doi:10.1016/j.matlet.2011.03.105.

15   Mohammadpour A., Eltahlawy M., Martino A., Askar A.M., Kisslinger R., Fedosejevs R. and Shankar K. J. Optical Limiting in Cu/CuO Nanostructures Formed by Magnetic Field-Assisted Anodization. *Journal of Nanoscience and Nanotechnology.* 2017. Vol.17, No.7, pp. 5019–5023, doi:10.1166/jnn.2017.13309.

16   Shu X., Zheng H., Xu G., Zhao J., Cui L., Cui J., Qin Y., Wang Y., Zhang Y., Wu Y. The anodization synthesis of copper oxide nanosheet arrays and their photoelectrochemical properties. *Applied Surface Science.* 2017. pp.412, pp. 505–516, doi:10.1016/j.apsusc.2017.03.267.

17   Kar P., Khairy El-Tahlawy M., Zhang Y., Yassin M., Mahdi N., Kisslinger R., Thakur U.K., Askar A.M., Fedosejevs R. and Shankar K. J. Anodic copper oxide nanowire and nanopore arrays with mixed phase content: synthesis, characterization and optical limiting response. *Journal of Physics Communications.* 2017. Vol.1, No.4, pp. 045012, doi:10.1088/2399-6528/aa93a4.

18   Voon C.H., Lim B.Y., Gopinath S.C.B., Al-douri Y., Foo K.L., Md Arshad M.K., Ten S.T., Ruslinda A.R., Hashim U., Tony V.C.S. Fabrication of Cu_2O Nanostructured Thin Film by Anodizing. *Materials Science-Poland.* 2018. Vol.36, No.2, pp. 209-216, doi: 10.1515/msp-2018-003.

SEVERAL NOTES ON THE LATTICE THERMAL CONDUCTIVITY OF FRACTAL-SHAPED NANOPARTICLES

Shishulin A.V.[1,2*], Potapov A.A.[3,4], Shishulina A.V.[5,6]

[1]Pleiades Publ., Ltd., Moscow, Russia, chichouline_alex@live.ru
[2]G.A. Razuvaev institute of organometallic chemistry, Russian Academy of sciences, Nizhny Novgorod, Russia
[3]V.A. Kotel'nikov institute of radio engineering and electronics, Russian Academy of sciences, Moscow, Russia
[4]JNU-IREE RAS Joint Laboratory of Information Technology and Fractal Processing of Signals, Jinan University, Guangzhou, China
[5]R.E. Alekseev Nizhny Novgorod State technical University, Nizhny Novgorod, Russia
[6]N.I. Lobachevsky Nizhny Novgorod State University, Nizhny Novgorod, Russia

Using the additive technologies in the production of nanoparticle-fabricated three-dimensional materials has become one of the most promising ways of obtaining effective and low-cost thermoelectric energy converters. Nanostructuring provides a route to modifying selectively the transport properties which determine the materials thermoelectric efficiency. In this paper, we have shown one more effect which consists in a significant dependence of the contribution of lattice vibrations to the thermal conductivity coefficient of a nanoparticle (its reducing is required in practice) on its morphology for nanoparticles of a pure substance. The particle morphology has been specified by the values of its effective diameter, fractal dimension and surface roughness.Using nanoparticles of pure bismuth at low temperatures as an example, we have demonstrated a notable decrease in the lattice thermal conductivity in "complicating" the particle morphology. In the final section, we have presented methods of calculating characteristics of nanoparticle ensembles, the methodology of measuring the fractal dimension experimentally also being discussed.

Keywords: *thermoelectric materials, thermal conductivity, nanoparticles,phonons, fractal dimension.*

Introduction

Thermoelectric materials and energy converters on their basis have been an object of considerable interest among researchers in recent years [1]. The expanding field of their application includes energy generators which operate in extreme conditions (radioisotope thermoelectric generators for Voyager-2 and other space modules [1]), thermoelectric converters for utilizing the waste heat dispersed into environment [2], cooling and temperature-control facilities based on the Peltier effect, etc. [3]. Despite the intensive development of multiple approaches to obtain thermoelectric materials with promising properties based on low-dimension structures (nanofilms [4,5], quantum wires [6], etc.), highly-effective and low-cost thermoelectrics can be produced on the basis of 3D nanocrystalline structures [7,8]. The scheme which illustrates the performance of a typical thermoelectric converter is given in Fig. 1.
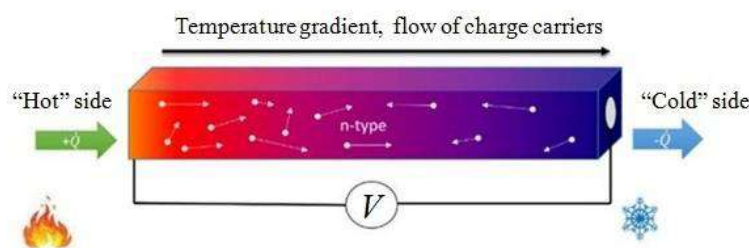
Fig.1. Schematic illustration of the performance of a typical thermoelectric converter. A thermoelectric device creates a voltage when there is a different temperature on each size of a thermoelectric material sample. At the atomic scale, an applied temperature gradient causes charge carriers in the material to diffuse from the "hot" side to the "cold" side.

The key characteristic parameter determining the materials thermoelectric efficiency is the dimensionless figure of merit, ZT, which can be expressed as a function of thermal conductivity κ, electrical conductivity σ and Seebeck coefficient α: $ZT = \alpha^2 \sigma \overline{T}/\kappa$ where $\overline{T}$ is the average temperature between the "hot" and "cold" sides of a thermoelectric converter and $\kappa \approx \kappa_{car} + \kappa_{ph}$ [1,2,7]. Here, κ_{car} and κ_{ph} are the contributions of charge carriers (electrons, holes) and phonons (crystal lattice vibrations) to the thermal conductivity, respectively (several other contributions, e.g. the ones of excitons or spin-orbit coupling, are neglected, being much lower). In every single material, as a rule, electrical conductivity σ and the contribution of carriers to the total thermal conductivity, κ_{car}, cannot be varied separately, and optimal thermoelectric properties can be obtained primarily through the reduction of the phonon contribution κ_{ph}. In nanostructured polycrystalline materials, κ_{ph} is generally decreased through the formation of multiple interfaces (grain boundaries) which scatter thermal phonons [9], add to this, the energy filtration of charge carriers at grain boundaries, which reduces the contribution of low-energy carriers to transport properties, results in an additional increase in the Seebeck coefficient [2]. Nanostructured polycrystalline thermoelectric materials can be produced using various technologies of up-to-date powder metallurgy, e.g. spark plasma sintering, selective laser sintering, selective laser melting, etc. [7,8].

It is necessary to mention that several effects manifesting themselves at the nanoscale provide additional "knobs" which allow tuning the properties of thermoelectric materials. For example, the phase equilibria in small-volume particles of stratifying solutions become morphology-dependent, being different from the ones of macroscopic-sized structures, which leads to the possibility of the formation of stable phases, the compositions of which are highly unstable in macroscale particles at the operation temperatures. As we have previously shown in [10,11] using the combination of thermodynamic [12] and *ab initio* [13] approaches, such phases correspond to much lower values of the phonon thermal conductivity coefficients favoring the growth of the thermoelectric figure of merit; we have also predicted the set of optimal morphological characteristics (as well as some other factors) which lead to reaching the minimum value of κ_{ph}. These effects have been interpreted as the implementation of several mechanisms of lowering the free energy of a nanoscale system, which can also be competitive in several cases leading to specific non-monotonous dependences of phase equilibria characteristics [14]. Despite the fact these effects are realized at the nanoscale particle sizes (available for the additive technologies, however) in the majority of cases, there is a broad class of systems with greater molecular masses in which such effects manifest themselves at characteristic sizes even several thousand times higher [15,16] (and should probably be called "small-amounts-of-matter effects" instead of "size effects" [17]).

In the present paper, we have shown for the first time another specific effect, which consists in additional decrease in the phonon contribution to the thermal conductivity coefficient, manifesting itself in nanoparticles even of pure substance. Physically, this effect is associated with an increase in the morphology-dependent fraction of surface atoms which have oscillation characteristics being different from the ones of atoms in the particle volume. The dependence of κ_{ph} on particle morphology has been constructed using nanoparticles of pure bismuth as an example. Bismuth (being either pure or alloyed with antimony) is considered to be one of the most efficient thermoelectric materials especially at low temperatures with a large set of possible application fields including space technologies. The obtained estimates combined with the ones in [10] show one more possible route to the more effective optimization of the thermoelectric performance of particle-fabricated nanoalloys.

1. Lattice thermal conductivity of nanoscale particles: the morphology matters

The specific properties of the substance in systems of a very small volume have been investigated by the scientific community since 1850: M. Faraday was the first to emit the idea that the melting temperature of extremely tiny particles should be smaller than the one for the bulk state [18]. A detailed review concerning unique properties of the substance at the nanoscale including the melting behavior can be found in Refs [18,19]. Here, in order to determine the morphology-dependent melting temperature of nanoparticles, we have used the model suggested by W.H. Qi and M.P. Wang [20]. Being experimentally verified for nanoparticles of pure bismuth, this model is based on the considerations of J.H. Rose *etal.* [21,22] on the

binding theory of solids which allow deriving the well-known empirical relation between melting temperature T_m and cohesive energy E_{coh} for pure metals: $T_m = 0.032 E_{coh}/k_B$ where k_B is the Boltzmann constant. According to the approach of W.H. Qi and M.P. Wang, the dependence of the nanoparticle melting temperature on the morphology can be described by the following equation: $T_m^{nano} = T_m^{bulk}\left(1 - 6kr_{at}/d_{eff}\right)$ where T_m^{nano} and T_m^{bulk} are the melting temperatures of a nanoparticle and the bulk material, respectively, r_{at} is the atomic radius and k and d_{eff} are the shape coefficient and the effective diameter of a nanoparticle (the diameter of a spherical nanoparticle of the same volume). The shape coefficient is the ratio between the surface area of the particle under consideration, A, and the surface area of the sphere of the same volume, A_0: $k = A/A_0$ (in details, such approach and its variants have been described in [12,23,24]). High values of shape coefficient k could be obtained, for example, in the case when the considered particles have the shapes similar to simple non-spherical geometric structures (for example, $k=1.49$ for a tetrahedron, $k=1.52$ for a cone, $k=3.20$ for a star icosahedron (an icosahedron with a tetrahedron at each face)) or structures extended in one direction (for example, values $k>2.00$ correspond to oblate spheroids with aspect ratio $a/b>5$ or to prolate spheroids with $a/b>3$). Moreover, high surface-to-volume ratios are also characteristic for particles of complicated and irregular shapes, in order to take into account their morphology, the notion of fractal geometry is often used [25]. According to the approach suggested by us in [26,27], the shape of a particle can be characterized by its fractal dimension D which correlates its volume V and surface area A: $A = CV^{2/D}$ where C is a numerical coefficient. For real irregular morphologies of materials structure elements, $D<3$ and is typically non-integer. The most classic examples of fractal structures are *worm-like*, *amoeba-like*, and *porcupine-like* ones [26] (see Fig. 2a). The formation of fractal-shaped structures is generic for many non-equilibrium processes [28].
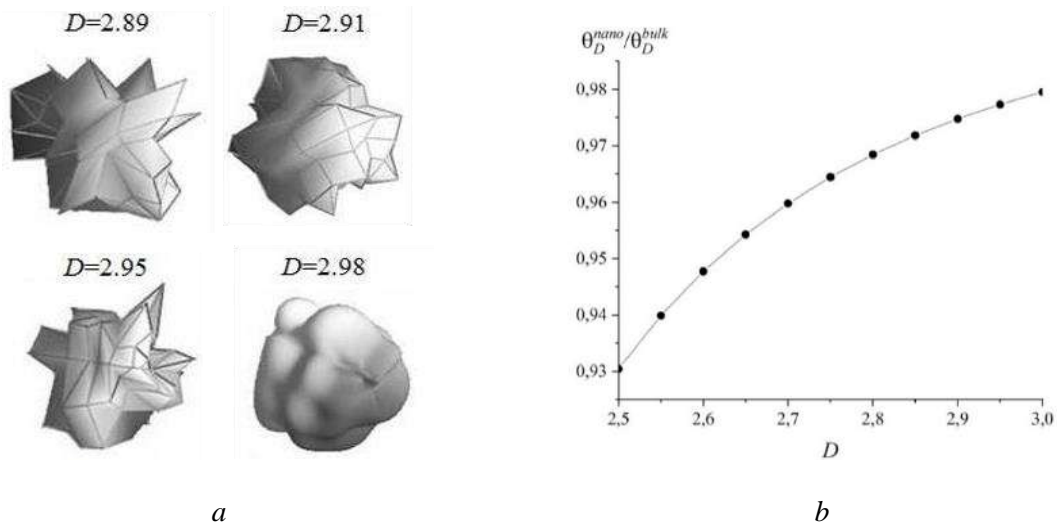
Fig 2. a) examples of "amoeba-like" and porcupine-like" fractal structures with various D; b) the dependence of relative Debye temperature $\theta_D^{nano}/\theta_D^{bulk}$ on the fractal dimension for a nanoparticle with d_{eff}=40 nm.

Melting temperature and temperature θ_D, at which all the modes of oscillations in the considered solid medium become excited (known as the Debye temperature), are interrelated according to the Lindemann criterion of melting [29]. This criterion is based on the statement that the root-mean-square amplitude of thermal oscillations at this temperature reaches a certain critical value which represents a constant fraction of the characteristic interatomic distance, δ_L, in the crystal lattice. δ_L is the so-called "Lindemann parameter", $\delta_L \in [0.15, 0.30]$. The Lindemann criterion can be mathematically formulated as follows [29]: $T_m = 4\pi^2 A \delta_L^2 a^2 k_B \theta_D / 4 N_A h^2$ where h is the Planck constant, a is the characteristic interatomic distance and A is the molar mass of the considered substance. Since the characteristic distances in the crystal lattice are independent on the size and shape of a particle when the particle size does not exceed several nanometers,

we obtain $\theta_D \sqcup T_m^{1/2}$, $\theta_D^{nano} = \theta_D^{bulk}\left(1 - 6kr_{at}/d_{eff}\right)^{1/2}$ while shape coefficient k is expressed is a function of volume V, $V = \pi d_{eff}^3/6$, and fractal dimension D of a nanoparticle: $k(V,D) = V^{2/D}/\left(3V/4\pi\right)^{2/3}$. The dependence of temperature θ_D on the fractal dimension for a nanoparticle with d_{eff}=40 nm is plotted in Fig. 2b.

In the general case, the contribution of phonons to the thermal conductivity coefficient (κ_{ph}) is directly proportional to average phonon velocity v_{ph} and phonon mean-free path l_{ph} [9]: $\kappa_{ph} = C_p v_{ph} l_{ph}/3$ where C_p is the specific heat of the material under consideration. Temperature θ_D is related to the average phonon velocity according to the following equation [30,31]: $\theta_D \sqcup \left(2h/\pi k_B\right)\left(3N_A/4\pi V_m\right)^{1/3} v_{ph}$. Here, V_m is the molar volume of the considered material. The dependence of the molar volume on the nanoparticle morphology becomes significant only when the characteristic size of a nanoparticle is 5-10 times lower than the ones regarded in this paper [32], therefore, we obtain $\theta_D^{nano}/\theta_D^{bulk} = v_{ph}^{nano}/v_{ph}^{bulk}$. According to the derivations in [33,34], $l_{ph}^{nano}/l_{ph}^{bulk} = \left(\theta_D^{nano}/\theta_D^{bulk}\right)^2$. After some simple algebraic transformations taking into account all the considerations above, we obtain Eq. (1) for the phonon contribution to the thermal conductivity of a nanoparticle, κ_{ph}^{nano}, as a function of its morphology; κ_{ph}^{bulk} represents the lattice thermal conductivity of the bulk material.

$$\kappa_{ph}^{nano} = \eta \exp\left(1 - l_0/d_{eff}\right) \times \left(1 - C\left(\pi/6\right)^{2/D-1} d_{eff}^{3\left(2/D - 5/3\right)} r_{at}\right)\kappa_{ph}^{bulk}. \tag{1}$$

Decreasing the size of nanoparticle and "complicating" its morphology lead to a more significant phonon scattering effect which, in its turn, affects the heat transfer process in nanostructures. A set of models describing the phonon scattering process in nanosystems in different conditions is given in Ref. [35]. In this paper, in order to demonstrate the essence of the phenomenon, we have applied the simple model which has been previously used by M. Goyal [36] (its experimental verification in several cases is also described in [36]). In the framework of this model, we have included pre-term $\eta \exp\left(1 - l_{ph}^{bulk}/d_{eff}\right)$ in Eq. (1) where η is the surface roughness parameter, $\eta \in (0,1]$, while ratio l_{ph}^{bulk}/d_{eff} is known as the Knudsen number. According to [36], the larger values of η correspond to a smoother nanoparticle surface leading to a higher probability of the specular scattering and to a lower probability of the diffusive one. Whereas the lower the value of η is, the rougher the surface is, which leads to an increase in the probability of the diffusive scattering resulting in a significant decrease in the lattice thermal conductivity (see Fig. 3).

Note that the correlation between surface roughness η and fractal dimension D of a nanoparticle is not unique (since their nature itself is different: the fractal dimension value is associated with the surface-to-volume ratio while the surface roughness corresponds primarily to the number of edges. For example, an *amoeba-like* particle with no edges or an ellipsoid with a high aspect ratio can have fractal dimensions significantly below 3 while their surface roughness parameters can be near to 1). Several notes on the dependence of fractal dimension on the surface roughness are given in [37] (see also their graphical representation in Fig. 2 of [37]). In our considerations, we have varied parameter η from 0.85 up to 1 in increments of 0.05. Without any losses of generality, coefficient C, which also matches dimensions, is accepted to be 4π for the sake of convenience. The phonon mean-free path for pure Bi in the bulk state as well as the value of its lattice thermal conductivity have been obtained *ab initio* in [13]. Fig. 3 is plotted for the case the heat transfer takes place in the "*binary*" crystallographic direction ((100)) while the operation temperature of the thermoelectric element is 100 K.

In is also worth mentioning that a high surface-to-volume ratio leading to significant changes in the number of surface atoms as well as in the cohesive energy is characteristic not only to nanoparticles and their ensembles but also for nano- and mesoporous media (see, for examples, our calculations in [38,39]). In such cases, we may expect the dependences of thermal properties on the pore morphology similar to the ones described above. The formation of such structures is possible, for example, during the early stages of spark plasma sintering, laser sintering of nanopowders as well as using a variety of other techniques (see [39] and Refs. therein).

.
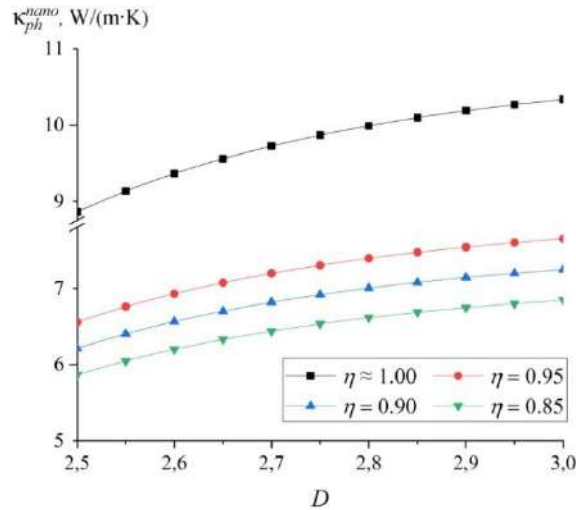
Fig. 3. The dependence of the phonon contribution to the thermal conductivity coefficient on fractal dimension D and surface roughness parameter η for a nanoparticle of pure Bi with d_{eff}=40 nm.

2. Additional remarks on nanoparticle ensembles

In the In the case of nanoparticle ensembles, the average functional properties of particles depend on the size and shape distributions in an ensemble. In [40,41], we have suggested a method for calculating such distributions based on the combined usage of number theory, fractal geometry and statistical thermodynamics. For example, the equilibrium size distributions for nanoparticles with fractal dimension D in a free-dispersed system can be expressed as follows:

$$f_D\left(\phi_p, D, N\right): \ \exp\left(-\frac{\gamma A_{sp}\left(D\right) + RT\ln f_p}{RT}\right), \ f_p = \frac{N}{N - \phi_p}\exp\left\{\pi\left(\sqrt{\frac{2}{3}}\left(N - \phi_p\right) - \sqrt{\frac{2}{3}N}\right)\right\}. \tag{2}$$

Here, $\phi_p = \omega\left(d_{eff}/d_{at}\right)^3$ is the number of atoms in a nanoparticle (its so-called "stoichiometric number"), ω is the lattice packing density, N is the total number of atoms in the system, $A_{sp}\left(D\right)$ is the specific surface area of the ensemble, γ is the surface energy of the material in the considered external environment; d_{at} is the atomic diameter. The presented estimates are in perfect accordance with the experimental data (see [40] and Refs. therein) and make it possible to model the thermodynamical conditions for the realization of optimal average geometric characteristics of nanoparticles leading to the optimal thermal and thermoelectric properties as well to predict the degree at which such properties are "blurred" in an ensemble. For example, average fractal dimension $\langle D \rangle$ and average stoichiometric number $\langle \phi_p \rangle$ of nanoparticles in the ensemble can be calculated as follows:

$$\langle D \rangle = \frac{\sum_i D_i \int f_D\left(D_i, \phi_p, N\right)d\phi_p}{\Omega(N)}, \quad \langle \phi_p \rangle = \frac{\sum_i \int \phi_p f_D\left(D_i, \phi_p, N\right)d\phi_p}{\Omega(N)}, \quad \Omega(N) = \sum_i \int f_D\left(D_i, \phi_p, N\right)d\phi_p. \tag{3}$$

Here, the limits of the integration over ϕ_p belong to range $[1, N]$ while the sample of distributions is considered where $D_i \in \left(2, 3\right)$ with an arbitrarily selected step.

Similarly, the suggested model makes it possible to determine some other properties of a nanoparticle ensemble, such as effective linear nanoparticle size $\langle l_{eff} \rangle$ (the edge length of the equal-volume cube) or effective nanoparticle diameter d_{eff} (several remarks on the calculation of such values are given in [40]):

$$\langle l_{eff} \rangle = \Omega(N)^{-1} d_{at} \sum_i \int \phi_p^{1/3} f_D\left(D_i, \phi_p\right)d\phi_p, \quad \langle d_{eff} \rangle = \Omega(N)^{-1} d_{at} \sum_i \int f_D\left(D_i, \phi_p\right)d\phi_p. \tag{4}$$

It is necessary to note that the numerical calculations of integrals such as $\int x(D_i, \phi_p) f_D(D_i, \phi_p) d\phi_p$, the upper integration limit being comparable to the Avogadro number, is quite complicated due to the fact the contribution of "huge" particles $\left(\phi_p \in \left[N_A^{0.6}, N_A\right]\right)$ is practically equal to zero. In their standard description, the calculation of such integrals using the software packages such as *Mathworks MathCAD* or *Wolfram Mathematica* can be misleading. In the case *Wolfram Mathematica* is used, the problem can be solved by modifying the integration method as follows: $\left(Method \to \left\{"DoubleExponential", "SymbolicProcessing" \to 0\right\}\right)$. *Mathworks MathCAD* allows selecting the integration technique: dividing the integration region into the intervals corresponding to the maxima of function $f_D(D_i, \phi_p, N)$ has turned out to be the most appropriate approach.

Wolfram Mathematica allows replacing sum $\sum_i \int x(D_i, \phi_p) f_D(D_i, \phi_p, N) d\phi_p$ with double integral $\iint x(D, \phi_p) f_D(D, \phi_p, N) d\phi_p dD$; in this case, the final result can be obtained through integrating sequentially, at first, over ϕ_p: $X(D,N) = \int x(D_i, \phi_p) f_D(D_i, \phi_p, N) d\phi_p$, $\phi_p \in [1, N]$; thereafter, over D: $X(N) = \int X(D,N) dD$.

Conclusion

Estimating the fractal dimension of nanoparticles using the optical or electron microscopy data can be carried in the framework of various approaches [42]. Among them, it is necessary to mention the so-called "box-counting technique" [43] which allows determining with satisfactory accuracy either the two-dimensional fractal characteristics or the three-dimensional ones using halftone microscopic images. In the two-dimensional case, the technique can be described as follows: the analyzed microscopic image is converted into a monochrome one, the illumination gradient being eliminated and the brightness being normalized if necessary. A mesh is specified over the image with a predetermined step, and then the image is transformed into a binary matrix where "1" corresponds to the mesh cells with the brightness above the specified threshold value. "0" corresponds to the others. Fractal dimension D is estimated according to the following dependence: $S \sim L^D$ (to within a dimensional factor) where S is the area of the "white" surface (equal to the number of coloured mesh cells) while L is the linear size of the image (matrix rank) [44]. It is worth mentioning that the value of fractal dimension D is sensitive to the chosen brightness threshold, P, in the most general case. For the well-founded selection of the value of P as well as for the elimination of possible ambiguations, the calibration dependence, $D(P)$, is constructed; the example of such dependence is given in [46]. In the three-dimensional case, a 3D mesh is specified where two axes correspond to the spatial coordinates while the third one stands for different levels of the image brightness. The fractal dimension is determined using the relation between the number of cells with the brightness above the specified threshold and the total number of cells. For each cell with a high brightness value, all the cells below are also taken into account.

REFERENCES

1 Rowe D.M. (ed.) *Thermoelectric handbook macro to nano*. Boca Raton, CRC Press. 2006. 1008 p.

2 Tambasov I.A., Voronin A.S., Evsevskaya N.P., et al. Thermoelectric properties of low-cost cost transparent single wall carbon nanotube thin films obtained by vacuum filtration. *Phys E*. 2019. Vol. 114. 113619. https://doi.org/10.1016/j.physe.2019.113619.

3 Hu J.-Z., Liu B., Zhou J., et al. Enhanced thermoelectric cooling performance with graded thermoelectric materials. *Jpn. j. appl. phys*. 2018. Vol. 57, pp. 71801 – 71806. www.doi.org/10.7567/JJAP.57.071801.

4 Li Z., Miao N., Zhou J., et al. High thermoelectric performance of few-quintuple Sb₂Te₃ nanofilms. *Nano energy*. 2018. Vol. 43, pp. 285 – 290. www.doi.org/10.1016/j.nanoen.2017.11.043.

5 Erofeeva I.V., Dorokhin M.V., Lesnikov V.P., et al. Thermoelectric effects in nanoscale layers of manganese silicide. *Semiconductors*. 2017. Vol. 51, No. 11, pp. 1403 – 1408. www.doi.org/10.1134/S1063782617110112.

.

6   Caballero-Calero O., Martín-González M. Thermoelectric nanowires: A brief prospective.*Scripta mater*. 2016. Vol. 111, pp. 54 – 57. www.doi.org/10.1016/j.scriptamat.2015.04.020.

7   Dorokhin M.V., Erofeeva I.V., Kuznetsov Yu.M., et al. Investigation of the initial stages of spark-plasma siltering of Si-Ge-based thermoelectric materials. *Nanosyst.: phys., chem., math*. 2018. Vol. 9, No. 5, pp. 622 – 630. www.doi.org/10.17586/2220-8054-2018-9-5-622-630.

8   Kuznetsov Yu.M., Bastrakova M., Dorokhin M.V., et al. Molecular dynamics studies on spark-plasma sintering of Si-Ge-based thermoelectric materials. *AIP adv*. 2020. Vol.10, No.6, 065219. https://doi.org/10.1063/5.0011740.

9   Bulat L.P., Drabkin I.A., Karatayev V.V., et al. Effect of boundary scattering on the thermal conductivity of a nanosctructured semiconductor material based on the $Bi_xSb_{2-x}Te_3$ solid solution. *Phys. solid state*. 2010. Vol. 52, No. 9, pp. 1836 – 1841. https://doi.org/10.1134/S1063783410090088.

10 Shishulin A.V., Fedoseev V.B., Shishulina A.V. Phonon thermal conductivity and phase equilibria of fractal Bi-Sb nanoparticles. *Tech. phys.* 2019. Vol. 64, No. 4, pp. 512 – 517. www.doi.org/10.1134/S1063784219040200.

11 Shishulin A.V., Potapov A.A., Shishulina A.V. *Fractal nanoparticles of phase-separating solid solutions: nanoscale effects on phase equilibria, thermal conductivity, thermoelectric performance*. 14th Chaotic modeling and simulation, Springer proceedings in complexity. www.doi.org/10.1007/978-3-030-96964-6_30.

12 Fedoseev V.B., Shishulin A.V. Shape effect in layering of solid solutions in small volume: bismuth-antimony alloy. *Phys. solid state*. 2018. Vol. 60, No. 7, pp. 1398 – 1404. www.doi.org/10.1134/S1063783418070120.

13 Lee S., Esfarjani K., Mendoza J., et al. Lattice thermal conductivity of Bi, Sb, and Bi-Sb alloy from first principles. *Phys. rev. B*. 2014. Vol. 89, pp. 85206 – 85215. www.doi.org/10.1103/PhysRevB.89.085206.

14 Shishulin A.V., Fedoseev V.B.Stratifying polymer solutions in microsized pores: phase transitions induced by deformation of a porous material. *Tech. phys*. 2020. Vol.65, No.3, pp. 340 – 346. www.doi.org/10.1134/S1063784220030238.

15 Shishulin A.V., Fedoseev V.B. Thermal stability and phase composition of stratifying polymer solutions in small-volume droplets. *J. eng. phys. thermophys*. 2020. Vol. 93, No. 4, pp. 802 – 809. www.doi.org/10.1007/s10891-020-02182-9.

16 Shishulin A.V., Fedoseev V.B.Features of the influence of the initial composition of organic stratifying mixtures in microsized pores on the mutual solubility of components. *Tech. phys. lett.* 2020. Vol. 46, No. 9, pp. 938 – 941. www.doi.org/10.1134/S1063785020090291.

17   Geoffrion L.-D., Guisbiers G. Chemical ordering in $Bi_{1-x}Sb_x$ nanostructures: alloy, janus or core-shell. *J. phys. chem. C*. 2020. Vol. 124, No.25, pp. 14061 – 14068. www.doi.org/10.1021/acs.jpcc.0c04356.

18 Guisbiers G. Advances in thermodynamic modeling of nanoparticles. *Adv. phys. X*. 2019. Vol. 4, No. 1, 1668299. www.doi.org/10.1080/23746149.2019.1668299

19 Hill T.L. *Thermodynamics of small systems. Parts 1 & 2*. Mineola, New York, Dover Publications. 2013. 416 p.

20 Qi W.H., Wang M.P. Size and shape-dependent melting temperature of metallic nanoparticles. *Mater. chem. phys*. 2004. Vol. 88, pp. 280 – 284. www.doi.org/10.1016/j.matchemphys.2004.04.026.

21 Rose J.H., Ferrante J., Smith J.R. Universal features of bonding in metals. *Phys. rev. B*. 1983. Vol. 28, No. 4, pp. 1835 – 1845. https://doi.org/10.1103/PhysRevB.28.1835.

22   Guinea F., Rose J.H., Smith J.R. et al. Scaling relations in the equation of state, thermal expansion and melting of metals. *Appl. phys. lett*. 1984. Vol. 44, pp. 53 – 55. https://doi.org/10.1063/1.94549.

23 Fedoseev V.B., Potapov A.A., Shishulin A.V., Fedoseeva E.N. Size and shape effect on the phase transitions in a small system with fractal interphase boundaries. *Eurasian phys. tech. j.* 2017. Vol. 14, No.1, pp. 18 – 24.

24 Shishulin A.V., Fedoseev V.B. Peculiarities of phase transformations of polymer solutions in deformable porous matrices. *Tech. phys. lett*. 2019. Vol. 45, No. 7, pp. 697 – 699. https://doi.org/10.1134/S1063785019070289.

25 Potapov A.A. On fractal dimension spectrum of new lightning discharge types in ionosphere: elves, jets and sprites. *Eurasian phys. tech. j.* 2016. Vol. 13, No. 2, pp. 5 – 11.

26 Shishulin A.V., Fedoseev V.B. On some peculiarities of stratification of liquid solutions within pores of fractal shape. *J. mol. liq*. 2019. Vol. 278, pp. 363 – 367. www.doi.org/10.1016/j.molliq.2019.01.050.

27 Shishulin A.V.*,* Fedoseev V.B., Shishulina A.V. Melting behavior of fractal-shaped nanoparticles (the example of Si-Ge system). *Tech. phys*. 2019. Vol. 64, No. 9, pp. 1343 – 1349. https://doi.org/10.1134/S1063784219090172.

28 Potapov A.A. On the issues of fractal radio electronics: Processing of multidimensional signals, radiolocation, nanotechnology, radio engineering elements and sensors. *Eurasian phys. tech. j.* 2018. Vol. 15, No. 2, pp. 5 – 15.

29 Vopson M.M., Rogers N., Hepburn I. The generalized Lindemann melting coefficient. *Solid state commun*. 2020. Vol. 218. 113977. www.doi.org/10.1016/j.ssc.2020.113977.

30 Post E.J. On the characteristic temperatures of single crystals and the dispersion of "Debye heat waves". *Can. j. phys*. 1953. Vol. 31, No. 1, pp. 112 – 119. https://doi.org/10.1139/p53-010.

31 Regal A.R., Glazov V.M. Entropy of melting of semiconductors. *Semiconductors*. 1995. Vol. 29, No. 5, pp. 405 – 417.

32 Magomedov M.N. On the statistical thermodynamics of a free-standing nanocrystal: silicon. *Cryst. rep*. 2017. Vol. 63, No. 3, 480 – 496. https://doi.org/10.1134/S1063774517030142.

33 Zimann J.M. *Electrons and phonons*. Oxford, Clarendon Press. 1960. pp. 58, 288, 396, 456.

34 Soyez G., Eastman J.A., Thompson L.J. et al. Grain-size-dependent thermal conductivity of nanocrystalline yttria-stabilized zirconia films grown by metal-organic chemical vapor deposition. *Appl. phys. lett*. 2000. Vol. 77, No. 8, pp. 1155 – 1157. https://doi.org/10.1063/1.1289803.

35 Khvesyuk V.I. Skryabin A.S. Heat conduction in nanostructures. *High temp*. 2017. Vol. 55, No. 3, pp. 434 – 456. https://doi.org/10.1134/S0018151X17030129.

36 Goyal M. Shape, size and phonon scattering effect on the thermal conductivity of nanostructures. *Pramana: j. phys.* 2018. Vol. 91, pp.87. www.doi.org/10.1007/s12043-018-1660-8.

37 Fedoseev V.B. The use of fractal geometry for the thermodynamic description of the free-dimensional crystal structure elements. *Lett. mater*. 2012. Vol. 2, pp. 78 – 83.

38 Shishulin A.V., Fedoseev V.B., Shishulina A.V. Variation of the Curie temperature in porous materials. *Tech. phys. lett*. 2020. Vol. 46, No. 7, pp. 680 – 682. https://doi.org/10.1134/S106378502007024X.

39 Shishulin A.V., Potapov A.A., Shishulina A.V. On the transition between ferromagnetic and paramagnetic states in mesoporous materials with fractal morphology. *Eurasian phys. tech. j.* 2021. Vol. 18, No.2, pp. 6 – 11. https://doi.org/10.31489/2021NO2/6-11.

40 Fedoseev V.B., Shishulin A.V. On the size distribution of dispersed fractal particles. *Tech. phys*. 2021. Vol. 66, No. 1, pp. 34 – 40. www.doi.org/10.1134/S1063784221010072.

41 Shishulin A.V., Potapov A.A., Shishulina A.V. The initial composition as an additional parameter determining the melting behavior of nanoparticles (a case study on Si_x-Ge_{1-x} alloys). *Eurasian phys. tech. j.* 2021. Vol. 18, No.4, pp. 5 – 13. https://doi.org/10.31489/2021NO4/5-14.

42 Potapov A.A., Pakhomov A.A., Potapov A.A. (Jr.), Potapov V.A. Processing by robust fractal-topological methods of flows of optical texture images on the Martian surface. *Eurasian phys. tech. j.* 2019. Vol. 16, No.2, pp. 5 – 10. https://doi.org/10.31489/2019NO2/5-10.

43 Li J., Du Q., Sun C. An improved box-counting method for image fractal dimension estimation *Pattern recognit*. 2009. Vol. 42, pp. 2460 – 2469. www.doi.org/10.1016/j.patcog.2009.03.001.

44 Fedoseeva E.N., Fedoseev V.B. Interaction of chitosan with benzoic acid in solution and films. *Polymer sci. Ser. A*. 2011. Vol. 53, No. 11, pp. 1040 – 1046. https://doi.org/10.1134/S0965545X1110004X.

.

THE INFLUENCE OF SIZE EFFECTS ON THE ORDERING OF LIQUID CRYSTALS LOCATED ON NANORIBBON GRAPHENE

Agelmenev M.E. [1*], Bratukhin S.M.[1], Polikarpov V.V.[2]

[1] E.A.Buketov Karaganda University, Karaganda, Kazakhstan, amaxut58@gmail.com
[2] Ltd "NTL KAZAKHSTAN", Karaganda, Kazakhstan

Experiments on computer simulation of the behavior of polar nematic phenylpropargyl ethers of parachlorophyllens on the surface of graphene nanoribbon made it possible to reveal a number of regularities. The dynamics of molecules is studied when the dimensions of graphene change under the action of an electric field and temperature. As a research method, the method of molecular dynamics was used in the approximation of a liquid state of aggregation. The simulation was carried out in the atomistic approach. It was shown that the graphene nanoribbon and electric filed defines the self-assembly of the nematic liquid crystals molecules in the biaxial state. These states appear at the variation of the graphene nanoribbon ratio of width to length. It was found that in the clearing area the ordering of the parachlorophyllens starts to grow when the value of the ratio of width to length is 3: 1.

Keywords: nematic liquid crystals, graphene nanoribbon, computer modeling

Introduction

Graphene has a great interest due to its electrical and thermoelectric properties. Research on changes in the electronic states of metal ions [1-2], photo-electro-chemical response [3], absorption processes [4], the nature of the interaction [5], electrical [6-7] and temperature conductivity [8], phase transition temperatures [9] show the crucial role of graphene. The performed experiments [10] on computer modeling of the behavior of the polar parachlorophyllens (PEC), located on the surface of graphene nanoribbon (GNR), allowed identifying a number of laws. The little effect of the graphene type on the behavior of the NLC was shown. It was established that the ordering of nematic liquid crystals increase non-linear with increasing of the electric field. The determining role of nanoribbon graphene and the electric field on self-organization of the NLC in the enlightenment region was shown. This allows stating that at least two processes are taking place under the influence of temperature and electric field: the first - "flow" of the molecules in the direction of X, the second - the rotation of the molecule in the direction of this axis. The second process may be due to the reorientation relative to the electric field of the molecules.

It is clear that for an effective use of nanoribbon graphene in devices there is need of understanding of the processes occurring in composite materials with nanoribbon graphene at the   temperature and other influences. The physical and chemical properties of the components definitely have significant effect on it. The widely used in electronics the liquid crystals are one of these materials by Wahle et al. [11]. As noted Divari et al. in [12], the ratio between length and width of the graphene has large impact on these properties. The founded effect of the flow of nematic liquid crystals (NLC) by we in [13] on the graphene surface at the temperature change had been experimentally confirmed [14]. Therefore, the understanding of influence of nanoribbon graphene size on the properties located on the surface of such electronic products as the NLC must be considered when creating optoelectronic devices based on these compounds.

In this regard, the purpose of this work was to study the effect of nanoribbon graphene size on the dynamics of behavior molecules of nematic arylpropargyl esters of phenols with temperature and electric field changes.

1. The methodology of the analysis

As a sample the nematic liquid crystal - phenylpropargyl ether of PEC [15], located on the nanoribbon graphene in a planar orientation was used. For the modeling of the behavior of these compounds we used the method of molecular dynamics based on the program GROMACS [16] version 3.3.1 approaching liquid state [17-19]. In the modeling the NPT ensemble is used, the modeling time at a given temperature was 10 ps. The Coulomb and van der Waals interactions were used in the modeling of the dynamic dynamics method. The corresponding parameters for these options are specified in [16]. The radius of the cutoff of the Coulomb interaction and the dispersion was 2 nm. The successive annealing was carried out in the heating mode. The input file for cluster formation was created, which took into account the distance between the molecules, in rows and layers of the cluster in the direction of XYZ. The grapheme sizes were varied by direction (OX), perpendicular to the director (OY). At the same time the sizes of the cluster and other side of graphene (OY) were unchanged. The direction of the electric field was set on the direction of the director.

The studies were carried out in the presence of the electric field parallel to the director. The graphene sizes that were used in the modeling varied, with a ration of width (X) to the length (Y) - 1:1 (115Å: 115Å, 2:1 (230Å: 116Å), 3:1 (345Å: 116Å), 3,5 1 (401Å: 116Å). In the study of the influence of some parameters the number of molecules of PEC was unchanged and they were oriented planar respectively to the graphene's plane. The structure of the graphene was chosen in the form of zigzag (Z) and armchair (A) [18]. The method of preparing and analysis of modeling results is presented in [15, 19].

2. Results and discussion. Effect of the GNR`s size on the dynamic behavior of the NLC

In this study the GNR`s size that was used in the modeling varied by the ratio of width to length - 1:1 (1), 2-1 (2), 3-1 (3), 3.5:1 (4), but the number of the PEC molecules were kept same. The electrical intensity value was 1×10^7 V / m, and it was directed by Y (Director). The research results are presented in Fig.1-7. The numbers are consistent with given ratios of width to length of the GNR and used in the figures.
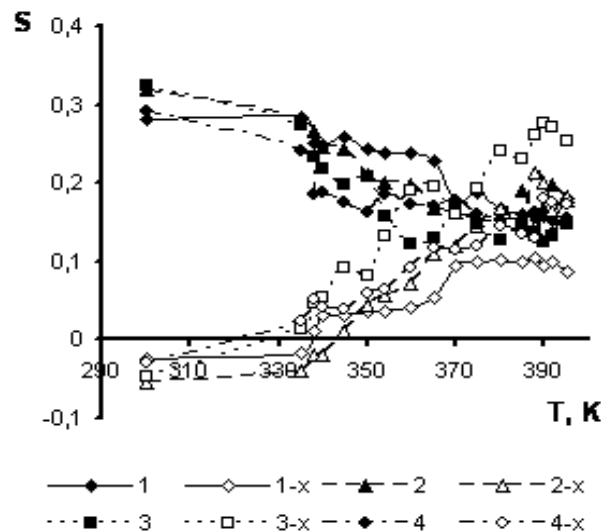
Fig.1. Temperature dependences of the ordering degree of the PEC at different GNR`s sizes (1, 2, 3, 4) and coordinates (x, y)

As seen in Fig. 1, the difference in the ordering degree values in two coordinate axes is observed before the temperature of decay of the dimers as in the previous section. The ordering degree values relative to the axes X and Y are changing in opposite direction with increase of temperature: along X increases, along Y reduces. In case 1 this value is higher in the clearing area than the value relative to the X-axis. In cases 2 and 4 the ordering degree values with respect to X and Y are equal. In case 3, there is a matching value at the decomposition temperature of dimers (354 K). The ordering degree along X exceeds this value with respect to Y with further increase in temperature; only at the temperature of 370 K they become equal. Biaxial state develops in varying ordering degrees in the OX and OY axis at melting temperature.

As seen in Figure 2, for case 3 the highest increase in the ordering at the clearing area is typical, less in case 2. This is the exact ratio, which significantly changes the electrical properties of the GNR [12]. The curves of the temperature dependences of the bond energy for all cases (Fig. 3) show the increase of its value with the increase of a temperature. The most rapid growth occurs in case 3. The smaller increase is observed in cases 2 and 4. This is consistent with the considered temperature dependences of the ordering degree and information entropy.
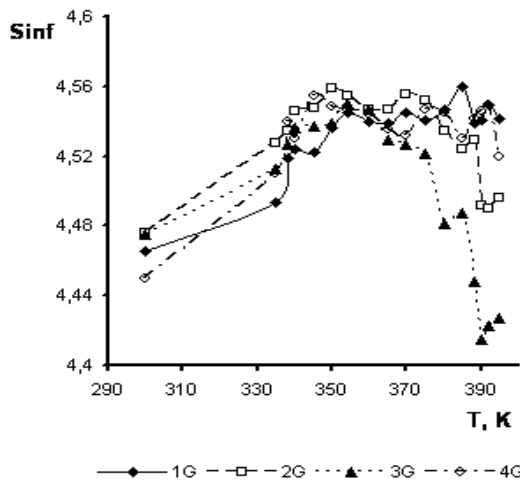
Fig.2. Temperature dependences of the information entropy for different GNR`s sizes (1, 2, 3, 4).
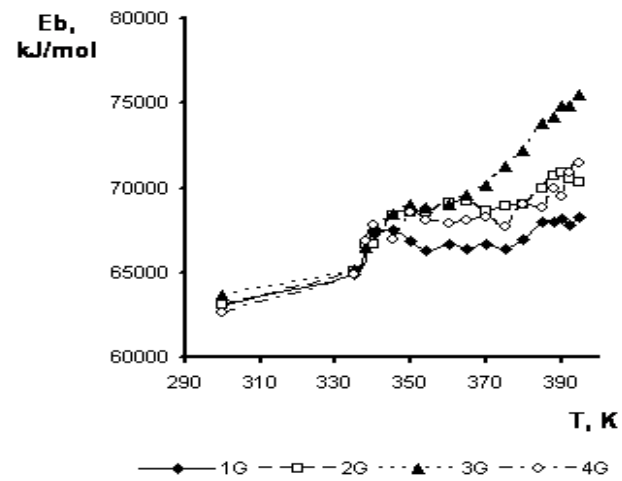
Fig.3 Temperature dependences of the bond energy for different GNR`s sizes (1, 2, 3, 4)

As shown on snapshots of clusters in various phase states (Fig. 4-7), the thickness of clearing becomes smaller with increasing ratio of width to length of the GNR. This is obviously due to the flow of the PEC molecules with increasing of temperature and surface of the GNR area.

300 K   338 K   354 K   390K
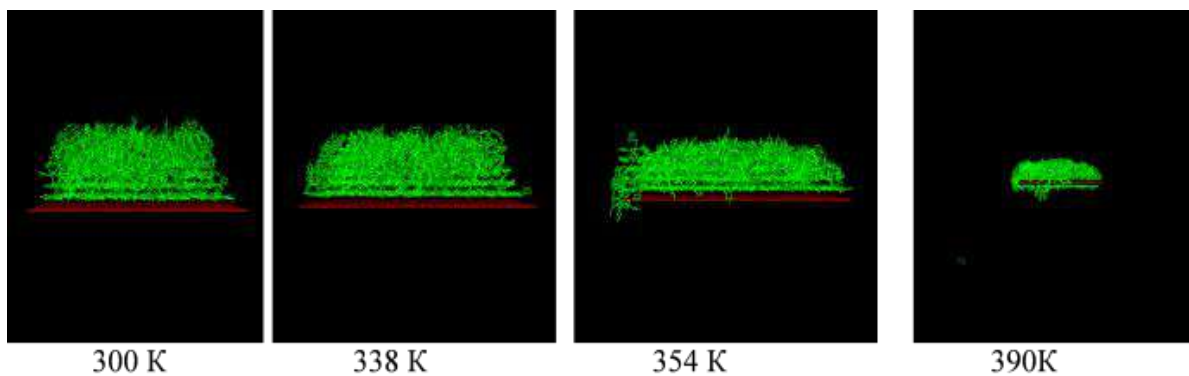
Fig.4. Snapshots of clusters in XOZ plane at the ratio of width to length (1)

300 K   338 K   354 K   390K
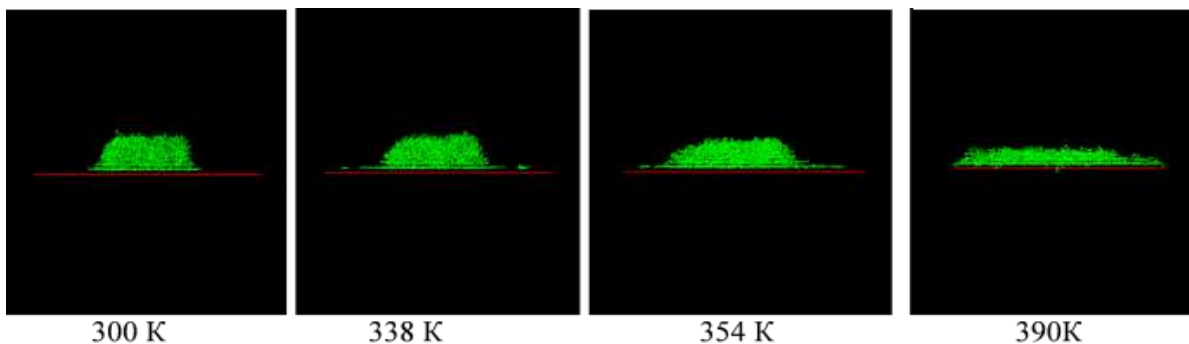
Fig.5. Snapshots of clusters in XOZ plane at the ratio of width to length (2)
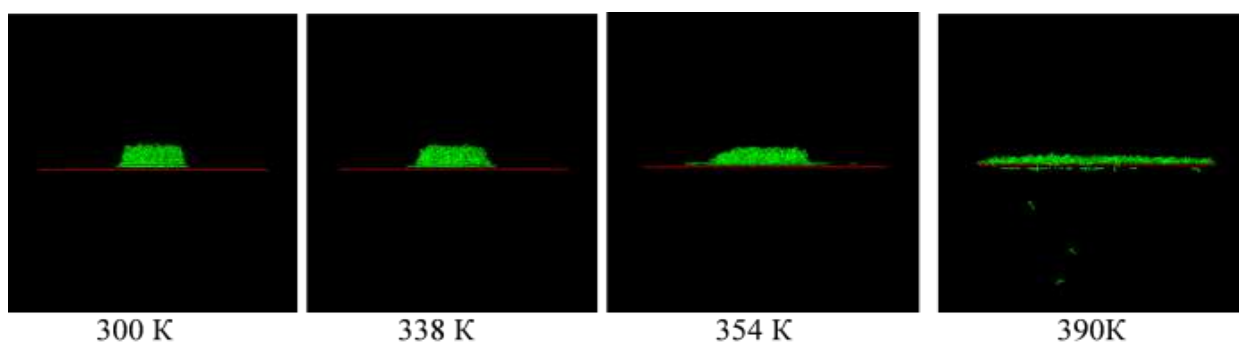
Fig.6. Snapshots of clusters in XOZ plane at the ratio of width to length (3)
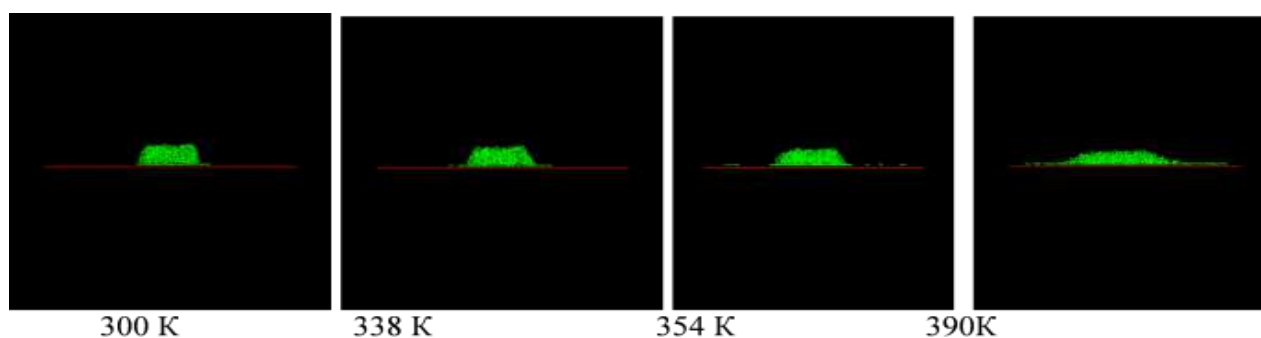
Fig.7. Snapshots of clusters in XOZ plane at the ratio of width to length (4)

Taking into account that the main flow X direction is perpendicular to the initial of molecules Y location the existence of 2 processes in clusters can be assumed. These processes occur simultaneously with increasing of temperature, which are most agreed from the moment of the dimer disintegration (354 K).

The first process is "flow" of the molecules in the direction of X, the second - the rotation of the molecule in the direction of this axis. The second process may be due to the reorientation relative to the electric field of the molecules, since the PEC dipole moment [15] has an angle of 50^0 relative to the longitudinal axis of the molecule in its initial state. The ratio of width to length as 3:1 should lead to the maximum universal conductivity of the GNR near the Dirac [13] point and at the ratio of 1:3 leads to the minimum value. However, the molecular dynamics method does not account quantum properties of the GNR. However, the carried out studies allow us to state that the nematic liquid crystals dynamics depends on the size of the GNR. The ratio of width to length of 3:1 leads to noticeable changes in the ordering in the clearing area.

Thus, on the basis of these studies it was found that the value of the ratio of width to length of 3 / 1 the ordering of the NLC begins to rise in the clearing area. This may be due to the possibility of a larger movement of molecules on the front surface, also due to the distribution of electron density of the GNR atoms.

Conclusion

It's identified a some of dependences by the performed computer modeling experiments on the polar PEC behavior located on the GNR surface. It was shown that the GNR and electric filed [10] defines the self-assembly of the NLC molecules in the biaxial state. These states appear at the variation of the GNR ratio of width to length. It was found that in the clearing area the ordering of the NLC starts to grow when the value of the ratio of width to length is 3: 1.

This helps to state that at least two processes are taking place under the influence of temperature and electric field: first one is the "flow" of the molecules in the direction of X, and the second one is the molecule rotation in the direction of this axis. The second process may be due to the molecule reorientation relative to the electric field. An isotropic phase and nematic phase coexist when NLC is on the prepared exfoliated graphene oxide platelets [20]. This is consistent with our results. Formation of this composite requires controlling of the GNS size.

REFERENCES

1   Kawabata H., Iyama T., Tachikawa H. Interaction of Lithium Ion (Li$^+$) with Chlorinated Graphene (Cl-Graphene) Surface: A Direct Ab-Initio MD Study. *Mol. Crys.Liq.Cryst*. 2009. Vol. 504, No.1, pp. 147-154.

2   Abe S., Watari F., Takada T., Tachikawa H. "A DFT and MD Study on the Interaction of Carbon Nano-Materials with Metal Ions", *Mol. Crys.Liq.Cryst*. 2009. Vol. 505, No.1, pp. 51-58.

3   Jung S.W., Park J-H., Seo S-W., et al. Enhanced Photoelectrochemical Response of Graphene-Coated Al2O3-TiO2 Nanocomposite Photoanodesung, *Mol. Crys.Liq.Cryst*. 2011. Vol.538, No.1, pp. 272-277.

4   Liu W., Zhao Y.H., Nguyen, J., et al. Electric field induced reversible switch in hydrogen storage based on single-layer and bilayer graphenes. *Carbon*. 2009. Vol. 47, No.15, pp. 3452 – 3460.

5   Fugetsu B., Sano E., Yu H., Mori K., Tanaka, T. Graphene oxide as dyestuffs for the creation of electrically conductive fabrics. *Carbon*. 2010. Vol.48, No.15, pp. 3340 – 3345.

6   Fan Y., Wang L., Li J., Li J., Sun S., Chen F., et al. Preparation and electrical properties of graphene nanosheet/Al2O3 composites. *Carbon*. 2010. Vol. 48, No.6, pp. 1743 – 1749.

7   Ramana G.V., Padya B., Srikanth V.V., et al. Electrically conductive carbon nanopipe-graphite nanosheet/polyaniline composites. *Carbon*. 2011. Vol. 49, No.15, pp. 5239 – 5245.

8   Wei Z., Ni Z., Bi K., Chen M., Chen Y. In-plane lattice thermal conductivities of multilayer graphene films", *Carbon*. 2011. Vol. 49, No 8, pp. 2653 – 2658.

9   Vadukumpully S., Paul J., Mahanta N., Valiyaveettil S. Flexible conductive graphene/poly (vinyl chloride) composite thin films with high mechanical strength and thermal stability. *Carbon*. 2011. Vol.49, No.1, pp.198-205.

10   Agelmenev M.E., Bratukhin S.M., Polikarpov V.V. The influence of various effects on the ordering of liquid crystals located on nanoribbon graphene. *Eurasian Physical Technical Journal*. 2018. Vol.15, No.1(29), pp. 40 – 47.

11   Wahle M., Kasdorf O., Kitzerow H-S., Liang Y., Feng X., Müllen K. Electrooptic Switching in Graphene-Based Liquid Crystal Cells. *Mol. Cryst. Liq. Cryst*. 2011. Vol. 543, No.1, pp. 187 – 193.

12   Divari P.C., Kliros G.S. Modeling the thermopower of ballistic graphene ribbons. *Physica E*. 2010. Vol. 42, No.9, pp. 2431–2435.

13   Agelmenev M.E., Muldakhmetov Z.M., Bratukhin S.M., Polikarpov V.V. The Influence of the Nano Substrate on the Nematic Liquid Crystals Behaviour. *Mol. Crys.Liq.Cryst*. 2011. Vol. 545, No.1, pp. 36 – 43.

14   Yu J-S., Kim S.J., Kim J-H. Effect of graphene layers on the alignment of nematic liquid crystal. *Book Abstract of the "23rd Intern. Liq. Cryst. Confer."* Krakow, Poland, 2010, pp.223.

15   Agelmenev M.E., Bazhikov K.T., Muldakhmetov Z.M., Sizykh M.Yu. Effect of the Nature of Halogen on the Acetylene Compounds. *Rus.J.Phys.Chem*. 2022. Vol.76, No.10, pp.1713 – 1714.

16   Van der Spoel D., Lindahl E., Hess B., van Buuren A.R., Apol E., Meulenhoff P.J., et al. *GROMACS User Manual version 3.3.1*. Available at: www.GROMACS.org

17   Agelmenev M.E., Muldakhmetov Z.M., Bratukhin S.M., Pak V.G., Polikarpov V.V., Yakovleva O.A. The dynamics of some nematic liquid crystals. *Mol.Crys.Liq.Cryst*. 2008. Vol. 494, pp. 339 – 352.

18   Agelmenev M.E., Bratukhin S.M., Muldakhmetov Z.M., Polikarpov V.V. Mesogenic System Simulation in the Liquid State of Aggregation. *Rus.J.Phys.Chem*. A. 2010. Vol. 84, No.7, pp.1158 – 1162.

19   Agelmenev M.E. The modeling with free boundary. *Mol.Crys.Liq.Cryst*. 2011. Vol. 545, No.1, pp.190-203.

20   Choi W., Lahiri I., Seelaboyina R., Kang Y.S. Synthesis of Graphene and Its Applications: A Review. *Critic. Rev. in Solid State and Materials Sciences*. 2010. Vol. 35, pp. 52 – 71.

ELECTRON KINETICS OF YTTRIUM IRON GARNET
AFTER SWIFT HEAVY ION IMPACT

Rymzhanov R.A.[1,2,*], Volkov A.E.[2,3], Ibrayeva A.D.[1,4]

[1]The Institute of Nuclear Physics, Almaty, Kazakhstan; r.a.rymzhanov@gmail.com
[2]Joint Institute for Nuclear Research, Dubna, Moscow Region, Russia;
[3]Lebedev Physical Institute of the Russian Academy of Sciences, Moscow, Russia;
[4]Centre for HRTEM, Nelson Mandela University, Port Elizabeth, South Africa;

The TREKIS Monte-Carlo model was applied to study the temporal electronic kinetics of yttrium iron garnet after a swift heavy ion impact. Cross sections of incident particles interaction with the target were determined within complex dielectric function-dynamic structure factor formalism. We found two modes of the spatial propagation of electronic excitation: fast delta-electrons form a front of the excitation while electrons produced due to decay of plasmons generated in a track form the second front slowly following behind the first one. Analysis of mechanisms of target lattice heating pointed to an important contribution of the potential energy released due to recombination of valence holes generated in an ion track. An increase of the excess lattice energy due to elastic scatterings of electrons and holes described with Mott cross-sections is minor. In contrast, complex dielectric function formalism demonstrates the significant contribution of these processes to the heating of the lattice.

Keywords: swift heavy ion track, electron excitations, complex dielectric function, ion energy loss, Monte Carlo simulations.

Introduction

Irradiation with swift heavy ions (SHI) decelerated due to the ionization processes can be applied as an effective tool for modification of solids, considerably changing material properties on the nanometric scale. The largest part of an energy deposited by an SHI is spent on excitation of the electron subsystem of a material [1,2]. Parameters of the initially excited electron ensemble determines subsequent kinetics of the electronic and atomic subsystems in the nanometric vicinity around the SHI trajectory [3]. The modification of the physical, chemical and mechanical properties of a target by SHI irradiation on nanometric level allows to use it in various nanostructuring applications [4–7].

Knowledge of cross-sections of charged particle scatterings on coupled target electrons as well as lattice atoms allows tracing the kinetics of material excitation along the ion trajectory that forms a basis for description of nonequilibrium structure modifications in SHI tracks. In this paper the complex dielectric function (CDF) formalism [8–10] is implemented to determine these cross sections for yttrium iron garnet ($Y_3Fe_5O_{12}$, YIG). The formalism takes automatically into account collective modes of electronic excitations in the target. Calculated cross sections of an SHI, electrons and valence holes scattering are then incorporated into the Monte-Carlo (MC) model describing coupled electronic and lattice kinetics in SHI tracks. Further, we analyze and compare contributions of different processes of electron-to-atoms energy transfer to lattice heating of YIG and Al_2O_3 in ion tracks.

1. Model

Based on asymptotic trajectories algorithm, the event-by-event simulations [11,12] of charged particles propagation forms the main principle of the MC code TREKIS [13,14]. We use the dynamic structure factor (DSF) formalism for determination of probabilities of charged particles interaction with a solid [8]. The dynamic structure factor can be declared as a product of the energy loss function (ELF), or the inverse imaginary part of the complex dielectric function (CDF) of a material. We reconstruct the ELF from the experimental and theoretical optical data as a set of artificial Drude oscillators [9,15], which gives us an

ability to describe partial cross-sections of electron interaction with the valence band and core shells as well as with the target lattice.

The TREKIS models: (a) propagation of an SHI producing ionization of a target and generation of free electrons (δ-electrons), holes in the valence band (VB) and deep atomic shells; (b) free δ-electrons interactions with ionic and electronic subsystems as well as subsequent kinetics of secondary electronic cascades forming due to relaxation of the excitation; (c) Auger decays of core holes, also forming secondary electrons; (d) radiative decays of deep shell holes, subsequent photon transport and photoabsorption, which produces new holes and electrons; (e) valence holes transport and their energy transfer to the lattice [13,14]. All details of the model assumptions and numerics of the code were thoroughly described in [13,14].

We analyze two channels of lattice excitation in the present approach: (1) due to elastic scattering of electrons and valence holes on the atomic system and (2) heating after release of the potential energy of the excited electron ensemble into the lattice due to recombination of valence holes. To describe this release, we assume an instant transfer of the excess potential energy of valence holes to the target atoms at 100 fs after the ion impact. Our previous works, Ref. [16,17], illustrated reliability of the applied approximation.

The MC procedure is iterated for ~103 times to obtain a trustworthy statistic for spatial and temporal distributions of parameters characterizing the excitation of a target: densities and energy densities of electrons, atoms, valence band holes and core holes in the proximity of an SHI track. These distributions can serve as input parameters (initial conditions and/or source terms) in further MD modeling of the kinetics of a lattice relaxation, structural modifications and phase transitions caused by an SHI passage [18,19].

2. Results and discussion

2.1. Construction of energy loss function

The energy loss function of YIG was reconstructed using ab-initio calculated optical properties from [20] and x-ray attenuation length from [21]. Figure 1a presents the loss function curve consisting of the set of peaks arising from peculiarities of photon interaction with the valence band and deep shells. We found in the literature data only for limited energy range for optical coefficients originated from the VB, so the intermediate energy region in Fig.1 was approximated to fulfill the sum rules. The scattering of excited electrons on atomic ensemble is described using Mott atomic cross sections with modified Molier's screening parameter [22,23] since no optical data describing phonon modes of YIG exist in the literature.
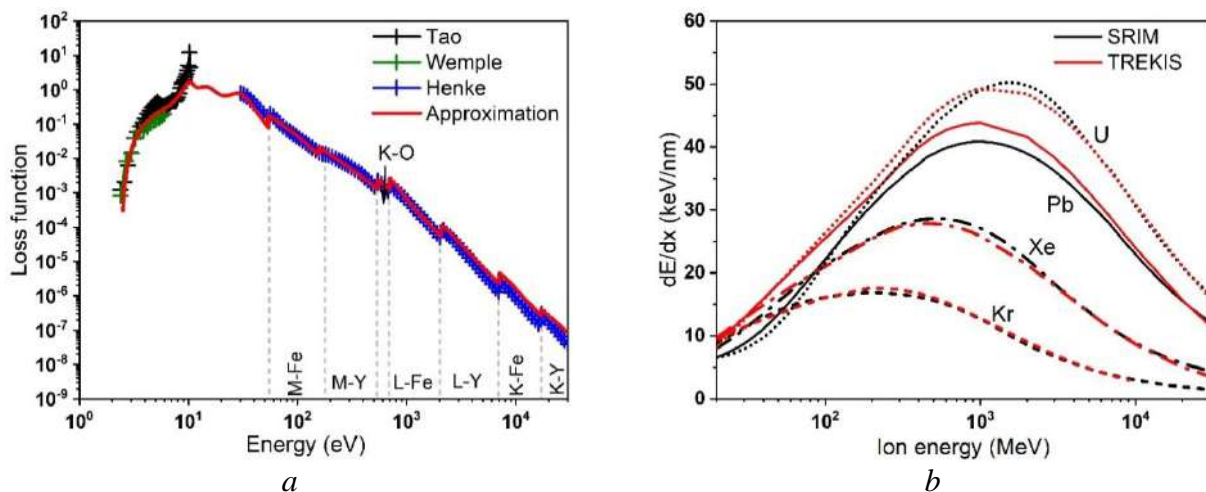
Fig.1. (a) Energy loss function of YIG obtained using experimental and theoretical optical data from: Tao [20], Henke [21] and Wemple [27]. (b) Energy dependent energy losses of different ions in YIG compared with SRIM code [25].

Table 1 collects the coefficients of the energy loss function of yttrium iron garnet in form of optical oscillators [9,13,26]. In this Table f-sum rule corresponds to the number of electrons (N_e) on a specific atomic shell and coincides very well with values from [27] (in brackets). The accuracy of the obtained ELF coefficients was verified by comparison of the calculated energy losses of different ions in YIG (Fig. 1b) with the SRIM code [25]. An overall good agreement confirms an applicability of the obtained fitting coefficients for the determination of cross sections of charged particles interaction with a solid YIG.

Table 1. Coefficients of the complex dielectric function of YIG in the form of oscillator functions. E_0, A, γ are coefficients of Drude-like oscillators [9, 13,26] used for ELF approximation. *f*-sum is the number of electrons (N_e) on the atomic shells. The values from [27] are shown in brackets for comparison.

Shell	E_0	A	γ	*f*-sum (N_e)
Valence band	3.1	-0.74	2.7	90.999 (91)
	10.2	30	2.5	
	15	114	8	
	30	380	18	
M-Fe	54	504	90	70.06 (70)
M-Y	157	532	400	78.01 (78)
K-O	540	202	340	23.997 (24)
L-Fe	700	338	350	39.999 (40)
L-Y	2100	192	1600	24.06 (24)
K-Fe	7000	83	5000	9.98 (10)
K-Y	17000	46	20000	5.98 (6)
Total:				343.09 (343)

2.2. Kinetics of the electron ensemble

Figure 2a presents temporal evolution of the radial energy density distributions of electrons in YIG calculated with MC TREKIS. We used Bi ions with 700 MeV energy, providing the energy losses of 43.6 keV/nm in YIG. Figure 2a demonstrates propagations of two fronts outwards from the ion trajectory. Movement of fast primary δ-electrons produced directly by the ion forms the first front.
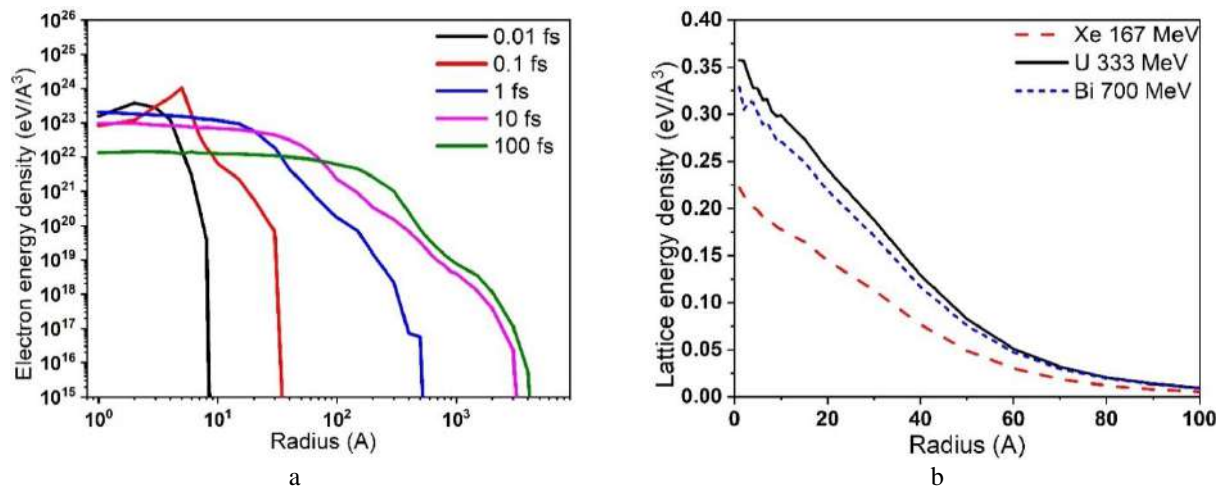
Fig.2. (a) The radial electron energy distributions around the trajectory of 700 MeV Bi ion in YIG at different times; (b) radial lattice energy distribution in tracks of different ions at 100 fs.

The second one results from generation of a large number of secondary electrons with the energies around the plasmon peak in the valence band. We assume that these electrons with approximately the same energy are generated due to fast decay of plasmons appeared in the ion track. Subsequent collective propagation of these electrons outwards from the center of excited area forms the front in the spatial energy density at earlier times (< 1 fs) which then smoothens out by the time of 10 to 100 fs.

Electrons spreading out of the track core interact inelastically with target atoms (producing new electrons and holes) and elastically (transferring a part of their energy to the atomic subsystem). Figure 2b shows the distribution of excess lattice energy, which consists of three main contributions: elastic scattering

of electrons, energy transfer by spreading valence holes and the potential energy release due to recombination of valence holes. As was discussed in [28] this potential energy may be quickly (at 100 fs timescale) converted into the kinetic energy of atoms due to changes of the interatomic potential stimulated by the highly excited electron system. We approximate this energy increase by the band gap energy (per one valence hole remaining in a track by the time of 100 fs after ion passage). This energy is assumed to be instantly transferred to atoms at 100 fs [16].

Figure 3 compares dependencies of the energy transferred into YIG and Al_2O_3 lattices on the kinetic energy of scattered electrons and valence holes in a track of 167 MeV Xe ion. For comparison, we show the results of applications of two forms of elastic cross-sections in alumina: the Mott atomic approximation and scattering on optical phonons using CDF-DSF formalism.
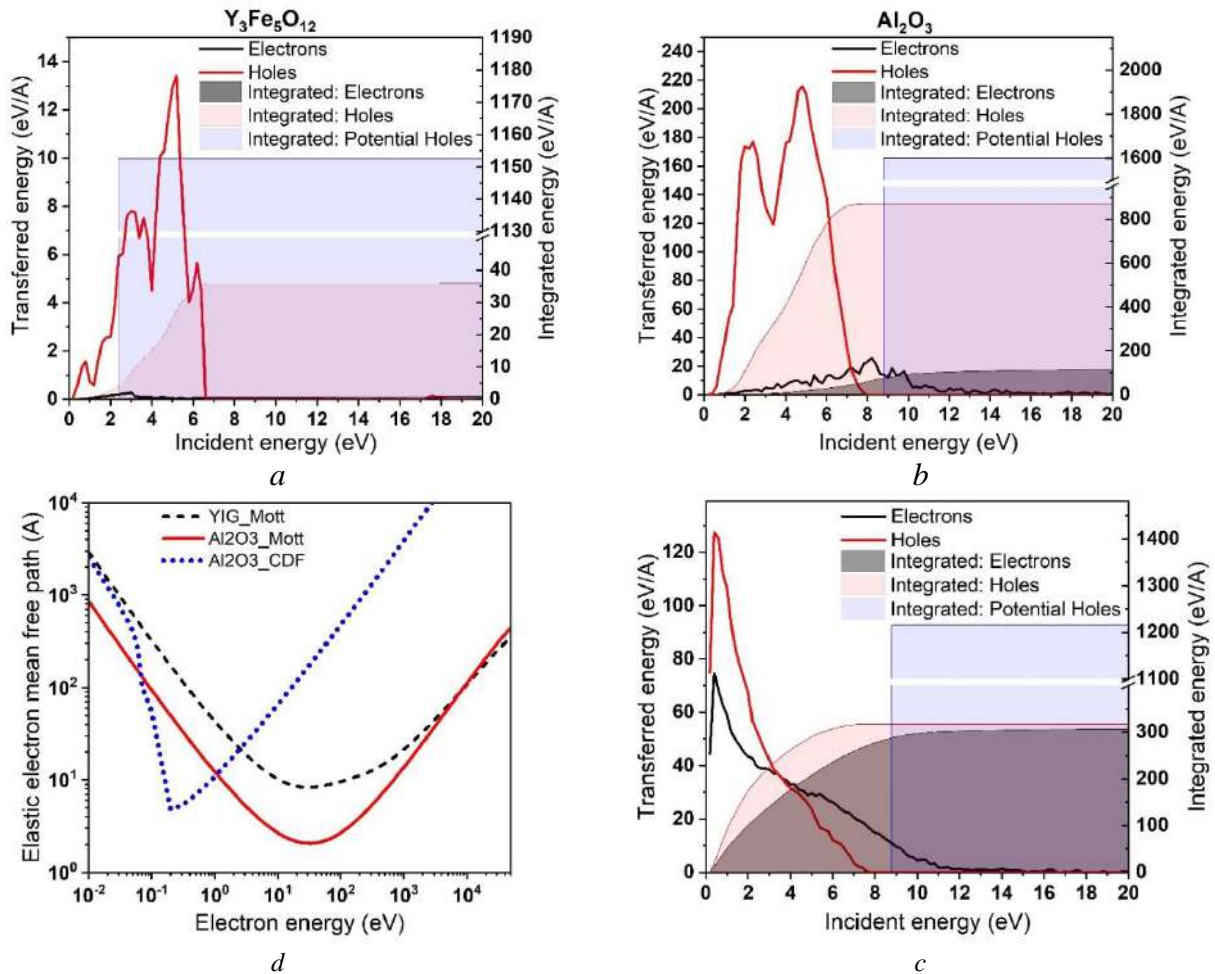
Fig.3. Dependence of the total energy transferred to the lattice by electrons and valence holes in 167 MeV Xe track on the particle kinetic energy in (a) YIG and (b) Al_2O_3 calculated using Mott atomic cross-sections, (c) Al_2O_3 calculated within CDF phonon cross-sections. Filled area shows the integrated elastic energy transfer by electrons/holes (grey and red) and potential energy of valence holes (blue). (d) Electron elastic mean free paths in YIG and Al_2O_3.

The potential energy distribution of valence holes is not shown in this Figure but it can be represented as a delta-function located at the band gap energy (2.4 eV for YIG and 8.8 eV for Al_2O_3). Blue filled rectangles represent the total excess energy accumulated by the lattice due to release of the potential energy of valence holes, which may constitute up to 65% of total lattice energy in alumina and about 97% in YIG.

Figure 3a also demonstrates that the almost all rest lattice energy (~3 %) for YIG is delivered by elastic interaction of valence band holes with target atoms, whereas electron scattering contributes less than 0.1 % of the total energy, when the Mott cross-section describes the both scattering processes. Almost all lattice energy is transferred by holes with energies below 6 eV.

In contrast to YIG, contributions of elastic scatterings of electrons and holes into heating of Al_2O_3 lattice is much larger: 4% for electrons and 32% for valence holes when the Mott cross section are used

(Figure 3b). Application of the phonon cross-sections gives the almost equal fractions of elastic channels of the energy transfer to the alumina lattice: ~17% for electrons and the same for valence holes (Figure 3c).

The registered difference between YIG and Al_2O_3 can be attributed to difference of atomic mass: the lower atomic masses in Al_2O_3 result in the higher probability of electron scattering (Figure 3d) on the lattice and the larger energy transfer to an atom in one impact.

It can be found, that the largest part of the energy transferred to lattice is provided by electrons and holes of energies below 10 eV. The maximum of the described by Mott cross-sections energy transferred by electrons is located at energies of ~8 eV (Figure 3b) whereas CDF cross sections result in maximum located at the much lower energies (< 0.5 eV). This difference reflects the positions of minima of the electron mean free path (inverse cross section) to elastic scattering on lattice (Figure 3d).

Conclusions

We present the results of simulations of electron subsystem excitation in swift heavy ion tracks in YIG performed with the help of the TREKIS MC code. The complex dielectric function formalism was applied to develop scattering cross sections and the energy losses of charged particles in YIG. Applicability of this approach was confirmed by a good agreement of calculated data with results of application of SRIM code [24].

Time resolved calculations revealed propagation of two fronts of electronic excitation. Fast δ-electrons form the first front while the second one behind it is attributed to electrons appearing due to decays (within 10 to 100 fs) of plasmons produced by excitation of electron ensemble.

Contributions of elastic scattering of electrons and valence holes to heating of the atomic subsystem were investigated. We show that the majority (~97%) of the lattice energy for YIG is delivered by conversion of the potential energy of valence holes, whereas contribution of elastic scatterings of electrons and holes is minor. In contrast to YIG, Al_2O_3 demonstrates the comparable contributions of these processes to the heating of the lattice. Electrons and holes of energies below 10 eV provide largest part of lattice energy transferred to the lattice via the elastic scattering channel in both materials.

Acknowledgments

REFERENCES

1 Komarov F.F. Defect and track formation in solids irradiated by superhigh-energy ions. *Physics-Uspekhi.* 2003. Vol. 46, pp. 1253–1282.

2 Miterev A.M. Theoretical aspects of the formation and evolution of charged particle tracks. *Physics-Uspekhi.* 2002. Vol. 45, pp. 1019–1050.

3 Baranov A.A., Medvedev N.A., Volkov A.E., et al. Effect of interaction of atomic electrons on ionization of an insulator in swift heavy ion tracks. *Nuclear Instruments and Methods in Physics Research B.* 2012. Vol. 286, pp. 51–55.

4 Komarov F.F. Nano- and microstructuring of solids by swift heavy ions. *Physics-Uspekhi.* 2017. Vol. 60, pp. 435–471.

5 Wesch W., Wendler E. *Ion Beam Modification of Solids, Ion-Solid Interaction and Radiation Damage.* Berlin: Springer, Cham, 2016, 534 p.

6 Jana K.K., Ray B., Avasthi D.K., Maiti P. Conducting nano-channels in an induced piezoelectric polymeric matrix using swift heavy ions and subsequent functionalization. *Journal of Materials Chemistry.* 2012. Vol. 22, pp. 3955.

7 Kozlovskiy A.L. Study of the wear resistance degradation kinetics of aln ceramic under heavy ion irradiation. *Eurasian Physical Technical Journal.* 2022. Vol. 19, pp. 10–14.

8 Van Hove L. Correlations in Space and Time and Born Approximation Scattering in Systems of Interacting Particles. *Physical Review.* 1954. Vol. 95, pp. 249–262.

9 Ritchie R.H., Howie A. Electron excitation and the optical potential in electron microscopy. *Philosophical*

Magazine. 1977. Vol. 36, pp. 463–481.

10 Boutboul T., Akkerman A., Breskin A., Chechik R. Electron inelastic mean free path and stopping power modelling in alkali halides in the 50 eV–10 keV energy range. *Journal of Applied Physics*. 1996. Vol. 79, pp. 6714.

11 Eckstein W. *Computer Simulation of Ion-Solid Interactions*. Berlin, Heidelberg: Springer Berlin Heidelberg, 1991, 296 p.

12 Gervais B., Bouffard S. Simulation of the primary stage of the interaction of swift heavy ions with condensed matter. *Nuclear Instruments and Methods in Physics Research B*. 1994. Vol. 88, pp. 355–364.

13 Medvedev N.A., Rymzhanov R.A., Volkov A.E. Time-resolved electron kinetics in swift heavy ion irradiated solids. *Journal of Physics D: Applied Physics*. 2015. Vol. 48, pp. 355303.

14 Rymzhanov R.A., Medvedev N.A., Volkov A.E. Effects of model approximations for electron, hole, and photon transport in swift heavy ion tracks. *Nuclear Instruments and Methods in Physics Research B*. 2016. Vol. 388, pp. 41–52.

15 Rymzhanov R.A., Medvedev N.A., Volkov A.E. Monte-Carlo modeling of excitation of the electron subsystem of Al2O3 and polyethylene after swift heavy ion impact. *Nuclear Inst. and Methods in Physics Research B*. 2014. Vol. 326, pp. 238–242.

16 Rymzhanov R., Medvedev N.A., Volkov A.E. Damage threshold and structure of swift heavy ion tracks in Al2O3. *Journal of Physics D: Applied Physics*. 2017. Vol. 50, pp. 475301.

17 Terekhin P.N., Rymzhanov R.A., Gorbunov S.A., et al. Effect of valence holes on swift heavy ion track formation in Al2O3. *Nuclear Instruments and Methods in Physics Research B*. 2015. Vol. 354, pp. 200–204.

18 Ridgway M.C., Bierschenk T., Giulian R., et al. Tracks and Voids in Amorphous Ge Induced by Swift Heavy-Ion Irradiation. *Physical Review Letters*. 2013. Vol. 110, pp. 245502.

19 Rymzhanov R.A., Medvedev N., Volkov A.E., O'Connell J.H., Skuratov V.A. Overlap of swift heavy ion tracks in Al2O3. *Nuclear Instruments and Methods in Physics Research B*. 2018. Vol. 435, pp. 121–125.

20 Tao S., Chao H., Hailong D., et al. First principles study of structure, electronic and optical properties of Y3Fe5O12in cubic and trigonal phases. *Materials Science- Poland*. 2015. Vol. 33, pp. 169–174.

21 Henke B.L., Gullikson E.M., Davis J.C. X-Ray Interactions: Photoabsorption, Scattering, Transmission, and Reflection at E = 50-30,000 eV, Z = 1-92. *Atomic Data and Nuclear Data Tables*. 1993. Vol. 54, pp. 181–342.

22 Mott N.F., Massey H.S.W. *The Theory of Atomic Collisions*. London: Oxford University Press, 1985, 858 p.

23 Jenkins T. M. *Monte Carlo Transport of Electrons and Photons*. Boston, MA: Springer US, 1988, 656 p.

24 Wemple S.H., Blank S.L., Seman J.A., Biolsi W.A. Optical properties of epitaxial iron garnet thin films. *Physical Review B*. 1974. Vol. 9, pp. 2134–2144.

25 Littmark J.F., Ziegler J.P., Biersack U. *The Stopping and Range of Ions in Solids*. New York: Pergamon Press, 1985, 321 p.

26 Akkerman A., Boutboul T., Breskin A., et al. Inelastic Electron Interactions in the Energy Range 50 eV to 10 keV in Insulators: Alkali Halides and Metal Oxides. *physica status solidi (b)*. 1996. Vol. 198, pp. 769–784.

27 Lide D.R. *CRC Handbook of chemistry and physics*, 84th ed. Boca Raton: CRC Press, 2003, 2616 p.

28 Medvedev N., Volkov A.E. Reconciling anomalously fast heating rate in ion tracks with low electron-phonon coupling. 2021. Available at: https://arxiv.org/abs/2109.04401v1.

CONFORMATIONAL APPROACH TO DETERMINING THE POLARIZATION OF POLYETHYLENE OXIDE DURING MELT-CRYSTAL TRANSITIONS IN A NON-UNIFORM TEMPERATURE FIELD

Matveev N.N. [1], Lisitsyn V.I. [1], Arkhipov V.V. [2*]

[1]Department of General and Applied Physics, Voronezh State University of Forestry and Technologies named after G.F. Morozov, Voronezh, Russian Federation
[2]Department of General Physics, Moscow Institute of Physics and Technology (National Research University), Dolgoprudny, Russian Federation, E-mail: midav_73@mail.ru

In connection with the widespread use of polyethylene oxide (PEO) in modern technologies, studies of the relationship between its supramolecular structure and properties by modeling methods have recently intensified. Usually, when modeling the thermopolarized effect, the supramolecular structure of flexible-chain polymers is represented by a set of linear one-dimensional crystals. This approach does not take into account the conformational features of the structure of polymers. Using the example of (PEO), the article substantiates a method for calculating the influence of the conformations of a polymer molecule on the temperature dependence of the averaged square of the dipole moment of its molecules. The problem solved in this work, as well as the proposed solutions and approaches, reflect the general fundamental problem of the thermodynamic stability of multicomponent systems in external fields.

Keywords: conformations of molecules, flexible-chain polymers, polyethylene oxide, supramolecular structure, thermopolarization effect, inhomogeneous temperature field.

Introduction

In recent years, there has been a shift in interest in condensed matter physics towards studies of various classes of disordered and incompletely ordered materials. This broad area of research includes both crystalline and amorphous or glassy materials: polymers, amorphous semiconductors and dielectrics, spin and dipole glasses, relaxors, etc. The reason for this interest is the fact that disordered phases of condensed media occur incomparably more often, and in practical terms, they are no less important than idealized single crystals.

Many of the disordered polymeric materials exhibit metastable polarization, i.e. such a polarization that can be induced by various external fields (electric, magnetic, and, as shown in the work, inhomogeneous temperature). This polarization can be maintained indefinitely under certain conditions. In some crystallizing partially ordered polymers, not only the creation of induced polarization is possible, but also the occurrence of spontaneous polarization in the absence of external fields.

Since the role of electrically active polar polymeric dielectrics in the formation of the latest areas of electronic, computer, and measuring technology is growing sharply, it is undoubtedly that for their more effective use it is necessary to study in detail the regularities and mechanisms of the occurrence of electric polarization and the features of the real structure of these materials.

In this regard, on the example of polyethylene oxide (PEO), which is widely used in the above areas, studies of the relationship between its supramolecular structure and properties by modeling methods have intensified. Usually, when modeling the thermopolarization effect, the supramolecular structure of flexible-chain polymers is represented by a set of linear one-dimensional crystals. Within the framework of such approaches, the conformational feature of the polymer structure cannot be taken into account.

In modern technologies, polyethylene oxide (PEO) is used in powder metallurgy, mechanical engineering, metalworking, oil refining, agriculture, textile, leather, rubber, paper, chemical, mining and other industries. Based on PEO, lubricants, cutting fluids, solvents, anti-caking additives for bulk materials are produced, and they are also used in the conservation of wet wood [1–4]. Therefore, the study of its supramolecular structure to create materials with certain properties does not lose its relevance [5-6].

When constructing a model of the thermopolarization effect [7], the calculations are usually based on the assumption that the crystal structure is a set of linear one-dimensional crystals. It is clear that such a model cannot take into account the conformational features of the structure of flexible-chain linear polymers.

The paper proposes a method for taking into account the influence of conformations on the dependence of polarization on the temperature of a flexible-chain polymer. The proposed approach to the determination of polarization characteristics is considered on the example of polyethylene oxide (PEO), since the conformational structure of its macromolecule and the experimental values of polarization, pyroelectric coefficients, etc., obtained from thermograms of polarization and depolarization currents are known [8, 9].

When considering the conformational approach, we will use the following assumptions.

• The electric charge of the kinetic fragment of the macromolecule remains unchanged when the conformation of the chain changes.

• Any monomeric unit is considered electrically neutral.

• Interaction between macromolecules is not taken into account.

1. Theoretical part

It was shown in [10–11] that when a polymer (both synthetic and natural biopolymer) is introduced into an inhomogeneous temperature field, electric fields of thermal origin arise in it. As a result of orientational polarization at the interface with vacuum or metal, uncompensated bound charges of molecular nature appear on the polymer surface, the surface density of which coincides with the normal projection of the polarization vector:

$$\sigma_b = \pm P_n \tag{1}$$

If the polymer is at a constant temperature ($T = const$) in a state of thermodynamic equilibrium with an electric field whose strength is $\vec{E} = const$, the equilibrium value of polarization is determined by the thermal equation of state [12, 13]:

$$P_i = -n_0 \frac{kT}{Z} \frac{\partial Z}{\partial E_i} \qquad (i = x, y, z), \tag{2}$$

where $n_0 = \dfrac{\rho N_A}{\langle M \rangle}$ is the number of macromolecules per unit volume; ρ and $\langle M \rangle$ are the density and average molecular weight of the polymer, respectively; N_A is the Avogadro's number; k is the Boltzmann constant; Z is the integral of the states of an individual macromolecule in the field $\vec{E}$:

$$Z = \sum_l \exp\left\{ -\frac{1}{kT} \left[\varepsilon_l^0 - (\vec{p}\vec{E}) \right] \right\}. \tag{3}$$

In expression (3), the summation is carried out over all conformational states of each macromolecule with energy ε_l^0.

$$\vec{p}_n = \sum_n q_n \vec{r}_n, \tag{4}$$

where $\vec{p}_n$ is the dipole moment of a particular macromolecule with its node number n; q_n and $\vec{r}_n$ are the charge and radius-vector of this molecule in K_0 coordinate system. The coordinate system K_0 is chosen in the way that the OZ axis is parallel to the field.

As an example let's consider the structure of the PEO chain the structural formula of which is $-[CH_2 - CH_2 - O]_n -$ [14]. The conformational structure of PEO is a repeating unit consisting of three bonds (Fig. 1).

As is known, molecular conformations represent different states of a molecule with an unequal arrangement of atoms in space, arising from changes in the internal geometric parameters of the molecule, in particular, rotation angles around chemical bonds and bond angles (see, for an example, [15]). So, let's introduce into consideration the coordinate system K_1 associated with the rotating fragments of the molecule using the Euler angles. Let the axes OX_1 and OX is directed parallel to the first $C - O$ valence bond and the OZ_1 axis is parallel to the direction of the dipole moment of the molecule in the given conformation.
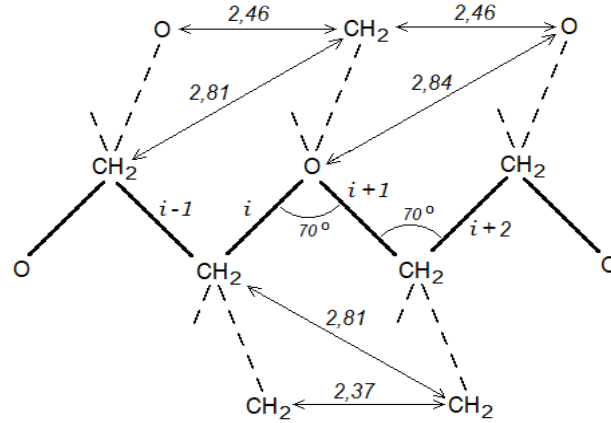
Fig.1. Conformational structure of the polyethylene oxide chain [15]. The $C-O$ and $C-C$ bond lengths are 1.43 Å and 1.53 Å, respectively; the angles complementary to valence are about 70º.
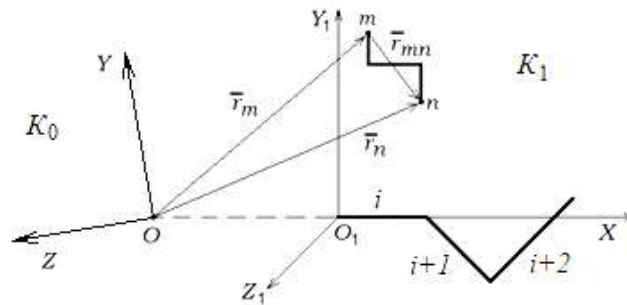
Fig.2. The orientation of coordinate axes.

Then the relationship between the system coordinates K_1 and K_0 is defined as follows [13] ($\varphi_1 = 0$, $\varphi_2 \in [0, \pi]$, $\varphi_3 \in [0, 2\pi]$):

$$x_1 = x \cos \varphi_3 - y \sin \varphi_3$$
$$y_1 = x \cos \varphi_2 \sin \varphi_3 + y \cos \varphi_2 \cos \varphi_3 - z \sin \varphi_2 \tag{5}$$
$$z_1 = x \sin \varphi_2 \sin \varphi_3 + y \sin \varphi_2 \cos \varphi_3 + z \cos \varphi_2$$

Let us write the state integral (3) in the system K_1:

$$Z = \sum_l \exp\left\{ -\frac{1}{kT}\left[\varepsilon_l^0 - E \cos \varphi_2 \sum_n q_n z_{1n} \right] \right\}, \tag{6}$$

where q_n is the charge of the n-th kinetic fragment of the macromolecule and dipole energy of the n-th kinetic fragment is

$$\varepsilon_p^n = Ep_n \cos \varphi_2 = E \cos \varphi_2 \sum_n \left(x \sin \varphi_2 \sin \varphi_3 + y \sin \varphi_2 \cos \varphi_3 + z \cos \varphi_2 \right)_n . \tag{7}$$

To calculate the polarization using formula (2), it is necessary to average over all possible orientations of the first valence bonds of all macromolecules located in a unit volume of PEO, i.e. integrate over the Euler angles. Let us first estimate the ratio of the dipole energy to the thermal energy at $T \approx 300 \, \text{K}$ and $E \approx 10$ V/cm, i.e. for a group of atoms with a size of ~10 valence bonds. This allows at considering polymers not having electret properties [16] to expand $\exp\left(\dfrac{\varepsilon_p^n}{kT} \right)$ into a series and restrict ourselves to the first non-vanishing terms.

Having carried out the necessary calculations and having made the indicated expansion into a series, after integrating over the angles φ_2 and φ_3, we obtain:

$$P_n = \alpha(T)E, \qquad (8)$$

where

$$\alpha(T) = -\frac{n_0}{kT} \frac{\sum p_l^2 \exp\left(-\frac{\varepsilon_l^0}{kT}\right)}{\sum \exp\left(-\frac{\varepsilon_l^0}{kT}\right)} = \frac{n_0}{3kT}\left\langle \vec{p}^2 \right\rangle \qquad (9)$$

$$p_l^2 = q_l^2(x^2 + y^2 + z^2)_l.$$

It can be seen from (9) that the value of $\alpha(T)$ is proportional to the square of the dipole moment of an individual macromolecule, averaged over all its conformations in the K_1 system, without taking into account the external electric field with strength E. Expressions (8) and (9) are outwardly similar to the corresponding expressions in [17] for dielectrics of any nature, the molecules of which, even in the absence of an external electric field, have a nonzero dipole moment. However, for PEO $\left\langle \vec{p}^2 \right\rangle$ is not a constant value and with a change in temperature leading to a change in conformation it changes.

2. Results and discussion

Thus, the calculation of the surface density of bound charges in an inhomogeneous temperature field reduces to averaging over all possible conformations of the squared dipole moment of one macromolecule in the K_1 coordinate system rigidly connected to the first valence bond of the macromolecule:

$$\sigma_b = \frac{N_A \rho E}{\langle M \rangle kT} \left\langle \vec{p}^2 \right\rangle. \qquad (10)$$

Since the surface charge density determines the polarization, i.e. $\sigma_b = P_n$, the expression (10) takes the form:

$$\left\langle \vec{p}^2 \right\rangle = \frac{3k\langle M \rangle}{N_A \rho E} PT. \qquad (11)$$

The value $a = \dfrac{3k\langle M \rangle}{N_A \rho E} = 1.7 \times 10^{-49}$ Qm⁴/K is a constant for a given polymer, where all input values (for PEO-15) are taken from tables and other data presented in the work [11]. Expression (11) and the data from [11] for the temperature dependence of polarization make it possible to graphically represent the character of the dependence $\left\langle \vec{p}^2 \right\rangle$ on temperature (Fig. 3).
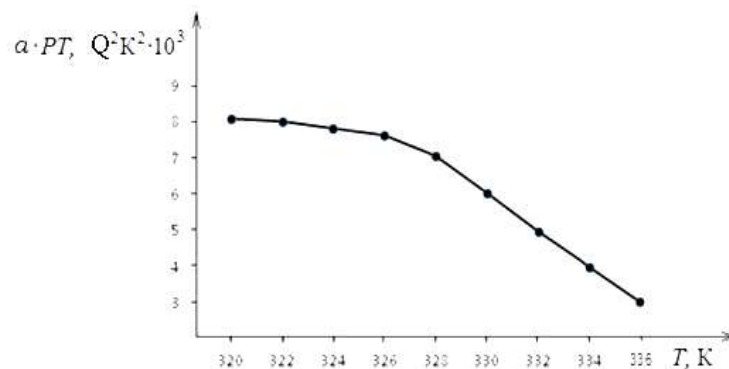
Fig.3. Dependence of the mean square dipole moment of PEO-15 on temperature.

The decrease $\left\langle \vec{p}^{\,2} \right\rangle$ shown by the graph with increasing temperature is due to the fact that the surface charge density decreases as a result of an increase in thermal motion

Conclusion

In conclusion, we note that many of the disordered dielectric materials have a metastable polarization, that is, a polarization that can be induced by various external fields, including an inhomogeneous temperature field. The experimental value of the polarization is determined by integrating the thermograms of the polarization currents, and the theoretical value is determined by using the model of a one-dimensional linear crystal. This model is rather simplified, since it does not take into account the conformation of the chain of the macromolecule. In this work, using the example of PEO, we show the possibility of determining the polarization taking into account the geometry of the kinetic fragments of the PEO macromolecule chain.

Comparison of the polarization determined by the formula (10) $P = 12$ μC/m^2 showed good agreement with experimentally data presented in the early works. The square of the dipole moment determined in this work is a very informative element of the polymer price structure. It depends on the mobility of its kinetic charge fragments, which form supramolecular structures. This is the most important factor for further investigation of the mechanisms of extended chain crystallization and folded chain crystallization using the mean square dipole moment of a particular polymer as a function of its molecular weight.

REFERENCES

1 Birshtein T.M. Conformations of Macromolecules and Intramolecular Conformational Transitions. *Polymer Science. Series A.* 2019. Vol. 61, No. 6, pp. 789-798.

2 Rud O.V., Birshtein T.M. Conformational Properties and Interaction of Polyelectrolyte Ph-Sensitive Stars. *Polymer Science. Series A*. 2013. Vol. 55, No.12, pp.757-771.

3 Polotsky A.A., Birshtein T.M., Borisov O.V., Daond M. Conformations Amphiphlite Polyelectrolyte Stars with Didblock Copolymer Arms. *Macromolecules*. 2013. Vol.46, No. 22, pp. 8999 – 9012.

4 Lange K.R. *Surfactants. Synthesis, properties, analysis, application*. St. Petersburg, Profession, 2007, 240 p.

5 Kuo C.Y., Huang Y.C., Hsiow C.Y., et al. Effect of side-chain architecture on the optical and crystalline properties of two-dimensional polythiophenes. *Macromolecules.* 2013. No. 46, pp. 5985-5997.

6 Tsvetkov N.V., et al. Conformational, optical, electro-optical, and dynamic characteristics of cross-linked poly (N-acryloyl-11-aminoundecanoic acid). *Colloid and Polymer Science*. 2014. Vol. 292, No. 10, pp. 2727-2733.

7 Matveev N.N., Kamalova N.S., Evsikova N.Yu. *Polarization phenomena in crystallizing polymers and biocomposite materials in a non-uniform temperature field.*. VSUFT, Voronezh, 2022, 310p. [in Rissian]

8 Korotkikh N.I., Matveev N.N., Sidorkin A.S. Pyroelectric Properties of Polyethylene Oxide. *Physics of the Solid State*. 2009. Vol. 51, No. 6, pp. 1290-1292.

9 Korotkikh N.I., Matveev N.N., Sidorkin A.S. Pyroelectric Properties of Polyethylene Oxide. *Physics of the Solid State*. 2009. Vol.51, No.6, pp.1290-1292.

10 Korotkich N.I., Matveev N.N., Kamalova N.S. Electric Fields of Thermal Origin in Crystallizing Polymers. *Bull. Russ. Acad. Sci.: Phys*. 2010. Vol. 74, No. 9, pp. 1314-1316. [in Russian]

11 Korotkikh N.I., Matveev N.N., Kamalova N.S. *Polarization of polyethylene oxide during phase transitions.* Saarbrucken: LapLamber, 2011, 89 p.

12 Yoshioka D. *Statistical Physics An Introduction.* Springer-Verlag, Berlin, Heidelberg, 2007, 206p.

13 Mandelkern L. *Crystallization of Polymers. Volume 1. Equilibrium concepts.* Cambridge University Press, New York, 2002, 448p.

14 Flory P. *Statistical Mechanics of Chain Molecules*. Mir, Moscow, 1971, 440 p. [in Russian]

15 Raju G.G. *Dielectrics in Electric Fields. Tables, Atoms, and Molecules.* CRC Press, Boca Raton, 2016, 796p.

16 Rychkov A.A., Rychkov D.A., Trofimov S.A. Electret State Stability in Surface Modified Polymers. *Izvestia: Herzen University Journal of Humanities & Sciences*. 2004. Vol. 4, No. 8, pp. 122-134. [in Russian]

17 Geyi W. *Foundations of Applied Electrodynamics*. John Wiley&Sons Ltd, Southern Gate, Chichester, West Sussex, 2010, 524 p.

MAGNETRON SPUTTERING OF PROTECTIVE COATINGS ON PARTS OF SURFACES OF PRODUCTS AND TOOLS USING MULTIELEMENT TARGETS MANUFACTURED USING A NEW TECHNOLOGY

Berdibekov A.T.[1], Laurinas V.Ch.[2]*, Dolya A.V.[1], Gruzin V.V.[1],
Guchenko S.A.[2], Tvardovsky A.N.[2]

[1]Research Institute of Arms and Military Equipment of the Military Research Center of the National Defense University named after the First President of the Republic of Kazakhstan – Elbasy, Nur-Sultan, Kazakhstan
[2]E.A. Buketov Karaganda University, Karaganda, Kazakhstan, vitas-laurinas@rambler.ru

Recently, the use of magnetron sputtering for the deposition of protective coatings has been intensively developed. The great prospect of using this method is due to the possibility of applying high-entropy coatings, which are used to protect surfaces that are simultaneously exposed to elevated temperatures, aggressive media and various types of wear. However, the use of the method of creating high-entropy coatings greatly hinders the absence in many cases of the required alloys, which have not only a certain qualitative elemental composition, but also a quantitative one. We managed to solve this problem by creating multi-element targets, with the help of which it becomes possible to create not only almost any elemental composition, but also to regulate the quantitative composition of elements. In this paper, we have proposed a method for manufacturing new types of targets for magnetron sputtering, with a detailed description of the technological chain of their manufacture. The novelty lies in the possibility of applying multi-element coatings when using one target. This is due to the fact that the number of different elements in the target can be measured in tens. The paper also presents the obtained positive result of using a target, which included five different metals, during magnetron sputtering.

Keywords: magnetron sputtering, protective coating, multi-element targets, high entropy coatings.

Introduction

The number of the Earth's population is growing rapidly, the number of various mechanisms necessary for people's lives and their comfort is increasing at an even faster pace, while the alloys from which they are made are becoming more and more difficult to manufacture and, accordingly, more expensive.

One of the ways to significantly save expensive metals (titanium, tungsten, molybdenum, nickel, etc.) is to apply protective coatings to parts made from simpler, cheaper alloys. In this case, the thickness of the deposited films usually lies in the range of several microns. Such an insignificant film thickness is quite enough to, for example, significantly improve corrosion resistance, heat and heat resistance, wear resistance, and also reduce the coefficient of friction of parts. Thus, coatings meet many parameters of operational and technological requirements.

There are many ways to deposit protective coatings [1], but the most promising are magnetron sputtering, ion and vacuum arc deposition [2]. These methods have a high degree of ionization, flux density and particle energy. Their wide range of deposited film parameters can be controlled by changing the substrate temperature, working gas pressure, substrate potential, and a number of other technological parameters.

1. Experiment technique

We have chosen the method of magnetron sputtering, which makes it possible to obtain coatings from almost any metals, alloys and semiconductor materials, and also, depending on the composition of the working atmosphere, to obtain films of oxides, nitrides, carbides, etc.

The aim of this work was the simultaneous deposition of a film using a single target consisting of Cr-Ni-Ti-Fe-Cu elements, which makes it possible to obtain a high-entropy coating.

To solve the tasks set, the technological chain given below was used.

At the first stage, the targets for magnetron sputtering were prepared. The metals that make up the future target were purchased pre-ground to an average of 50 microns. They were dosed in equal at.% and placed in the grinding jars of a ball mill. The grinding jars and balls were made from tungsten carbide. The mixture of metals placed in the grinding jars was poured with Nefras C2 - 80/120 gasoline and the ball mill worked for six hours. After grinding, the powder was separated from gasoline and sent for further drying for 4 hours, being in a vacuum hood.

After drying, the powder was sent for examination using a MIRA-3 LMU scanning electron microscope. The studies of the resulting powder using an electron microscope made it possible to find that, firstly, the grain size decreased, from an average of 50 microns to 2 microns, and secondly, the elemental composition of an individual grain after manipulation with a ball mill contains all the elements , which were in the grinding jar, and a good preservation of the proportion of elements (at.%) is recorded.

At the next stage of manufacturing targets for magnetron sputtering, disks 12 mm in diameter and 3 mm thick were created from micropowders pressed using a hydraulic press (20 tons). The small size of the discs was due to insufficient pressure to press the larger discs. After pressing, the discs were sintered in a vacuum furnace at a temperature of 800^0C for two hours and then cooled in a residual vacuum to room temperature. Due to the small size of the discs, a steel matrix (steel 08) was made in the form of a disc 100 mm in diameter and 10 mm thick. Round 3 mm recesses were milled into them with a diameter to fit the dimensions of the manufactured targets, which were then inserted into the matrix on a "hot" one. Fig.1 shows a view of an already working target, which consists of a matrix into which disks are inserted. The composition of the disks consists of Cr-Ni-Ti-Fe-Cu.

Fig.1. View of the target, consisting of a matrix and 21 disks.

We assume that the technology used to create targets by this method has the advantage of deposition of high-entropy coatings consisting of a large number of elements.

In order to check the possibility of creating disks for a target with a large number of elements, we conducted an experiment to obtain a mixture of 8 elements - Ni-Co-Fe-Ti-Cr-Zr-Mo-W. The choice of refractory metals was necessary to test the possibility of their sintering in vacuum at a relatively low temperature for them - 1000^0C. The manufacture of the disks was successful, they had quite sufficient strength, enough to be inserted into the mounting holes of the matrix.

Thus, it can be expected that the targets may contain several times more elements than five elements, which makes it possible to expand the range of physical and mechanical parameters of the deposited films.

At the final stage, in order to carry out magnetron sputtering of films using a prepared target, substrates were made, on which coatings are applied. In the manufacture of substrates, AISI 321 steel was used. The substrate is a hexagon with edges of 15 mm and a thickness of 5 mm. Both planes of the hexagon were ground on a surface grinder, one, which was subsequently coated, was polished on a polishing machine to a mirror finish, and final polishing took place in an electrolytic-plasma polishing bath. After unloading from

the bath, the part was washed in an ultrasonic bath and treated with steam using a steam jet device, wiped with coarse calico soaked in ethanol and placed in a drying cabinet and kept in it for two hours at a temperature of 150^0C.

Fig.2. Information - measuring device for determining the coefficient of sliding friction.

Fig.3. Tribometer.

To determine the coefficients of friction, the experimental setup "Information - measuring device for determining the coefficient of sliding friction" was used, the appearance of which is shown in Fig.2, and the tribometer shown in Fig.3 was used to measure wear resistance. Both devices were created by employees Scientific Research Center "Ion-plasma technologies and modern instrumentation" at E.A. Buketov KarU.

2. Results and discussion

The films were deposited in a chamber ion-plasma vacuum unit. NNV-6.6-I1, which in the basic configuration is designed for applying various single-layer and multilayer coatings on a wide range of metal products with a diameter of up to 200 mm and a length of up to 250 mm by the method of substance condensation with ion bombardment.

Instead of one of the three electric arc evaporators, we installed a magnetron, and instead of the second, a plasma source with an incandescent cathode, which makes it possible to clean their surfaces with a stream of ions (argon) by bombarding the substrates placed in the chamber before coating [3].

In the case of coating only one surface, the substrates are fixed and the coating is applied frontally. If it is necessary to apply a coating on the entire surface of the substrate, for example, during a further study of the heat and heat resistance of the sample, the entire surface of the substrates is polished, and the substrates in the installation chamber rotate both around their axis and rotate in a circle, with adjustable speeds of both rotations. The use of sample rotation makes it possible to deposit coatings on complex-shaped parts [4].

Thin films of Cr-Ni-Ti-Fe-Cu + Fe (~5 μm) were deposited on AISI 321 steel substrates by magnetron sputtering in an argon atmosphere in an NNV-6.6I1 vacuum setup. Additional contribution (Fe) of the target to the elemental composition of the coating, in addition to disks, a steel (steel 08) matrix contributed.

Fig.4 shows the spectrum taken from the central part of the disk obtained by the above method using a MIRA-3 LMU scanning electron microscope.

It should be noted that the difference in the elemental composition of the disc and the deposited film may be due to the difference in the "sticking" coefficients of the elements used. As for the "tail" of foreign elements observed in Fig.2, this is due to both the oxidation of the disks and the "dirt" that appeared during their pressing. Finishing cleaning with a filament cathode plasma source cleans both the substrates and the target, which allows you to get rid of the "tail" of foreign elements during coating deposition. In the first series of experiments, the coefficients of friction of disks and applied coatings were measured, since this

parameter is important for increasing the service life of the rubbing parts of mechanisms [5]. Fig.5 shows the spectrum taken from the coating on the substrate using a MIRA-3 LMU scanning electron microscope.
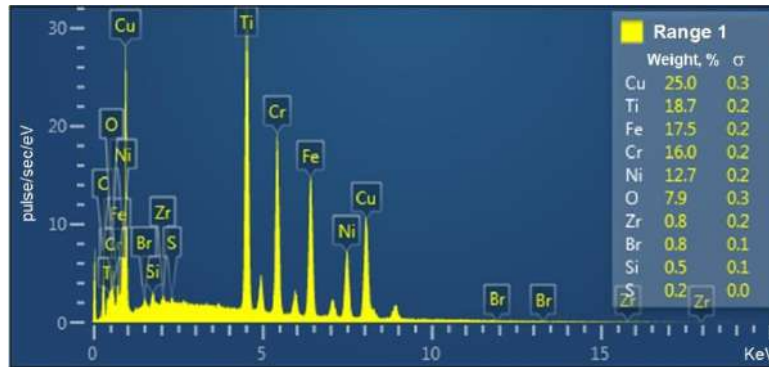
Fig.4. Spectrum taken from the central part of the target disk using a scanning electron microscope.
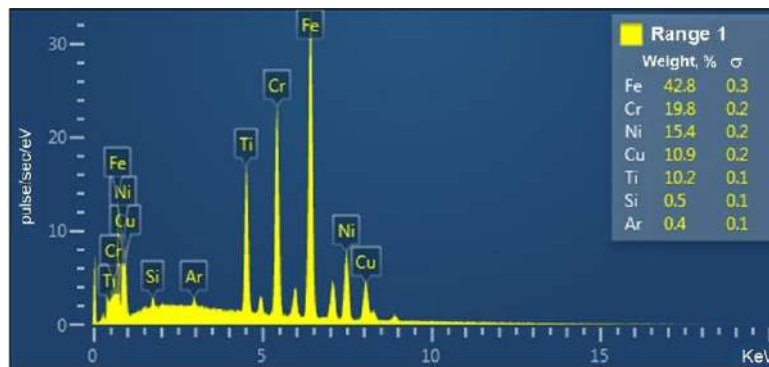
Fig.5. Spectrum taken from a coating on a substrate using a scanning electron microscope

For a more accurate result, measurements were taken 25 times on each metal plate. Copper, AISI 201 steel and aluminum plates were used. The results obtained are shown in table 1. In the second series of experiments, the Vickers microhardness of disks and deposited coatings was measured on an HVS-1000A device [6]. One sample was measured 10 times. The results obtained are shown in table 1. In the final series of experiments, the wear resistance of discs and applied coatings was measured [7].

During the rotation of a ball made of steel with high hardness, the coating wears out, and a spherical hole is formed in the film deposited on the substrate. The number of wells on one sample (20 pcs) was chosen so that the accuracy of the RADWAG AS60/220R2 electronic balance - 0.06 mg - was enough to obtain reliable information about the sample weight loss, and, at the same time, that the depth of the well did not exceed the thickness of the coating layer – 5 µm. In addition, similar measurements were carried out with substrates, the results of which for the measured coefficients of friction, microhardness and wear of AISI 321 steel are also shown in Table 1.

Table 1. The table shows the values of the coefficients of sliding friction, microhardness and abrasion rate of the multi-element disks, coatings and substrates that we have manufactured.

Object	Friction coefficient			Microhardness HV	Wear, µg/s
	on Al	on steel AISI 201	on Cu		
Disk Cr-Ni-Ti-Fe-Cu	0.09±0.006	0.07±0.006	0.11±0.007	580±0.4	0.3±0.07
Coating Cr-Ni-Ti-Fe-Cu+ Fe, on the substrate	0.07±0.003	0.06±0.003	0.08±0.004	790±0.2	0.1±0.06
Substrate AISI 321	0.10±0.003	0.25±0.002	0.39±0.003	363±0.3	0.4 ±0.03

Conclusion

The results obtained during testing the use of the above technological chain indicate that the applied composite multi-element coating Cr-Ni-Ti-Fe-Cu + Fe has a high microhardness and wear resistance, with relatively low values of friction coefficients. Thus, microhardness and wear resistance are several times higher than similar characteristics of the substrate material, and the coefficient of friction is at least 30% lower, which can increase the service life of machine parts and mechanisms.

Acknowledgments

REFERENCES

1 Reshetnyak E.N., Strelnitsky V.E. Synthesis of strengthening nanostructured coatings *Issues of Atomic Science and Technology*. 2008. No. 2. pp. 119-130. [in Russian]

2 Yurov V.M., Laurinas V.Ch., Guchenko S.A. et al. Structure and properties of multiphase ion-plasma coatings. Karaganda: Publishing and Printing Center of the Kazakh Russian University, 2013, 150 p. [in Russian]

3 Guchenko S.A., Eremin E.N., Zavatskaya O.N., et al Effect of N_2 and Ar on the properties of multicomponent ion-plasma coatings 12X18H10T+Cu+Al *IOP Conf. Series: Journal of Physics: Conf. Series.* 2019. 1260, 062009.

4 Eremin, E.N., Yurov, V.M., Laurynas, V.Ch. Influence of ION-plasma spraying regimes on the formation and properties of multi-element coatings *Journal of Physics: Conference Series,* 2020, 1441(1), 012006.

5 Cha S. (eds.) Consumption Due to Friction in Motored Vehicles and Low-Friction Coatings to Reduce It. *Springer International Publishing Switzerland: Coating Technology for Vehicle Applications*. 2015. 248 p.

6 Holmberg K., Erdemir A. Influence of tribology on global energy consumption, costs and emissions. *VTT Technical Research Centre of Finland,* 2017, 360 p.

7 Urbahs A. (eds.) Evaluation of the Physical and Mechanical Characteristics of Ion-Plasma Antifriction Coatings Based on Ti-Cu. *Trans Tech Publications Ltd, Switzerland: Key Engineering Materials Submitted,* 2018. 366 p.

INVESTIGATION OF THE ENERGY DEPENDENCE OF THE INTERACTION POTENTIALS OF THE ^{16}O+^{12}C NUCLEAR SYSTEM WITH A SEMI-MICROSCOPIC METHOD

Soldatkhan D.[1]*, Amangeldi N.[1,2], Baltabekov A.S.[3] Yergaliuly G.[1]

[1]L.N. Gumilyov Eurasian National University, Nur-Sultan, Kazakhstan; Soldathan.dauren@mail.ru
[2]Institute of nuclear physics, Almaty, Kazakhstan
[3]E.A. Buketov Karaganda University, Karaganda, Kazakhstan

The study of the collision of heavy ions with light nuclei at low energy is important in nuclear physics, thermonuclear energy, and astrophysics. The high-precision values of the nuclear system described at an energy close to the Coulomb barrier are used to control the synthesis of light nuclei inside thermosynthesis. For cross sections of reactions of light nuclei on the sun, plasma, and stars, we can use the parameters we have set. The article presents a microscopic approach to describing the process of nuclear-nuclear interaction. In the phenomenological approach, which determines empirical values based on comparison with experimental data, it is possible to find many sets of parameters with potentials that characterize the cross-section well. But the question arises which of them are real. Therefore, it is necessary to additionally describe microscopic potentials. For the same reason, a semi-microscopic analysis was carried out, which describes the imaginary part of the nuclear potential on the basis of an optical model, and the real part on a double-folding model. The folding potential is constructed depending on the effective nucleon-nucleon interaction based on the matrix element of two nucleons and the density of the nucleon distribution. As a result of the analysis, differential cross sections and optimal parameters were determined that well characterize the experimental cross sections of the ^{16}O+^{12}C nuclear system at energies E_{Lab}=20, 24, 36 MeV. The coefficients of normalization of differential cross sections, described on the basis of real microfolding potentials, were determined in the range N=0.85-1.0.

***Keywords**: elastic scattering, folding model, matter density distribution, nucleon-nucleon interaction.*

Introduction

Microscopic studies of the structural characteristics and mechanism of nuclear matter give their results. Based on the analysis of the scattering of composite particles in the nucleus at lower energy, it is possible to obtain important information about the properties of the internuclear potential [1]. To obtain information about the structure of nuclei and nuclear matter, it is necessary to know the mechanism of their interaction. To do this, it is necessary to construct nuclear-nuclear optical potentials and, on this basis, simulate the observed interaction characteristics.

As for the distribution of the density of nuclei, one of the fundamental achievements of recent times in this field is the discovery of expanded "tails" (halos) in the distribution of neutron and proton densities of light radioactive nuclei [2]. A detailed study of the differential cross-sections of elastic scattering of alpha particles and p-shell nuclei with nuclei led to the discovery of the phenomenon of "nuclear rainbow. In turn, it became necessary to introduce effective nucleon-nucleon forces depending both on the density of the nuclear medium in the area of mutual penetration of nuclei and on the collision energy of nuclei [3, 4]. The DF (Double-folding) model calculates the nuclear-nuclear potential using density-dependent of the 3 parameters of Michigan Yukawa (M3Y) interactions describing the density and energy dependence of the optical potential of the nucleon. Effective interaction is obtained by density-dependent forms by comparing the three elements selected in the Yukawa sum matrix. This model can describe the structure of the nucleus, since it is studied on the basis of summation of the central part of the nucleon-nucleon (NN) interaction with the ground states of the density of the beam ion and the target nucleus.

The article describes experimental elastic scattering cross-sections of the ^{16}O+^{12}C reaction with differential cross sections based on the standard optical model (OM). In addition, the DF model defines differential cross sections in which nuclear-nuclear potentials are constructed with effective forces NN.

.

Since the elastic scattering data clearly depend on the density of the distribution of matter in the nucleus, it is necessary to analyze the interaction of M3Y. The introduction of a real density dependence leads to a significant change in both the strength and the folding potential. The dependence on the same density is called the DDM3Y interaction [5]. In order to obtain the real part of micro folding potentials, density-dependent CDM3Y, BDM3Y DDM3Y types of effective M3Y interactions were used.

The study of the process of nuclear-nuclear interaction on the basis of theoretical ideas about the effective interaction of two nucleons gives reliable assumptions about the structure of the nucleus. The effective NN-interaction of m3u is carried out on the basis of the proton-neutron interaction matrix and the density distribution integral of nucleons. Microscopic analysis explicitly takes into account correlations based on effective NN forces to clarify the shape of the real part of the nuclear potential.

1. Construction of NN interaction potentials

The distribution of nuclear matter is constructed in a factorized form depending on coordinates and density in an effective interaction of the M3Y type [5]. The interaction potential of the beam nucleus and the target nucleus depends on the E/A_1 - nucleon energy and the density of the nuclei in the region of their overlap [6]. Equation of dependence of the optical potential of a nucleon on density and energy,

$$\upsilon_{D(EX)}(E,\rho,s) = g(E)f(\rho)\upsilon'_{D(EX)}(s), \tag{1}$$

where, $\upsilon_{D(EX)}$ - Direct (D) and Exchange (EX) potentials, $g(E)$ - dependence of potential on energy, $f(\rho)$ - density dependence function.

Effective NN potentials are determined by the sum of M3Y potentials in the region of interacting nuclei. Isoscalar and isovector M3Y potentials are parametrized as follows [6].

$$\vartheta_{0n}^{D(EX)} = \sum_{i=1,2,3} N_i \frac{e^{-\mu_j r}}{\mu_j r} \;. \tag{2}$$

Table 1. M3Y-Reid, M3Y-Paris N_i, μ_i parameters, and coefficients of potentials [7, 8]

N_i	i	N_1	N_2	N_3
Potential	μ_i , fm^{-1}	4.0	2.5	0.7072
M3Y-Reid	ϑ_{00}^{D}, MeV	7999.0	-2134.25	0
	ϑ_{00}^{EX} , MeV	4631.375	-1787.125	-7.8474
M3Y-Paris	ϑ_{00}^{D}, MeV	11061.625	-2537.5	0
	ϑ_{00}^{EX} , MeV	-1524.25	-518.75	-7.8474

At lower energies, it is important to clearly consider the effects of exchange. Therefore, effective NN takes into account direct, exchange components of interaction [8] and even, odd components of central forces [9]:

$$\upsilon_D(s) = 7999{,}0 \frac{e^{-4s}}{4s} - 2134{,}25 \frac{e^{-2,5s}}{2,5s}, \tag{3}$$

$$\upsilon_{EX}(s) = 4631{,}4 \frac{e^{-4s}}{4s} - 1787{,}1 \frac{e^{-2,5s}}{2,5s} - 7{,}8474 \frac{e^{-0,7072s}}{0,7072s}, \tag{4}$$

$\upsilon_D(s)$- the fraction of the third term of the direct potential is zero.

Direct and exchange component of effective M3Y interaction based on the G-matrix element of the Paris potential [17]:

$$\upsilon_D(s) = 11061,6 \frac{e^{-4s}}{4s} - 2537,5 \frac{e^{-2,5s}}{2,5s}, \quad (5)$$

$$\upsilon_{EX}(s) = -1524,0 \frac{e^{-4s}}{4s} - 518,8 \frac{e^{-2,5s}}{2,5s} - 7,8474 \frac{e^{-0,7072s}}{0,7072s}, \quad (6)$$

The direct part of the potential is completely elastic, only at the expense of the exchange component is absorption.

2. Construction of the density dependence function

Harmonic oscillator (HO) and Three-parameter Fermi - (3pF) models were used in the distribution of the density of the nuclei of the ^{16}O-beam and oh, ^{12}C-targets [12, 13]. The general form of the density dependence factor and the correlation function is determined by the following equation [14, 17]:

$$f(\rho) = C'_\rho(E)(1 + \alpha(E)e^{-\beta(E)(\rho_1 + \rho_2)}), \quad (7)$$

M3Y- Paris energy-dependent form of potential,

$$g(E) = (1 - 0.003E / A), \quad (8)$$

dependent density type CDM3Y:

$$f(\rho) = C'_\rho(E)(1 + \alpha(E)e^{-\beta(E)(\rho_1 + \rho_2)} - \gamma\rho(r)), \quad (9)$$

CDM3Yn (n=1) C_ρ, α, β, γ the parameters are given in Table 2 [15].
M3Y-Reid [2, 8, 9] energy-dependent type of potential:

$$g(E) = (1 - 0.002E / A), \quad (10)$$

M3Y-Reid for the potential, we use the form of density dependence in DM3Y [6].

$$f(\rho) = C(1 - \gamma\rho(r)), \quad (11)$$

BDM3Y1- Reid, C_ρ, γ - the parameters are given in Table 2.
DDM3Y0 The formula of the energy dependence of the potential in the d-independent form of interaction $g(E) = 276(1 - 0.005E / A)$ is applied.

Table 2. M3Y interaction coefficients depending on the density

Density-dependent version	C_ρ	a	β	γ
CDM3Y1-Paris	0.3429	3.0232	3.5512	0.5
BDM3Y1-Reid	1.2521	0.0	0.0	1.7452
DDM3Y0-Reid	1.0	0.0	0.0	0.0

The table shows n=1 for CDM3Yn, BDM3Yn interactions. In the article by Khoa Dao Tien [10, 18, 19], the dependence of the scattering density of the ^{16}O ion on the ^{12}C nucleus on CDM3Y-Paris, BDM3Y-Reid was analyzed. From here, the K-incompressibility parameter is selected, which is in good agreement with experimental values in the range of 150-210.

.

3. Discussions and results

Nuclear micro folding potentials for the $^{12}C+^{16}O$ nuclear system are calculated in the C++ program for energy of 20, 24, 35 MeV. M3Y-Reid, M3Y-Paris when calculating the potentials , the values of the density of nuclear matter were calculated using the formula [11].

$$\rho_0 = A \bigg/ (4\pi a^3 \sqrt{\pi}\left[\frac{1}{4}+\frac{3}{8}\alpha\right]),\qquad(12)$$

For the core of the ^{16}O beam, the values ρ_0 =0.17 fm^3 are assumed, for the core of the ^{12}C target ρ_0 =0.16 fm^3. As a result of the calculation, folding potentials were obtained depending on the density of CDM3Y1, BDM3Y1, DDM3Y0 at energies of 20, 24, 35 MeV for a nuclear system of $^{16}O+^{12}C$. We use this folding potential instead of the real part of the OM potential:

$$U(r) = NV_F(r) - iW_0 f(r, r_W, a_W) + V_C(r),\qquad(13)$$

where, N - the rationing factor, V_F - folding potentials, W_0 - imaginary potential, r_W, a_W - diffusion and radius of the imaginary potential, $V_C(r)$ - Coulomb potential.

The folding potential in this formula:

$$V_F = \iint \rho_1(r_1)\rho_2(r_2)\vartheta_{NN}(s)d^3r_1 d^3r_2,\quad s=r+r_2-r_1,\qquad(14)$$

where ϑ_{NN} - effective interaction potential NN, $\rho_1(r_1)$ and $\rho_2 (r_2)$ the distribution of the density of matter between the flying particle and the target nuclei, respectively.

(13) the real part of the optical potential in the localized folding potential formula is estimated within the density form. The parameters of the Woods-Saxon potential, obtained as an imaginary part of the potential, are determined by the Fresco program. Thus, based on the optical model, we obtain differential cross sections semi-microscopically. Figure 1-3.
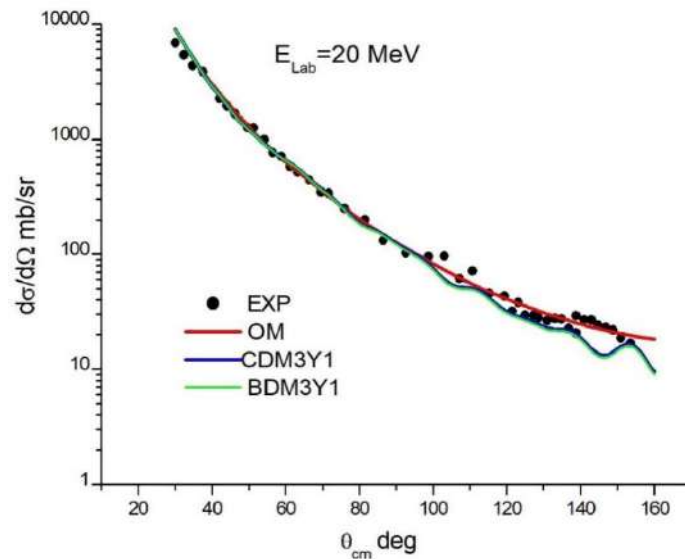
Fig.1. Cross sections of the $^{16}O+^{12}C$ system of OM and DFM at energy E_{Lab} = 20 MeV.
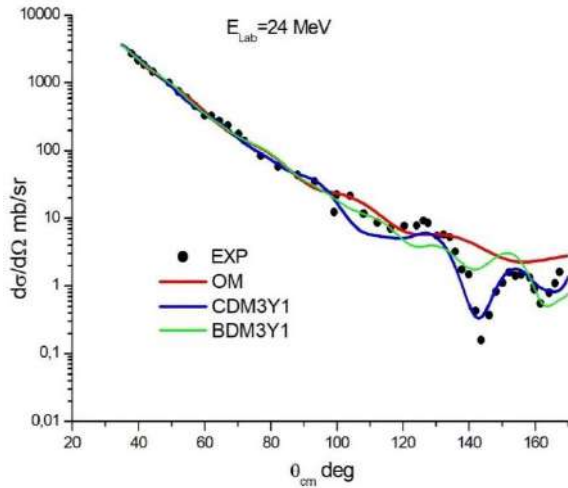
Fig.2. Cross sections of the $^{16}O+^{12}C$ system of OM and DFM at energy E_{Lab} = 24 MeV.
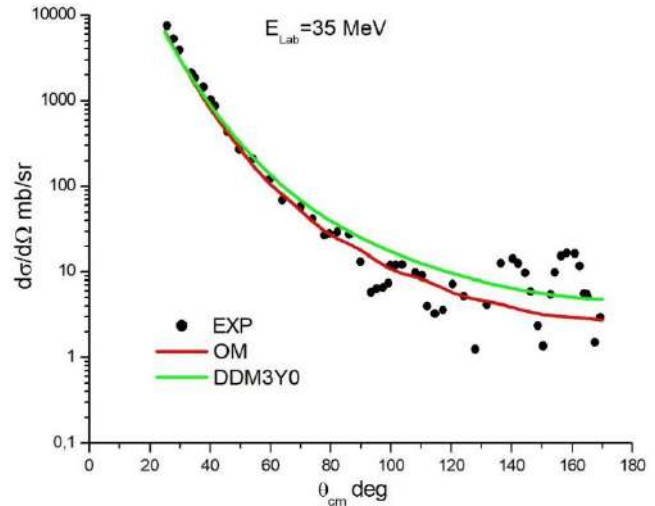
Fig.3. Cross sections of the $^{16}O+^{12}C$ system of OM and DFM at energy E_{Lab} = 35 MeV.

Differential cross sections depending on the determined density CDM3Y1, BDM3Y1, DDM3Y0 describe the experimental cross-section at a full angle. Experimental data in the studied nuclear system $^{16}O+^{12}C$ used the energies lab =20, 24, 35 MeV from the literature [16].

The following set of parameters describing the experimental data was determined: V_0 - real potential, W_0 - imaginary potential, a_r, a_w - diffuse of real, imaginary potential, Nr - coefficient of normalization, χ^2/N - error, Jv, Jw - integrals of the real and the imaginary potentials and σ - cross section (Table 3). The peculiarity of the analysis is that when searching for potentials, the radii of real, imaginary parts and the radii of coulombs were fixed.

Table 3. Parameters of the $^{16}O+^{12}C$ system at an energy of 20, 24, 35 MeV, DFM CDM3Y1, BDM3Y1, DDM3Y0, fix: r_r=1.2 fm, r_w=1,25 fm. r_C=1.3 fm.

E_{Lab}, MeV	Potential	V_0, MeV	a_r, fm	W_0, MeV	a_w, fm	N_r	χ^2/N	σ	Jv	Jw
20	OM	103.0	0.35	5.0	0.9		8.4	212	447.6	28.94
	CDM3Y1			5,0	0.9	0.9	4.0			
	BDM3Y1			5.0	0.9	0.9	2.5			
24	OM	105.0	0.465	5.97	0.407		1,4	476	468.52	29.58
	CDM3Y1			5,97	0,407	0.85	4.6			
	BDM3Y1			5.97	0.407	1.0	4.9			
35	OM	80.0	0.233	9.8	0.2		5.2	938	411.51	28.49
	DDM3Y0			9.8	0.2	0.8	7.2			

Conclusion

The folding potentials of M3Y-Read and M3Y-Paris effective NN interactions are determined. A semimicroscopic analysis of the $^{16}O+^{12}C$ nuclear system based on OM using core-core folding potentials has been carried out. The differential elastic scattering cross sections at energies E_{lab}=20, 24, 35 MeV were chosen for analysis within the framework of the optical model and the folding model (CDM3Y1, BDM3Y1, DDM3Y0). The variants BDM3Y1-Raid, CDM3Y1-Paris and DDB3Y1-Fatal are described only by the front (up to 90^0) angles, applicable to the experimental data of other authors [20].

In our work, up to 180^0 corners are described. The coefficient of N_r - normalization of differential cross sections constructed using folding potentials was found in the range of 0.8-1.0 (Table 3). The presence of an imaginary part of the potentials at a low energy of less than 10 MeV indicates the transparency (elasticity) of

the optical potential. The decrease in the real part and the increase in the imaginary part of the potentials from the energy dependence in laboratory energies at 20-35 MeV retains a global pattern. In accordance with the energy dependence of the real and imaginary potentials, the volume integral changes monotonically. It is important to solve the energy problem by applying the values of high-precision parameters determined at low energy to the synthesis of light nuclei inside thermosynthesis. When studying the cross section of the reaction of light nuclei on the sun, plasma and stars, it is possible to use the potentials (other parameters) of nuclear systems that we have determined.

Acknowledgments

REFERENCES

1 Khoa D.T., Knjaz'kov O.M. Obmennye effekty v yadro-yadernyh potencialah i yadernoe raduzhnoe rassejanie. *Fizika jelementarnyh chastic i atomnogo yadra*. 1990. Vol. 21, No. 6, pp. 1456-1498. [in Russian]

2 Tanihata I., Hamagaki H., Hashimoto O. Measurements of interaction cross sections and nuclear radii in the light p-shell region. *Physical Review Letters*. 1985. Vol. 55, No.24, pp. 2676. doi.org/10.1103/PhysRevLett.55.2676.

3 Khoa D.T. α-nucleus optical potential in the double-folding model. *Physical Review C*. 2001. Vol.*63, No.*3, pp. 034007. doi.org/10.1103/PhysRevC.63.034007.

4 Von Oertzen W., Khoa D.T., Bohlen H.G. At the end of the rainbow an understanding of nuclear matter. *Europhysics News*. 2000. Vol.31 No.2, pp. 5-9.

5 Kobos A.M., Brown B.A., Lindsay R. Folding-model analysis of elastic and inelastic α-particle scattering using a density-dependent force. *Nuclear Physics A*.1984. Vol. 425, No.2, pp. 205-232. doi: 10.1016/0375-9474(84)90073-3.

6 Lukyanov V.K., Zemlyanaya E.V. Total cross sections for nucleus-nucleus reactions within the Glauber-Sitenko approach for realistic distributions of nuclear matter. *Physics of Atomic Nuclei*. 2004. Vol.67, No.7, pp.1282-1298.

7 Anantaraman N., Toki H., Bertsch G.F. An effective interaction for inelastic scattering derived from the Paris potential. *Nuclear Physics A*. 1983. Vol.*398,* No.2, pp. 269-278. doi.org/10.1016/0375-9474(83)90487-6.

8 Satchler G.R. Direct Nuclear Reactions. *Oxford Univ. Press, New York*, 1983.

9 Bertsch G., Borysowicz J., McManus H. Interactions for inelastic scattering derived from realistic potentials. *Nuclear Physics A*. 1977. Vol.284, No.3, pp. 399-419. https://doi.org/10.1016/0375-9474(77)90392-X.

10 Khoa D.T, Oertzen V.W, Bohlen H.G. Double-Folding Model for Heavy ion Optical Potential: Revised and Applied to Study ^{12}C and ^{16}O Elastic Scattering. *Physical Review C*.1994. Vol.49, pp.1652-1667.

11 Ehrenberg H.F., Hofstadter R., Meyer-Berkhout U. High-energy electron scattering and the charge distribution of carbon-12 and oxygen-16. *Physical Review*. 1959. Vol.113, No.2, pp. 666.

12 De Jager C.W., De Vries H., De Vries C. Nuclear charge-and magnetization-density-distribution parameters from elastic electron scattering. *Atomic data and nuclear data tables*. 1974. Vol.14, No.5, pp. 479-508.

13 De Vries H., et al. Nuclear charge-density-distribution parameters from elastic electron scattering. *Atomic data and nuclear data tables*. 1987. Vol. 36(3), pp. 495-536. doi.org/10.1016/0092-640X(87)90013-1.

14 Gupta S.K., Sinha B. Intrinsic density and energy dependence: Exchange effects in alpha-nucleus scattering. *Physical Review C*. 1984. Vol.30 No.3, pp.1093. doi.org/10.1103/PhysRevC.30.1093.

15 Gontchar I.I., Chushnyakova M.V. A C-code for the double folding interaction potential of two spherical nuclei. *Computer Physics Communications*. 2010. Vol.181, No.1, pp.168-182.

16 Voos U.C., Von Oertzen W., Bock R. Optical-model analysis of the elastic scattering of complex nuclei at low energies. *Nuclear Physics A*, 1969. Vol.135. No.1, pp. 207-224. doi.org/10.1016/0375-9474(69)90159-6.

17 Khoa D.T., Satchler G.R., Von Oertzen W. Nuclear incompressibility and density dependent NN interactions in the folding model for nucleus-nucleus potentials. *Physical Review C*. 1997. Vol.56, No.2, pp. 954. doi.org/10.1103/PhysRevC.56.954.

18 Khoa D.T., Von Oertzen W. Refractive alpha-nucleus scattering: a probe for the incompressibility of cold nuclear matter. *Physics Letters B*. 1995. Vol.342 No.1, pp. 6-12. doi.org/10.1016/0370-2693(94)01393-Q.

19 Khoa D.T., Satchler G.R. Generalized folding model for elastic and inelastic nucleus–nucleus scattering using realistic density dependent nucleon–nucleon interaction. *Nuclear Physics A*. 2000. Vol.668, No.1, pp. 3-41.

20 Soldatkhan D., et al. New Measurements and Theoretical Analysis for the 16O+ 12C Nuclear System. *Brazilian Journal of Physics*. 2022. Vol. 52, No.5, pp. 1-10. doi.org/10.1007/s13538-022-01153-0.

METHANOL PRODUCTION UNITS OF MODULAR TYPE FOR INDUSTRY DECARBONIZATION

Zageris G. [1]*, Geza V. [1], Jakovics A.[1], Rodin L. [2], Homko A. [2], Kharitonov V. [2], Rogulyova M. [2]

[1]University of Latvia, Riga, Jelgavas Str. 3, Latvia,

[2]Encata LLC, Riga, Pulka Str. 3, Latvia

The production of carbon-containing chemicals is a way to decarbonize gas emissions. In particular, methanol (CH_3OH) can be produced from associated petroleum gas, which is currently flared. It makes sense to use simple methods of hydrocarbon gas conversion into synthesis gas, such as partial oxidation of methane to create small modular plants for direct operation in oil and gas fields. The numerical modelling of partial oxidation is considered, taking into account the kinetics of chemical processes and the design of the equipment. In this work the several models have been built to describe partial oxidation of natural gas with air - the equilibrium and complete 3D models which take into account the phenomena of mass and energy transfer, as well as chemical transformation. The main conclusion of the model comparison is that the full numerical model predicts incomplete oxidation quite well, while the simpler equilibrium model does not. In the future, the results of the numerical modelling of oxygen methane conversion will be investigated and presented.

Keywords: decarbonization, methanol production units, chemical reaction modeling, computational fluid dynamics, combustion, partial oxidation.

Introduction

Many industries emit carbon dioxide into the atmosphere, which leads to the greenhouse effect and climate change on the planet. In oil-producing fields, during the separation of oil, the so-called associated petroleum gas (APG) is released. It is a hydrocarbon gas consisting of methane, propane, ethane, and other higher methane homologues. At oil fields, where there are appropriate pipeline networks, APG is sent to gas processing plants, where the gas is subjected to standard cleaning and processing methods.

In some oil fields, APG is re-injected into oil-bearing formations. This measure allows temporary mothballing of gas but is extremely costly and inefficient. In oil fields where there is no gas processing, APG is partially used to generate electricity for their own needs, and the remaining gas is simply flared. Thus, about 150 billion m3 of APG are flared in the world annually, as a result of which more than 350 million tons of CO2 are released into the atmosphere [1] (see Fig.1).

Fig. 1. Burning flares in oil and gas fields.

This is not the only harm caused by APG flaring. Burning flares just warm the atmosphere. The amount of energy used to warm up the natural environment is equivalent to 750 billion kWh of electricity. This energy exceeds the combined annual consumption of all African countries [2].

In addition, APG flaring in the subarctic regions leads to the release of large amounts of soot, which settles on the snow cover, increases the absorption of solar energy and accelerates the melting of Arctic ice [3]. Burning flares worsen the general ecological state of the Earth's environment and make a significant contribution to global climate change. This situation negatively affects the entire population of the planet, regardless of where the flares are burning in Nigeria, the USA, Holland or Venezuela.

From [4] can be obtained that on average, the volume of gas burned in one flare is about 9 million m3/year (~1000 m3/hour). And it leads that about 22 thousand tons of CO2 and 70 thousand Gcal of heat per one flare being emitted into the atmosphere per year. Associated petroleum gas is quite a suitable hydrocarbon feedstock for methanol production. It is possible to produce 10 thousand tons of methanol per year from the specified volume of gas [5]. The environmental impact of this solution is obvious. Instead of emitting greenhouse gas into the atmosphere, a valuable chemical product is produced. The direct oil and gas fields' methanol production economy has many advantages since methanol is used as a hydrate inhibitor and can be consumed near its production. Currently, methanol is imported to the fields from large chemical complexes located at a great distance and its price is quite high.

There is one more important point to be made. Nowadays the world economy is on the "green transition" path, a reduction of the use of fossil sources of hydrocarbons and the move to renewable energy sources. In this regard, it may seem that innovative engineering related to oil and gas production has lost relevance, and CO2 emissions will disappear by themselves. But we need to understand that, on the one hand, the "green transition" will take decades, and on the other hand, the rejection of fossil fuels is planned in the field of energy. At the same time, fossil hydrocarbons will long remain the main raw material base for the chemical industry. Petrochemicals are rapidly becoming the largest driver of global oil consumption. They are set to account for more than a third of the growth in oil demand by 2030, and nearly half by 2050. Petrochemicals are also poised to consume an additional 56 billion cubic meters of natural gas by 2030 [16]. Therefore, the relevance of modular plants for the production of chemicals in the fields will remain in the future.

1. Methanol production unit description

The production of such a high-tech product as methanol (CH_3OH) directly at the fields must meet certain technical requirements that are not typical for traditional large-scale production. One of the main requirements for such units is their compactness and block-modular design. The dimensions of the equipment of plants with a capacity of 1-10 thousand tons/year fully comply with the requirements of the block-modular design. Such container manufacturing of units greatly simplifies their installation at oil and gas fields and dismantling when moving units to other fields.

We have developed a process flow diagram for a methanol production unit that meets the requirements of compact production. Its block diagram is shown in Fig.2. The methanol production scheme consists of the following technological blocks:
- Desulphurization of hydrocarbon raw materials.
- Raw material conversion.
- Methanol synthesis.
- Rectification of raw methanol.

To remove sulfur compounds, instead of the traditional two-stage scheme, a one-stage scheme is used, with a bifunctional catalyst, on which the processes of hydrogenation of organosulfur compounds to hydrogen sulphide and hydrogen sulfide adsorption take place [6, p.27]:

$$RSH \; + \; H_2 \; = \; H_2S \; + \; RH \quad (hydrogenation)$$

$$H_2S \; + \; ZnO \; = \; ZnS \; + \; H_2O \quad (adsorption)$$
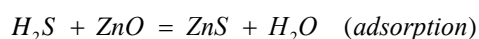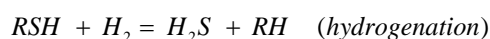
For the conversion of hydrocarbon feedstocks, the traditional solution in large-scale production is steam reforming in a tube furnace. Source [6, p.54] describes the basics of the process and gives an example of industrial application. This is a complex structure, difficult to minimize in size, with the production of a large amount of steam, which is used to drive powerful compressors. For mini-units, the compressors use electric drives and the steam requirement is significantly lower. For these reasons, as well as other technical reasons,

for a compact plant, the optimal option for the conversion is partial oxidation or steam-oxygen conversion of natural gas [8, p.217].
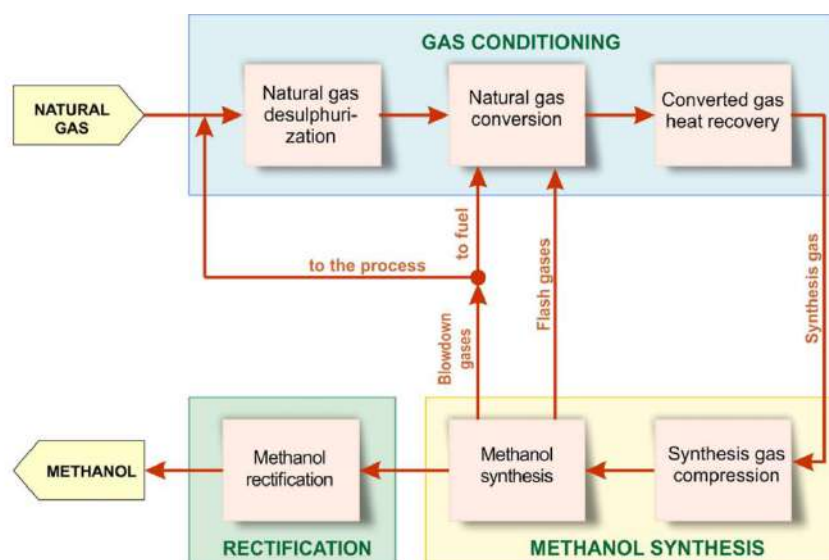
Fig.2 Methanol production block diagram.

The chemical mechanism of this process can be described in a simplified form as follows:

$$CH_4 + 0.5 \cdot O_2 = CO + 2 \cdot H_2$$
$$CH_4 + H_2O = CO + 3 \cdot H_2$$
$$CO_2 + H_2 = CO + H_2O$$
$$CO + 0.5 \cdot O_2 = CO_2$$
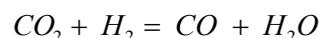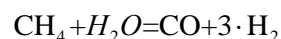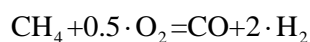
This solution provides small dimensions of the natural gas conversion reactor and the best composition of the synthesis gas obtained in the process of conversion, which is characterized by the functional:

$$F = \frac{X_{H2} - X_{CO2}}{X_{CO2} + X_{CO}}, \tag{1}$$

where X_i - volume concentrations of the respective components.

The better feedstock processing into methanol is achieved at a certain ratio of H2:CO:CO2 in the syngas composition. In this case, a value of the functional is close to 2.

The synthesis of methanol is carried out according to the circulation scheme in a compact tubular isothermal reactor according to the following reactions [7]:

$$CO_2 + 3H_2 = CH_3OH + H_2O + Q$$
$$CO + 2H_2 = CH_3OH + Q$$
$$CO_2 + H_2 = CO + H_2O - Q$$
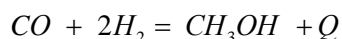
Rectification of raw methanol for a compact unit is provided according to a simplified single-column scheme.

2. Natural gas partial oxidation mathematical simulation

Natural gas partial oxidation is an understudied object in terms of process mathematical modelling. Existing traditional approaches, based on thermodynamics, do allow to obtain only values of conversion reactor output composition and heat of reaction to get a material and heat balance of both synthesis gas production in particular and methanol production in general and accordingly calculate all the technological characteristics and consumption factors. The task of developing and designing of partial oxidation reactor is

solved by a large number of experimental studies to optimize the geometry of the mixing unit and combustion chamber. A detailed mathematical model of natural gas partial oxidation is intended to replace a significant amount of experimental studies with a computational experiment stage. Various studies show good correlation between numerical models based on finite volume method. Simple 1D models are capable to predict output gas content in catalytic methane partial oxidation [13]. More complex models involve full 3D resolution of methane oxidation equipment [14]. Such models ensure reliable prediction of gas composition and flame characteristics. Although models have certain drawbacks (e.g. temperature tends to be overpredicted when using Eddy Dissipation Concept), results of these models provide valuable details for understanding of processes within the equipment.

That is why it goal of this paper to study the regularities of the interaction of gaseous hydrocarbons with oxygen and water vapour and develop a mathematical model of the partial oxidation process, based on kinetic relationships, and solutions of the equations of hydrodynamics and heat transfer.

3. Description of natural gas partial oxidation engineering calculation method

Traditional approaches based on thermodynamics give opportunities to calculate equilibrium composition and heat of chemical reactions i.e. composition and temperature of outlet stream without relation to the reaction time. Chemical equilibrium can be described by the following system of algebraic equations (in matrix form):

$$ln(Kp_i) = \sum_{j}^{m} (S_{i,j} \cdot ln(p_j))$$

(2)

Where m is the reaction number, j is the substance number, Kp_i is the equilibrium constant of reaction i, S_{ij} is the stoichiometric matrix and p_j is the composition vector for partial pressures.

Equilibrium constant Kp_i may be expressed through the thermodynamic relation:

$$\ln(Kp_i) = -\frac{dG_i}{RT}$$

(3)

dG_i- Gibbs energy change in the reaction i, expressed through thermodynamic parameters and R, T - universal gas constant and absolute temperature respectively.

The methodology for calculating the equilibrium composition and temperature consists of the following steps:

1. Selection of the list of substances and the basis of the reactions – a list of linearly independent reactions. For engineering purposes, only initial and final substances are taken into account and they are chosen so that the basis does not have a large dimension. The mathematical representation of the reaction basis is a stoichiometric matrix S_{ij}, rows of which correspond to reactions and columns to stoichiometric coefficients. For example, in the case of partial oxidation of methane without taking into account soot formation, the reaction basis can be written as:

$$CH_4 + 0.5 \cdot O_2 = CO + 2 \cdot H_2$$
$$CH_4 + H_2O = CO + 3 \cdot H_2$$
$$CO + H_2O = CO_2 + H_2$$
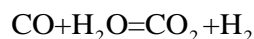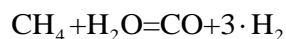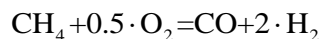
2. Choice of a method for calculating values of equilibrium constants as a function of temperature. In the simplest case, one can use table values from a handbook. The other way is to use empirical dependencies of the form $\ln(Kp_i) = a_i + b_iT + c_iT^2 + d_iT^3 + e_iT^4$, where a_i, b_i, c_i, d_i and e_i are empirical coefficients. Also, the equilibrium constant can be calculated from the thermodynamic relation given above (eq. 3).

3. At given initial values of T, P and p_j^0 the system of equations (eq. 2) is solved for example, by the Newton-Raphson method to obtain an equilibrium composition. Calculation of equilibrium temperature by solving heat balance equation:

$$H_{out} - H_{in} = Q(T, P, p_i).$$

(4)

Here, H_{out}, H_{in} are output and input enthalpies $Q(T, P, p_i)$ is heat flux and T, P, p_i are temperature, pressure and composition respectively.

The dependence of heat flux on T, P, p_i is determined by the heat transfer conditions in each particular reactor heat exchanger and is calculated by formulas widely available in the literature, e.g., in [15]. The case of $Q(T, P, p_i) = 0$ is for an adiabatic reactor. These equations are solved together with the system described by eq. 2 by iterative methods to find out the temperatures that make them true. Since the process of synthesis gas production by partial oxidation reaches equilibrium, the results of equilibrium calculations can serve to estimate the output compositions and temperatures obtained on the complex numerical model.

4. Gas flow numerical modeling

In contrast to model described in previous section, model described in this section calculates local spatial distribution of physical quantities and chemical species thus allowing more detailed study of underlying processes. To appropriately study the combustive processes within a natural gas reactor, one must adequately model the flow of the gas, thermal transport, and chemical reactions. A lot of care must especially be taken with modelling turbulent flows, as this also feeds into the calculations relating to chemistry. In this study, the Navier-Stokes equations that govern incompressible fluid flow are used, as the fluid in consideration is a gas in subsonic flow. The equations are solved in the Reynolds-averaged (RANS) approach:

$$\frac{\partial}{\partial t}\overline{\rho} + \frac{\partial}{\partial x_j}\left(\overline{\rho}\,\overline{v}_j + \overline{\rho'\,v'_j}\right) = 0 \tag{5}$$

$$\rho\frac{\partial \overline{v}_i}{\partial t} + \rho\frac{\partial}{\partial x_j}\overline{v}_j\overline{v}_i = \frac{\partial}{\partial x_j}\left(\mu\left(\frac{\partial \overline{v}_i}{\partial x_j} + \frac{\partial \overline{v}_j}{\partial x_i}\right) - \overline{p}\delta_{ij} - \rho\overline{v'_i v'_j}\right) + f_i \tag{6}$$

Here, ρ is density, v_i is the i-th component of velocity, p is pressure, μ is viscosity and f_i are additional volume forces/sources. The apostrophe symbol denotes turbulent pulsations for these quantities.

These equations require closure for the Reynolds stress term $\rho\overline{v'_i v'_j}$. In this study, the $k - \varepsilon$ model, which allows for calculation of the turbulence energy k and turbulent dissipation ε, is employed:

$$\frac{\partial(\rho k)}{\partial t} + \frac{\partial}{\partial x_i}(\rho k v_i) = \frac{\partial}{\partial x_j}\left[\left(\mu + \frac{\mu_t}{\sigma_k}\right)\frac{\partial k}{\partial x_j}\right] + G_k - \rho\varepsilon \tag{7}$$

$$\frac{\partial(\rho \varepsilon)}{\partial t} + \frac{\partial}{\partial x_i}(\rho \varepsilon v_i) = \frac{\partial}{\partial x_j}\left[\left(\mu + \frac{\mu_t}{\sigma_\varepsilon}\right)\frac{\partial \varepsilon}{\partial x_j}\right] + C_1\frac{\varepsilon}{k}G_k - C_2\frac{\rho\varepsilon^2}{k} \tag{8}$$

$\mu_t = \frac{\rho C_\mu k^2}{\varepsilon}$ is turbulent viscosity, $C_1 = 1.44, C_2 = 1.92, C_\mu = 0.09, \sigma_k = 1.0, \sigma_\varepsilon = 1.3$ are empirical constants and $G_k = -\rho\overline{v'_i v'_j}\frac{\partial v_j}{\partial x_i}$ acts as a source term for turbulence.

Because this study deals with chemical reactions, it is imperative to also model thermal transport. This is done via the energy equation:

$$\frac{\partial(\rho E)}{\partial t} + \nabla\left(\vec{v}(\rho E + p)\right) = \nabla\left(k_{\text{eff}}\nabla T - \sum h_j \vec{J}_j + \left(\vec{\vec{\tau}}_{\text{eff}} \cdot \vec{v}\right)\right) + S_h \tag{9}$$

E is energy, T is temperature, k_{eff} is the effective conductivity (which is the sum of the molecular and turbulent conductivities), $\vec{J}_j$ is the diffusive flux of the j-th species, h_j is the sensible enthalpy of the j-th species, $\vec{\vec{\tau}}_{\text{eff}}$ is the total stress tensor (due to molecular and turbulent viscosity), S_h is a source term, in this case heat produced or consumed by reactions.

Both of the hitherto considered approaches together with chemistry modeling are dependent on one another – chemical reaction rates are determined by turbulence, they consequently produce or reduce heat, which can change the temperature locally, thus locally changing e.g. the density of the mixture, changing the flow characteristics. Because of this feedback loop, care must be taken to adequately model all of these processes in a unified framework. Thus, a more detailed will be provided for chemical reaction modeling.

5. Chemical reaction modeling

Chemical reactions are often of interest in many industrial applications, particularly ones that include combustive processes. For example, the production of syngas is often the result of complex, multiple step chemical reactions with many species involved in the process. To build a fully descriptive numerical model for such processes, chemistry must be adequately taken in account. Furthermore, one must also take in account the medium that the reactions take place in.

The transport of each chemical species is described by the species transport equation [6]:

$$\frac{\partial(\rho Y_i)}{\partial t} + \nabla \cdot (\rho \vec{v} Y_i) = -\nabla \cdot \vec{J}_i + R_i \tag{10}$$

Here, the left-hand side is the material derivative for Y_i, which is the mass fraction of the i-th species, J_i is the diffusion flux of that species, R_i is a production term (which is typically determined by the chemical reactions taking place).

To determine the R_i term, the chemical reactions taking place must be considered. The reactions that take place in each process are often known beforehand, but an accurate description of these reactions requires the knowledge of constants that determine the rate of each reaction, and the relation of these constants to parameters such as pressure or temperature, which can vary greatly as the reactions evolve, or otherwise a priori assumptions are required that allow for the reaction rates to be discarded from the model. These things have previously been studied at length, especially for often used technological processes, and are available as empirical data tables for some given ranges of parameters.

5.1 GRI-Mech 3.0

Natural gas combustion is quite a complex process, because natural gas itself is constituted of multiple species (typically mainly of methane, but also of higher alkanes and traces of carbon dioxide, nitrogen, hydrogen sulfide and/or helium) and because the species in the gas can undergo many different reaction mechanisms. One description of the combustion of natural gas is in GRI-Mech 3.0, an aggregation of research data from the University of Berkeley [7]. Altogether, GRI-Mech 3.0 describes 53 species and 325 reactions. It is both based in a lot of research as described in [7] and has been extensively used to describe combustion with good success. GRI-Mech 3.0 is written in the CHEMKIN file format. CHEMKIN files are written in a certain syntax and used to describe reaction mechanisms, reaction rate constants and the thermodynamic properties of the species in a certain temperature range, also denoted inside the file. The GRI-Mech 3.0 library is open-source and freely available.

5.2 Eddy dissipation concept model

Chemical reactions are also strongly dependent on the medium they occur in. Temperature and pressure are important parameters to chemical reactions, however, adequately describing the mixing of the reactive species is also crucial to accurately describe the relevant chemistry. This is even more crucial in turbulent flows, where mixing happens at the smaller, turbulent scales and must be taken in account.

The *Eddy-Dissipation-Concept model* is an extension of the eddy-dissipation model by Magnussen [8] [9] which takes in account that chemical reactions take place in the finest turbulent scales. The volume fraction is calculated as follows:

$$(\xi^*)^3 = C_\xi^3 \left(\frac{\nu \varepsilon}{k^2}\right)^{3/4} \tag{11}$$

Here, ν is kinematic viscosity and C_ξ is a volume fraction constant and ξ^* is the turbulent length scale. The chemical reactions occur over a turbulent fine structure time scale, which is described as follows:

$$\tau^* = C_\tau \left(\frac{\nu}{\varepsilon}\right)^{1/2} \tag{12}$$

Here, C_τ is a time scale constant.

In these scales, then, reactions can be modeled with submodels according to the finite Arrhenius rates. This model takes in account both the laminar rate of the reaction and the mixing at a certain point of the gas. Furthermore, it allows for combustion modelling without the requirement for a spark.

5.3 Practical implementation in ANSYS Fluent

ANSYS Fluent is one of the software solutions capable of both modeling gas flow (k-ε turbulence and energy transport) and chemical reactions within it with the eddy dissipation method (among others). However, one should note that ANSYS Fluent is commercial software and thus requires a license to run. It also supports the use of CHEMKIN files for specifying the chemistry mechanics, which is GRI-Mech 3.0 in this case.

ANSYS Fluent offers the option to integrate chemistry via direct integration, which is computationally expensive. However, there is an alternate option - the ISAT (in situ adaptive tabulation) method. Solving chemistry with ISAT can lead to approximately 100 times faster solutions. The basic idea of ISAT is that it begins with direct integration and saves the calculations in a table. As the table expands, in some cases, the calculations can simply be looked up in the table (or rather interpolated with some set precision) instead of performing a full calculation. Generally, the longer the simulation goes, the larger the table becomes and there is less need for direct integration, thus greatly speeding up calculations.

6. Numerical model for the ENCATA gas reactor

A numerical model simulating gas flow and chemical reactions was formulated for a particular gas reactor according to the specifications of ENCATA LLC. A sketch of the design (and of the computational mesh) can be seen in Fig. 3. The mesh constructed for the 3D case consists of 350k tetrahedral elements, which are more refined near the walls and where the reaction zones are predicted to be most active (in order to capture the fast chemistry going on). This mesh size has been arrived at after completing a mesh independence sub-study. As can be seen, the case is solved for 1/8th of the geometry by using the underlying symmetry of the geometry. This allows for faster computing times, which are otherwise very extensive due to the computing costs of solving for chemistry.
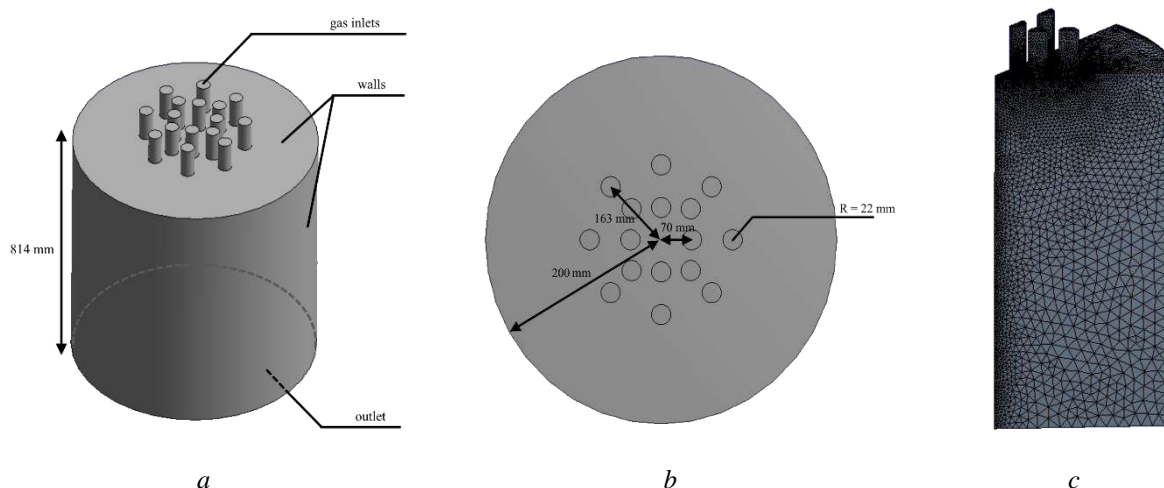
Fig. 3. A sketch of (a) the 3D reaction geometry with labels and height (b) the top of the 3D model with measurements (c) the computational mesh.

The mix of natural gas and air is fed through the inlets according to ENCATA LLC specifications see Table 1. In the computational model, it is fed in already as a premixed, homogeneous mixture. The total mass inflow through the inlets is 0.166 kg/s. The walls of the reactor are modelled as adiabatic. All the thermochemical data of each constituent element in the gas mixture is given via GRI-Mech 3.0. The calculations are performed first by using GRIMech 3.0, then by using a simplified natural gas combustion reaction set. This is done in the hopes that a simplified chemistry description can adequately describe the output gas, as chemical calculations take up the vast majority of the computational costs.

The simplified reaction mechanism is described in [17]. Originally it was used for calculating gasification of coal in combination with heterogenous reactions. The model is solved as a stationary and time-averaged (in

terms of turbulent quantities) case. The resultant gas output is compared to that of the empirically tested values known by ENCATA.

Table 1. Composition of input gas

Mixture component	Mass fraction, % (mass)
CH_4	5.870
CO_2	0.133
C_2H_6	0.346
C_3H_8	0.102
C_4H_{10}	0.034
C_5H_{12}	0.028
N_2	70.506
O_2	21.525
Ar	1.193
H_2O	0.263

7. Results

Upon completing the described calculations, one can examine the main characteristics of the solution – the temperature field, reaction heat field and integral values of the species at the outflow, as well as the average temperature at the outflow.

First, upon analyzing the temperature fields (Fig. 4), one can see that the full and simplified chemical models give different results for the equilibrium temperature achieved in the reactor, with the simplified reaction set giving a higher average temperature. However, the characteristics of the temperature field are similar in both cases.

Secondly, when considering the reaction heat fields, further agreement can be found. The characteristic zones of reaction are quite similar in both cases, with the simplified reaction set once again giving slightly higher results. This is likely the reason for the higher temperatures.

In Table 2, the output gas compositions of the two cases are compared and set against ENCATAs own in-house model results. It must immediately be noted that the full chemistry model with GRIMech 3.0 gives a good estimate for the output gas, with each species generally differing from ENCATAs results by less than 0.5 mol%.

Table 2. Comparison of output values in various models

Gases at outlet	ENCATA equilibrium model, mol%	GRIMech 3.0. model, mol%	Simplified chemistry model, mol%
H_2	2.20	2.52	0.21
CO	4.00	4.50	3.05
CO_2	6.70	6.49	7.02
H_2O	19.10	18.81	20.03
N_2	67.20	66.70	69.68
Ar	0.80	0.83	-
Other	-	0.15	0.01
Average T, °C	2048	1868	2055

However, the average temperature at the outlet is markedly lower when compared to ENCATA modelling results. On the flipside, the simplified chemistry model forecasts the output gas worse than the full model does, but the temperature obtained at the outlet is much closer to the ENCATA benchmark. This leads to an interesting question regarding the fact that one model forecasts output gas composition better, the other better forecasts the output gas temperature. Further work will be required to determine the cause for this, as outside effects can be the culprit (e.g. in the scope of this work radiation modelling has been neglected – upon including radiation calculations, the temperature fields could change).

Overall, the authors arrive at the conclusion that a simplified chemistry model nevertheless describes the output gas composition too poorly in order to be a good substitute for the full GRIMech 3.0 chemistry set. Work is still required to see whether intermediate chemistry sets that are smaller than GRIMech but more expansive than the one considered in this paper may be used to cut computational costs. For engineering and design purposes a model that quickly returns results is required for it to be feasible in everyday use.
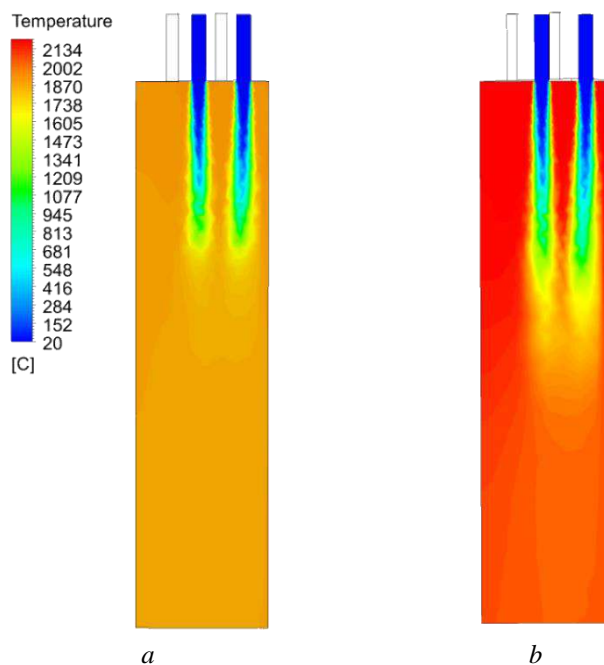
Fig. 4. The temperature field for the models with (a) GRIMech 3.0 chemistry (b) simplified chemistry.
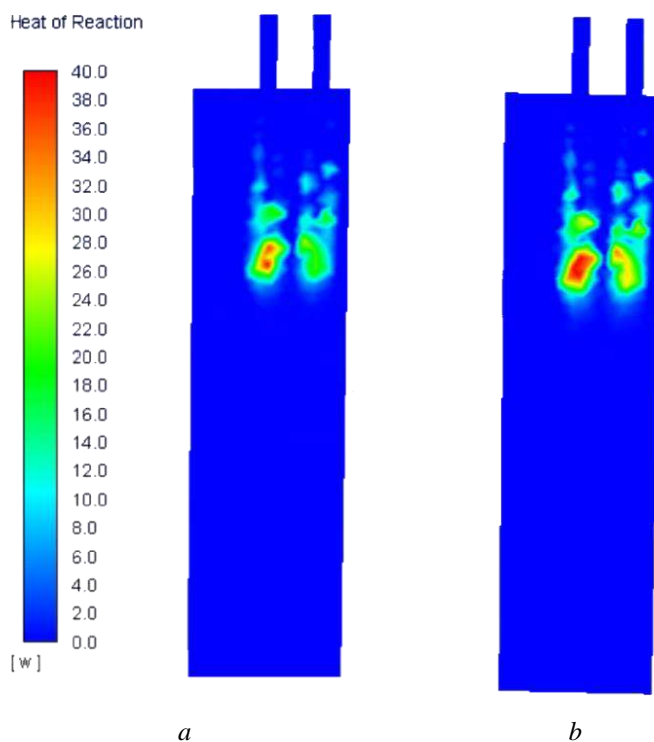
Fig. 5. The reaction heat field for the models with (a) GRIMech 3.0 chemistry (b) simplified chemistry.

Conclusion

Having constructed two models (full GRIMech 3.0 chemistry and a simplified reaction set) for the combustion of natural gas in a reactor, one can conclude the following:

− The two reaction sets produce reasonably close results for temperature and reaction heat fields qualitatively, with the (slight) differences being in quantitative values.

− The full chemistry set produces a good forecast for the composition of the output gas but underestimates the output temperature. The simplified model fails to adequately forecast the output gas composition; however, it gives a better agreement for the output temperature.

− The simplified reaction set considered in this study cannot be used to adequately forecast the output gas. Further work is required to see if intermediate reaction schemes smaller than GRIMech 3.0 exist that can give better results and allow for cutting computational costs.

Further work includes considering other reaction sets for natural gas combustion, as well as more thoroughly studying the effects of variations added to the model (e.g. adding radiation modeling, varying model constants etc.).

REFERENCES

1 Zero Routine Flaring by 2030. World Bank Initiative. Available at: thedocs.worldbank.org/en/doc/ -0400072021/zrf-initiative-text-list-map-98 (Dec13, 2021).

2 New Data Reveals Uptick in Global Gas Flaring. World Bank press release. Available at: www.world bank. org /en/news/press-release/2016/12/12/new-data-reveals-uptick-in-global-gas-flaring (Dec12, 2016).

3 Huang K., Fu J.S. A global gas flaring black carbon emission rate dataset from 1994 to 2012. *Sci Data*. 2016. Vol. 3, 160104 [electronic resource].

4 Vorob'ev A., Shchesnyak E. Associated Petroleum Gas Flaring:The Problem and Possible Solution. *Proc. of the "14th International Congress for Applied Mineralogy - ICAM"*, 2019, pp 227–230.

5 Rodin L. Compact Methanol Production at Oil and Gas Fields. Nowadays and development perspective. *Proceeding of the "VII International Oil and Gas Conference".* NewFolk O&G CC. Lviv, Ukraine. 2021, pp.72.

6 Melnikov E.J. ed. *Azotchik Handbook. Moscow* Chemistry, 1986, 54 p. [in Russian]

7 Nestle F., et.al. Kinetic modelling of methanol synthesis over commercial catalysts: A critical assessment. *Chem. Eng .J*. 2020. Vol. 394, pp. 1 – 13.

8 ANSYS FLUENT 12.0 *Theory Guide, Release 12.0 © ANSYS*, Inc. 2009-01-23. Available at: www.afs. enea.it/project/neptunius/docs/fluent/html/th/main_pre.htm.

9 Smith G.P., Golden D.M., Frenklach M., et al. GRIMech 3.0. Available at: http://combustion.berke ley.edu/gri-mech/version30/text30.html.

10 Magnussen B.F. On the Structure of Turbulence and a Generalized Eddy Dissipation Concept for Chemical Reaction in Turbulent Flow. *Proceeding of the "19th AIAA Aerospace Science Meeting"*. St.Louis, Missouri, USA. 1981, pp.1 – 6.

11 Magnussen B.F. Modeling of NOx and soot formation by the Eddy Dissipation Concept. Int.Flame Research Foundation. *Proceedings of "11th Task Leaders Meeting, IEA Working Party on Energy Conservation in Combustion"*, Örenäs, Glumslöv, Sweden, 1989. pp. 248 – 268.

12 Wang Y., Zeng H., Banerjee A., et al. Elementary reaction modeling and experimental characterization on methane partial oxidation within a catalyst-enhanced porous media combustor. *Energy & Fuels*. 2016. Vol.30 (9), pp. 7778 – 7785. doi:10.1021/acs.energyfuels.6b01624

13 Voloshchuk Y., Vascellari M., Hasse Ch., et al. Numerical study of natural gas reforming by non-catalytic partial oxidation based on the Virtuhcon Benchmark. *Chemical Engineering Journal*. 2017. Vol.327, pp. 307 – 319. doi:10.1016/j.cej.2017.06.061.

14 Yunus A. Çengel, Afshin J. Ghajar. *Heat and Mass Transfer: Fundamentals & Applications*. 5th edition. McGraw-Hill Education. 2015, 992 p.

15 *The Future of Petrochemicals Towards more sustainable plastics and fertilisers*. OECD/IEA, 2018. A*vailable at:* www.iea.org

16 Lu X., Wang T. Simulation of ash deposition behavior in an entrained flow coal gasifier. *International Journal of Clean Coal and Energy*. 2015. Vol.4, pp. 43 – 59.

PHOTOVOLTAIC PROPERTIES OF FUNCTIONALIZED INDODICARBOCYANINE DYE

Ibrayev N.Kh.[1*], Seliverstova E.V.[1], Omarova G.S.[1], Ishchenko A.A.[2],
Derevyanko N.A.[2], Khamza T.[3]

[1*]Institute of Molecular Nanophotonics, Buketov Karaganda University, Karaganda, Kazakhstan, niazibrayev@mail.ru
[2]Institute of Organic Chemistry, NAS of Ukraine, Kyiv, Ukraine
[3]Nazarbayev Intellectual School of Karaganda, Kazakhstan

The effect of the chemical structure of polymethine dyes on their spectral-luminescent and photovoltaic properties has been studied. It has been shown that the introduction of hydroxyl functional groups into the dye structure leads to a bathochromic shift of the absorption and fluorescence bands. During the adsorption of dyes on the surface of titanium dioxide, a shift of their spectra to the red wavelength region was recorded with a simultaneous broadening of the bands caused by dye aggregation on the semiconductor surface. A decrease in the lifetimes of the excited state of molecules by 64 and 30% was registered for dyes 1 and 2, respectively. Quenching of the fluorescence lifetimes of adsorbed molecules is the result of electron transfer from the dye to the semiconductor. Measurements of the photovoltaic parameters of the studied dye-sensitized solar cells showed a higher efficiency for the functionalized dye, which is associated with better adsorption of this compound on TiO_2.

Keywords: polymethine dyes; functional groups; optical properties; photovoltaics; dye-sensitized solar cells.

Introduction

Currently, the search and active using of new alternative energy sources in many developed countries of the world are accepted as vital, strategically necessary resources. In this regard, active development of photovoltaic cells is carrying out. Solar cells with using of organic dyes, despite their low efficiency, are a good alternative to semiconductor solar panels, since their production is more environmentally friendly and does not require complex technology. The main component of a dye-sensitized solar cell (DSSC) is a semiconductor electrode with adsorbed dye molecules. The most popular and chemically stable sensitizers for DSSC are organometallic chromophores and complexes with rare earth elements [1, 2]. However, their synthesis is a laborious and rather expensive task. In this regard, many groups are developing organic molecules-sensitizers for DSSC.

The aim of the present work is studying if the effect of functional groups in the structure of a polymethine dye on its spectral-luminescent and photovoltaic properties. The choice of these dyes is due to the fact that among organic chromophores they have the largest range of changes in photophysical [3] and nonlinear optical properties, due to which they are widely used in organic photovoltaics [3–6], laser technology [7–10], and nonlinear optics [11-13], information technologies [14, 15], in biology and medicine [16, 17]. Among the important properties of polymethine dyes, their extremely high extinction coefficients having to be highlighted [3]. In this regard, polymethine dyes are a promising class of sensitizers for solar cells. To date, it has been shown that the adsorption of polymethine dyes on TiO_2 leads to an expansion of the efficiency of light harvesting of the cell's working electrode to the red region of the spectrum [18–23]. This increases the conversion efficiency of light into electrical energy. A factor contributing to an increase in the adsorption efficiency of polymethine dyes on the surface of a semiconductor is the "anchor" groups in the structure of the dye.

1. Experiment

Cationic indodicarbocyanine dyes (IPD) were chosen as the objects of study, the structural formulas of which are shown in Fig. 1. IPD 1 with hydroxyl groups is an analog of IPD 2 dye. The main spectral-luminescent and photovoltaic properties of IPD dye are detailed in [5, 24].

The absorption and fluorescence spectra of the dyes were measured on a Cary-300 and Eclipse spectrometer (Agilent Techn.). The lifetimes of the excited state of the dye molecules were measured with using of a pulsed spectrofluorimeter with picosecond resolution and recording in the time-correlated photon counting mode (Becker&Hickl, Germany) [25, 26].
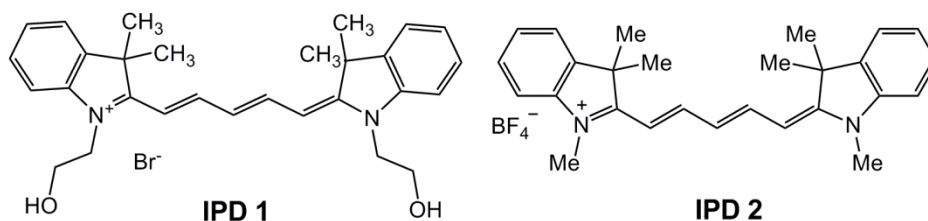
Fig. 1. Structure of IPD 1 and 2

Glass plates coated with FTO (surface resistivity ~7 Ω/sq, Sigma Aldrich) were used to prepare and assemble solar cells. A nanometer blocking layer of TiO_2 was deposited on the FTO surface. Pastes from TiO_2 nanoparticles (Sigma-Aldrich, d~21 nm) were prepared according to the procedures of [4–6, 27]. TiO_2 pastes were deposited onto the surface of a conductive glass by the doctor-blading method. The films were left to relax in air for 3 minutes, dried at 125 ºC for 6 minutes, and annealed stepwise (with a step of 175 ºC) in the temperature range from 175 to 500 ºC.

Ethanol solutions with dye concentration equal to 10^{-4} mol/L were used for the sorption. For this purpose, porous semiconductor films were placed into dye solution for the 24 h. After that, the films were dried in an oven (T=70°C) for 30 minutes. The sorption of the dye into the pores and the estimation of its concentration were controlled by the methods of absorption spectroscopy. The platinum electrodes were prepared separately on the FTO surface. Platinum was deposited with electrochemical method from an ethanol solution of H_2PtCl_6 (Sigma Aldrcih). At the final stage, the cells were assembled according to the standard procedure [27].

The current-voltage characteristics (CVC) of solar cells were measured under illumination by Xe lamp with a light power of 100 mW/cm^2 on a CT50AAA Cell Tester measuring complex (Photo Emission Tech.). The measurements were carried out in the photovoltaic mode at room temperature. The parameters of the DSSC as the open circuit voltage (V_{oc}), the short circuit current density (J_{sc}), the fill factor (FF), and the efficiency (η) of the cell were determined from the CVCs.

2. Results and discussion

The absorption and fluorescence spectra of IPD 1 dye measured in ethanol solution are shown in the Fig. 2a. The absorption bands of IPD 1 and 2 are located in the wavelength range of 500–700 nm. The absorption spectrum maximum of the IPD 1 dye exhibits at 645 nm (Table 1) with a shoulder at ~600 nm. For the parent dye IPD2, the band maximum is hypsochromically shifted by 10 nm and exhibits at 635 nm with a shoulder at $^a\lambda_{2\,max}$=595 nm. At the same time, it should be noted that the extinction coefficient of IPD 1 dye have the close values as for IPD 2 dye [5].

Table 1. Spectral and luminescent properties of IPD 1 and 2 in ethanol solutions (C=10^{-5} mol/L)

Dye	$^a\lambda_{1\,max}$ (nm)	$^a\lambda_{2\,max}$ (nm)	$\Delta^a\lambda_{1/2}$ (nm)	$^f\lambda_{1max}$ (nm)	$^f\lambda_{2max}$ (nm)	$\Delta\lambda^f_{1/2}$ (nm)
IPD 1	645	600	45	670	720	35
IPD 2	635	595	45	655	715	31

Photoexcitation of the emission spectra of dye solutions was carried out both from the short-wavelength (λ_{exc}=590 nm) and long-wavelength side (λ_{exc}=630 nm) of the absorption spectrum of luminophores. The highest dye fluorescence intensity was recorded upon excitation at 630 nm. As in the absorption spectra, the short-wavelength shoulder in the region of 715 – 720 nm is mirrored in the fluorescence spectra. The maximum of the fluorescence spectrum of the dyes IPD 1 and IPD 2 was registered at 670 and 655 nm, respectively. Thus, it has been established that functional groups have practically no effect on the spectral and luminescent characteristics of the IPD 1 dye. However, they play an important role in the adsorption of dyes on semiconductor films.
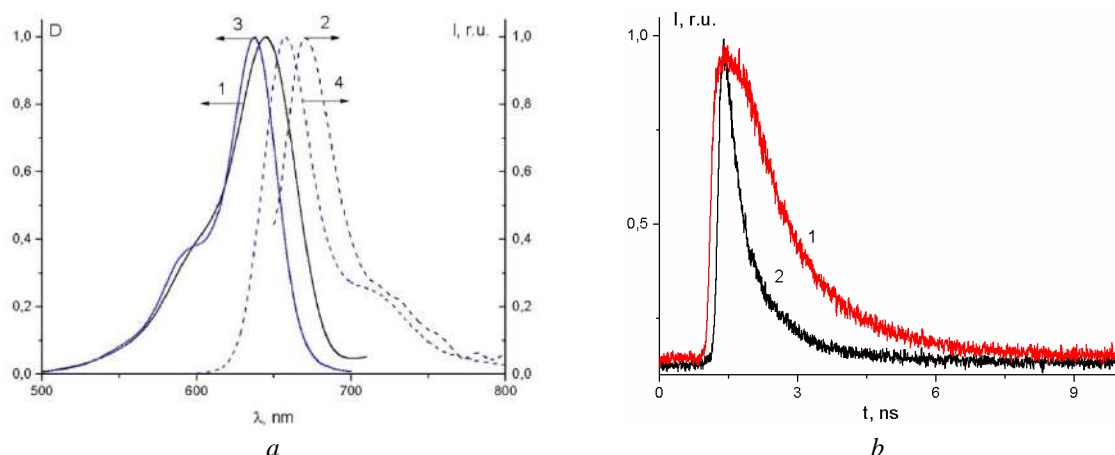
Fig.2. (a) Absorption (1, 3) and fluorescence (2, 4) spectra of dyes 1 (1, 2) and 2 (3, 4) in ethanol (C=10^{-5} mol/L); (b) fluorescence decay kinetics of dye 1 in ethanol solution (1) and on TiO_2 film (2), λ_{exc}=488 nm

Since the sensitization of the active electrodes of the Grätzel cells occurs by the adsorption of dyes from solutions, it was interesting to find out what spectral changes would occur in the absorption and fluorescence spectra of the dyes on the surface semiconductor films.

For this purpose, TiO_2 films were prepared on nonluminescent quartz substrates by the doctor-blading method. The measurements showed (Table 2) that a bathochromic shift of the absorption and fluorescence bands of both dyes occurs on the surface of the porous films. At the same time, the absorption and fluorescence band of the dyes were deformed, which is expressed in the broadening of the spectra, as well as the virtual absence of a shoulder in both the absorption and fluorescence spectra of the dye.

Table 2. Spectral-luminescent parameters of IPD 1 and 2 adsorbed on the surface of TiO_2 films

Dye	$^a\lambda_{1\ max}$ (nm)	$\Delta^a\lambda_{1/2}$ (nm)	$^f\lambda_{1max}$(nm)	$\Delta\lambda^f_{1/2}$ (nm)	τ_f (ns)	$\tau_f/\tau_f^{solution}$
IPD 1	648	128	672	132	0.40	0.36
IPD 2	646	125	663	130	0.65	0.70

Measurements of the fluorescence decay kinetics of dyes on TiO_2 films have shown that the lifetime of the excited state of the dye was reduced by 64 and 30% for IPD 1 and 2, respectively (Fig. 2b). The quenching of the fluorescence lifetime of adsorbed dyes is the result of the electron transfer from the dye to semiconductor when colored films were irradiated with visible light [22, 25]. This effect is more pronounced for IPD 1.

The higher efficiency of electron transfer was confirmed by data on the photovoltaic characteristics of solar cells, sensitized with dye 1 or 2 (Table 3).

Table 3. Photovoltaic parameters of DSSC, sensitized with IPD 1 and 2

Dye	J_{sc} (mA/cm^2)	V_{oc}(mV)	FF	η(%)
IPD 1	0.46	272.0	0.30	0.037
IPD 2	0.11	375.0	0.15	0.006

It can be seen that the cell with the IPD 1 has better photovoltaic parameters compared to the IPD 2, despite the fact that the open-circuit voltage Voc for the IPD 2 is higher. This can be explained by the fact that the presence of functional groups in the IPD 1 dye molecule leads to an almost 4-fold increase in the J_{sc} value compared to IPD 2. This parameter directly depends on the number of charge carriers transferred from the dye to the semiconductor [28, 29]. That is, the process of charge-carriers generation in the cell is more efficient due to the presence of anchor groups in the structure of the dye 1. In addition, this assumption was confirmed by the change in the optical density of dye solutions before and after their adsorption on the surface of the TiO_2 films. As the estimation of the number of adsorbed molecules (N) on the cell surface showed, N=$2.5 \cdot 10^{16}$ for IPD 1 and N=$1.7 \cdot 10^{16}$ for IPD 2.

Conclusion

Thus, the measurements showed that the introduction of functional groups into the structure of the indodicarbocyanine dye molecule leads to a bathochromic shift of its absorption and fluorescence bands. During the adsorption of the studied dyes, a shift of their spectra towards red wavelengths was recorded. At the same time, the absorption and fluorescence bands of the dyes were broaded, as well as the shoulder in both the absorption and fluorescence bands of the dye the virtual was absent. This is accompanied by a decrease in the lifetime of the excited state of the dye by 64 and 30% for IPD 1 and 2, correspondingly. The quenching of the fluorescence lifetimes of adsorbed dyes is the result of electron transfer from the lower unoccupied molecular orbital of the dye to the conduction band of the semiconductor upon irradiation of the films with visible light. On the basis of the photovoltaic parameters, it can be concluded that the presence of functional groups in the dye molecule leads to an increase in the efficiency of the photovoltaic characteristics of solar cells sensitized with organic dyes.

REFERENCES

1   Sharma K., Sharma V., Sharma S.S. Dye-sensitized solar cells: fundamentals and current status. *Nanoscale Research Letters*. 2018. Vol. 13, pp.381(1-6).

2   Freitag M., Teuscher J., Saygili Y., et al. Dye-sensitized solar cells for efficient power generation under ambient lighting. *Nature Photon.* 2017. Vol. 11, pp. 372–378.

3   Ishchenko A. A. Structure and spectral-luminescent properties of polymethine dyes. *Russian Chemical Reviews.* 1991. Vol. 60, No. 8, pp. 865–884.

4   Ibrayev N. Kh., Seliverstova E. V., Ishchenko A. A., et al. The effect of sulfonate groups on spectral-luminescent and photovoltaic properties of squarylium dyes. *Journal of Photochemistry and Photobiology A*: *Chemistry.* 2017. Vol. 306, pp. 570-575.

5   Ibrayev N., Omarova G., Seliverstova E., et al. Plasmonic effect of Ag nanoparticles on polymethine dyes sensitized titanium dioxide. *Engineered Science.* 2021.Vol. 14, pp. 69–77.

6   Ibrayev N., Seliverstova E., Omarova G., et al. Sensitization of TiO$_2$ by merocyanine dye in the presence of plasmon nanoparticles. *Materials Today: Proceedings.* 2022. Vol. 49, pp. 2464-2468.

7   Ibrayev N.Kh., Ishchenko A.A., Afanasyev D.A., Zhumabay N. D. Active laser medium for near-infrared spectral range based on electron-unsymmetrical polymethine dye and silver nanoparticles. *Applied Physics B: Lasers and Optics.* 2019. Vol. 125, pp. 1-7.

8   Ibrayev N., Afanasyev D., Ishchenko A., et al. Influence of silver nanoparticles on the spectral-luminescent and lasing properties of merocyanine dyes solutions. *Laser Physics Letters.* 2021. Vol. 18, No. 8, pp. 085001(1-6).

9   Bulavko G. V., Ishchenko A.A. Organic bulk heterojunction photovoltaic structures: design, morphology and properties. *Russian Chemical Reviews,* 2014, Vol. 83, No. 7, pp. 575–599.

10   Ishchenko A.A. Laser media based on polymethine dyes. *Quantum Electronics.* 1994. Vol. 24, No. 6, pp. 471-492.

11   Bezrodnyi V. I., Ishchenko A.A. High-energy single pulse and multispike operation with a passive polymer Q-switch. *Optics and Laser Technology*. 2002. Vol. 34, No. 1, pp.7-13.

12   Klimusheva G., Bugaychuk S., Garbovskiy Yu., et al.Fast dynamic holographic recording based on conductive ionic metal-alkanoate liquid crystals and smectic glasses. *Optics Letters.* 2006. Vol. 31, No. 2, pp. 235-237.

13   Bondarev S. L., Tikhomirov S. A., Knyukshto V. N., et al. Fluorescence and solvatochromism of a merocyanine dye with a high quadratic polarizability in solutions and polymer films. *Journal of Luminescence.* 2007. Vol. 124, No. 1, pp. 178-186.

14   Voiciuk V., Redeckas K., Derevyanko N. A., et al. Study of photophysical properties of a series of polymethine dyes by femtosecond laser photolysis. *Dyes and Pigments*. 2014. Vol. 109, pp. 120-126.

15   Davidenko N.A., Ishchenko A.A. Spin conversion and electric field effect on photoluminescence in amorphous molecular semiconductors doped with ionic dyes. *Chemical Physics.* 1999. Vol. 247, pp. 237-243.

16   Ciubini B., Visentin S., Serpe L., et al. Design and synthesis of symmetrical pentamethine cyanine dyes as NIR photosensitizers for PDT. *Dyes and Pigments*. 2019. Vol. 160, pp. 806-813.

17   Dereje D.M., Pontremoli C., Moran Plata M.J., et al. Polymethine dyes for PDT: recent advances and perspectives to drive future applications. *Photochemical&Photobiological Sciences.* 2022. Vol. 21, pp. 397-419.

18 Winstead A., Williams R. *Application of microwave assisted organic synthesis to the development of near-IR cyanine dye probes*. In *Environmental Biosensors*. Somerset V. (Ed.), InTech, 2010, pp. 237-254.

19 Ma X., Hua J., Wu W., et al.A high-efficiency cyanine dye for dye-sensitized solar cells. *Tetrahedron*. 2008. Vol. 64, pp. 345-350.

20 Funabiki K., Mase H., Saito Ya., et al. Design of NIR-absorbing simple asymmetric squaraine dyes carrying indoline moieties for use in dye-sensitized solar cells with Pt-free electrodes. *Organic Letters*. 2012. Vol. 14, pp.1246-1249.

21 Ghann W., Kang H., Emerson E., et al. Photophysical properties of near-IR cyanine dyes and their application as photosensitizers in dye sensitized solar cells. *Inorganica Chimica Acta*. 2017. Vol. 467, pp. 123-131.

22 Mishra A., Markus M., Fischer K. R., et al. Metal-free organic dyes for dye-sensitized solar cells: from structure: property relationships to design rules. *Angewandte Chemie International Edition*. 2009. Vol. 48, pp. 247-249.

23 Naim W., Novelli V., Nikolinakos I., et al. Transparent and colorless dye-sensitized solar cells exceeding 75% average visible transmittance. *JACS Au*. 2021. Vol. 1, No. 4, pp. 409-426.

24 Seliverstova E., Ibrayev N., Omarova G., et al. Competitive influence of the plasmon effect and energy transfer between chromophores and Ag nanoparticles on the fluorescent properties of indopolycarbocyanine dyes. *Journal of Luminescence*. 2021. Vol. 235, pp. 118000.

25 Ibrayev N. Kh., Dzhanabekova R. Kh., Amanzholova G. S. Spectral and luminescent properties of carbon quantum dots functionalized with N- and S-contaning groups. *Eurasian phys. tech. j.* 2021. Vol. 18, No. 2, pp. 12-17.

26 Zhumabekov A. Zh., Ibrayev N. Kh., Seliverstova E.V. Investigation of photocatalytic activity of TiO_2–GO nanocomposite. *Eurasian phys. tech. j.* 2019. Vol. 16, No. 1, pp. 42-46.

27 Ito S., Murakami T.N., Comte P., et al. Fabrication of thin film dye sensitized solar cells with solar to electric power conversion efficiency over 10%. *Thin Solid Films*.2008. Vol. 516, pp. 4613-4619.

28 Kathiravan A., Renganathan R. Effect of anchoring group on the photosensitization of colloidal TiO_2 nanoparticles with porphyrins. *Journal of Colloid and Interface Science*. 2009. Vol. 331, No. 2, pp. 401-407.

29 Huber R., Sporlein S., Moser J. E., et al. The role of surface in the ultrafast photoinduced electrone transfer from sentisized dye molecules to semiconductor colloids. *Journal of Physical Chemistry B*. 2000. Vol. 104, pp. 8995-9003.

RESULTS OF THE EXPERIMENTAL STUDY OF THE FLOW FIELD OF A STATIONARY AIR FLOW DURING THE OPERATION OF A FOUR-BLADE BIDARRIEUS-1 TURBINE

Yershina A.K.[1], Manatbayev R.K.[2], Baizhuma Zh.[2]

[1]Department of Physics, Kazakh National Women's Pedagogical University, Almaty, Kazakhstan
[2]Department of Thermophysics and Technical Physics, al-Farabi Kazakh National University, Almaty, Kazakhstan,
rustemmanatbayev@gmail.com

There are a great variety of wind turbine constructions but by their principle of operation they are divided into three main types - sail (Savonius wind power unit), propeller and airfoils (Darrieus wind turbine). At present, propeller-type wind-turbines are the most widely spread. They are produced on a commercial level in many countries. Other conditions being equal, the power produced by wind power unit (WPU) is proportional to the area being swept around by a wind wheel. Therefore, Megawatt propeller-type wind turbines have blades with the length of 40 and more meters. Only aircraft works with a highly-qualified personnel and corresponding equipment can produce such long blades of a specific shape. Of high interest have become airfoil wind turbines (Darrieus WPU) lately. They are of a simpler construction and have a quite high wind power utilization factor ($\xi=0.45$). In spite of the fact that this is a good index of WPU efficiency, the workers of al-Farabi Kazakh National University have developed a new version of a wind turbine which allows increasing 1.3-1.6 times the value of this coefficient. This apparatus is named a Bidarrieus unit. This paper presents the description of a Bidarrieus unit, the principle of its operation and the possibility of increasing the wind power utilization factor. Also, the results of testing an acting laboratory model in an aerodynamic tunnel

Keywords: wind turbine, Darrieus, Bidarrieus, two-rotor wind power turbine, wind power factor

Introduction

Recently, interest has appeared in wing-type wind turbines, called the Darrieus wind turbine, invented by the French engineer Darrieus in 1925. [1] The Darrieus apparatus has the following advantages over other wind turbines:

1) due to the vertical-axial rotation of the turbine, the change in wind direction does not play a role;

2) the swept area is not inferior to the propeller area;

3) the power generator and other equipment are located at ground level, which facilitates the construction of the large-capacity machine, maintenance, and repair;

4) structurally, they are relatively simple to manufacture and have a fairly high coefficient of wind energy utilization (x=0.45);

5) the relative noiselessness of the turbine rotation, due to the continuous flow around the working blades by the wind flow, since symmetrical NACA profiles are used here;

6) the Darrieus wind turbine allows a wide range of design versions of these devices.

Therefore, many firms are showing interest in vertical-axis wind turbines of the carousel type, in particular, the Darrieus turbine [1-4]. As it is known, the Darrieus construction has a single shaft of rotation and a rectilinear span associated with two oppositely located working blades. A distinctive feature of the proposed device is the use of the principle of autonomous operation of two coaxial shafts connected to the turbine and transmitting wind energy to two current generators. Thus, the power removed by the two direct current generators is summed up. For centering, the coaxially mounted rotation shafts are separated from each other by support bearings, which ensures their independent rotation: both coordinated in the same direction and in the opposite direction. The wingspan and rotor blades can be made in the form of NACA symmetrical airfoils. The rotation of the wind turbine occurs due to the action of lifting forces on the working blades. The working blade can be connected to the rotation shaft using a swing or troposkino method.

1. The main part. The principle of operation of vertical-axis wind power devices of the carousel type.

Currently, propeller-type wind turbines are widely used, which make it possible to increase the installed capacity of each installation to several megawatts. Like any mechanical apparatus, a wind turbine of this type has both positive and negative sides. The positive is the developed and mastered long-term technology, on the basis of which, at present, high-performance power plants are being created around the world. Nevertheless, while bringing significant benefits to the country's energy balance, they cause some damage to the environmental situation in these regions. For example, propeller wind farms produce significant disturbances due to the high level of turbulence in the atmosphere. The high and wide range of sound waves create unbearable conditions for surrounding living organisms. The higher the installed capacity of such wind farms, the larger the lifeless territory in these regions (birds, wildlife and local people leave these places). In this regard, Darrieus carousel-type wind turbines, operating on the lifting force of the working blades and having a NACA symmetrical wing shape, are becoming more preferable. At the same time, the overall dimensions of such devices are much smaller than propeller ones, with almost the same installed power values. The material consumption and the space occupied for these devices are incomparable with the propeller ones. The Darrieus wind turbine has a non-separated flow around the blade and, accordingly, is almost silent. These profiles (NACA-0021) have low drag at $\varphi=0$. [5,6]

$$\varsigma_{x\pi} = C_{x\pi}\rho\frac{U^2}{2}, \qquad \text{where } C_{x\pi}=0.028.$$

Whereas, if the blade of the same profile is deployed, with the trailing edge towards the wind flow, the resistance becomes an order of magnitude higher, due to the separation flow.

$$\varsigma_{xк} = C_{xк}\rho\frac{U^2}{2}, \qquad \text{where } C_{xк}=0.16.$$

In this regard, many companies give more and more preference to carousel-type devices. In addition, they allow the possibility of developing and creating various promising versions of wind turbines. At present, the theoretical foundations of Darrieus wind turbines have been developed [5,7].

A group of Kazakhstani scientists-enthusiasts for several years has been actively engaged in the development and modeling of various versions of carousel-type wind turbines with high utilization rates of wind energy at the Research Institute of Mathematics and Mechanics. New versions of the wind turbine have been developed, which allow, with the same swept area, to remove wind energy by 30-40% more compared to other wind turbines. Patents were received for several inventions [8,9]: wind turbine Bidarie-1, vertical-axial composite wind turbine HBI-rotor, wind turbine Bidarie-2, and organization of thermal protection of wind turbine operation under adverse climatic conditions. Schematic diagrams and photographs of the designs of the developed wind turbines are shown in fig. 1, 2.

The objective of the study is to develop a new modification of a carousel-type wind turbine with high technical and economic indicators. The mission of this study is to create a wind turbine at minimal cost and get the maximum of wind energy, which is in abundance in any region of our republic. A two-rotor wind turbine design is proposed, which allows to remove the maximum amount of wind energy. This design ensures the removal of the main element - the wind turbine, beyond the surface boundary layer and thereby allows you to remove wind energy in the area of potential wind movement, where the average wind speed is 2-3 times higher than the average wind speed of the surface boundary layer. This will allow the unit to begin to rotate spontaneously already at a wind speed of 5 m/s.

2. Features and principles of operation of Bidarrieus-1 wind turbines

The first version of two-rotor machines, called Bidarrieus-1, is quite widely known not only in Kazakhstan, but also abroad. The design of this wind turbine is a set of two Darrieus turbines as if nested in each other and deployed so that their spans are perpendicular to each other, i.e. $\alpha = 90°$ [7-9]. Figure 1 shows various design schemes for the Bidarrieus-1 wind turbines. On the diagrams of Fig. 1, the following designations are accepted: 1 - blades, 2 - swings, 3 - housing, 4 - rotation shafts, 5 - bearing, $\alpha= 90^0$. In fig. 1a shows a variant with straight working blades (1) of an H-shaped rotor.
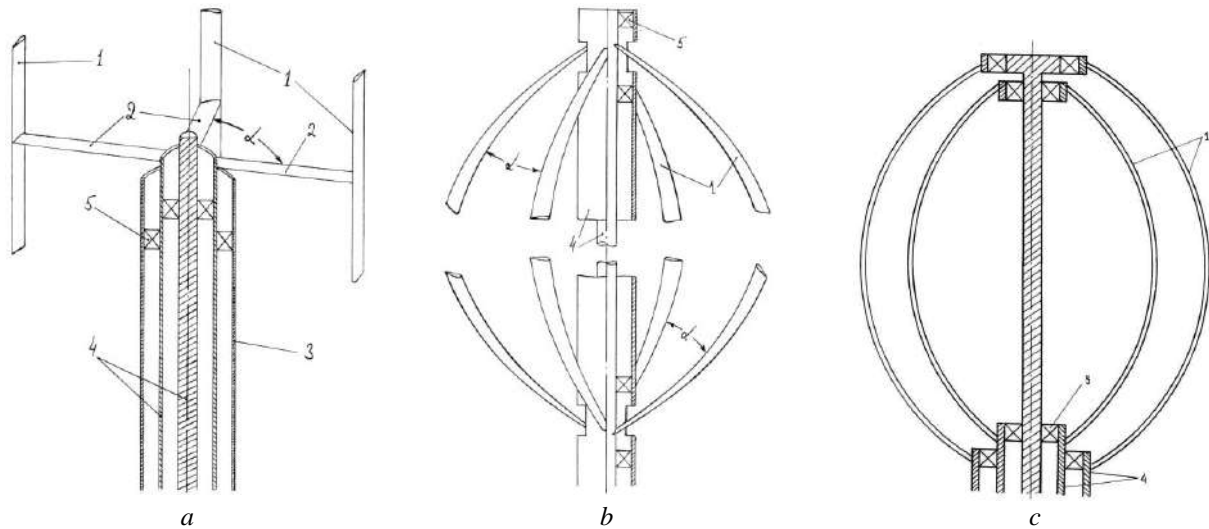
Fig 1. Schematic diagrams of the design of various wind turbines Bidarrieus -1:
a) with straight wings (one-way rotation); b) troposkino systems (one-way rotation); c) with troposkino blades
(shaft rotation in different directions)

Each of the two coaxially located shafts (4) is connected with its symmetrically located pair of blades (1) by means of spans (2), which, during rotation, create a moment of forces that autonomously act on the "own" shaft. Figure 1b shows a diagram of the wind turbine Bidarie-1, but the blades are made in the form of a troposkino. The stability of the wind turbine is achieved by the symmetrical arrangement of the blades. Fig.1c describes the design that allows the rotation of the shafts in different directions. In this embodiment, both shafts must rotate in the same direction with the same angular velocity. There is a special corrective device (clamp) that maintains the angle between the spans $\alpha = 90°$ when Bidarrieus-1 is operating [8].

3. The laboratory model of Bidarrieus-1

In the course of research, for testing in a wind tunnel, an operating laboratory model of the Bidarrieus -1 wind turbine was initially made (Fig. 2). The dimensions of the model are chosen so that it fits freely in the working section of the wind tunnel. Each pair of blades is connected by mutually perpendicular spans so that each of the four blades of the Darrieus wind turbine model is located at an angle of 90° to each other, Fig. 1a. The working section of the wind tunnel has an elliptical shape, the major axis of which is located horizontally.

Fig. 2. Laboratory model of the Bidarrieus -1 twin-rotor wind turbine of JSC Research Institute "Gidropribor", Uralsk: side view.

The current model has the following dimensions: total height 785 mm; the span on which four working blades are located is 800 mm. The working blades and both spans were made in the form of a symmetrical NACA-0021 profile. The blades and spans have the same chords, 32 mm long, the length of the working blades is 550 mm, the length of the spans is 400 mm. The proposed device is placed in one housing and consists of two coaxially located shafts of rotation connected with the working blades using spans. A distinctive feature of the Bidarrieus-1 device is the use in the design of the principle of autonomous operation of the shafts connected to the wind turbine and transmitting wind energy to two electric generators. When conducting experiments to determine and compare the values of wind energy utilization factors, the model worked both in the Darrieus mode and in the Bidarrieus-1 mode. The test results at various air flow rates showed the efficiency of the Bidarrieus-1 twin-rotor machine.

4. The methodology of the experiment and the results of the experimental study

The experiments were carried out on a working laboratory model of a wind turbine with straight working blades in a wind tunnel of JSC Research Institute "Gidropribor". The flow characteristics were measured in the working section of the wind tunnel. The model is a two-bladed version with vertical straight working blades mounted on horizontally directed strokes, rotated by 180°. The working blades and swings are symmetrical NACA-0021 profiles. Two such two-bladed wind turbines are mounted on two coaxial shafts that can rotate independently of each other. The dimensions of the wind turbines are identical and the four working blades are located at the same distance from the common axis of rotation, in other words, the length of the strokes is the same. Strokes are attached to the top of the shafts. Each of the coaxial shafts below has a pulley, with the help of a belt drive, two independently operating electric generators rotate. Wind turbines are rotated relative to each other by 90°, so that the turbine strokes are a cross with right angles. For independent rotation of the turbines, there is a special device that maintains this angle constant. Thus, each turbine rotates its own shaft and transmits torque to one of the electric generators. Such a device is the Bidarrieus-1 model, capable of simultaneously rotating 2 electric generators.

The design allows you to remove one of the turbines connected to the inner shaft. In this case, we will have the well-known two-bladed Darrieus turbine model, which, through the rotation of the shaft, transfers energy to one electric generator. As a result, it is possible to compare the power developed by the wind turbines "Bidarrieus-1" (the total capacity of two electric generators) and "Darrieus" under all other identical conditions. The dimensions of the wind turbine are chosen so that the model fits completely in the working section of the wind tunnel. This is an open area of elliptical shape with dimensions: length - 2.2 m, the major axis of the ellipse - 2.1 m is located in the horizontal direction, and the minor axis - 1.2 m. The airflow in the working area moves in a horizontal direction at a speed of up to 35m/s (Fig.3).
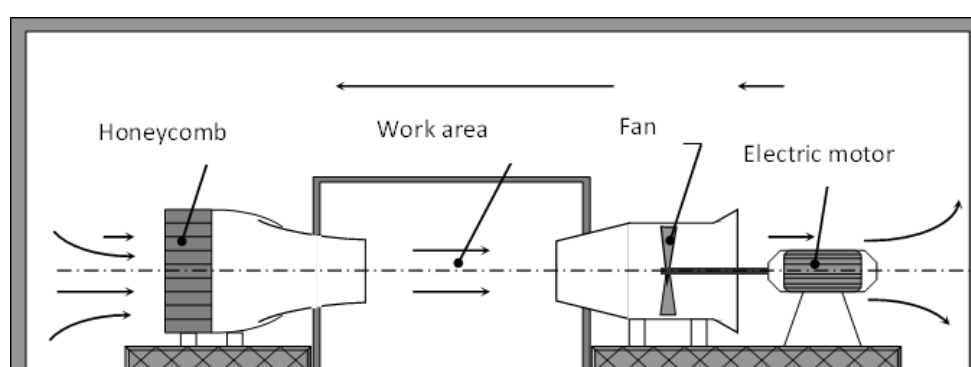
Fig.3. Schematic diagram of a wind tunnel.

The model was mounted in the central part of the working section of the wind tunnel across the flow so that the plane of rotation of the flywheels lay in the central plane of the working section passing through the major axis of the ellipse, and the axis of rotation of the turbine was directed along the minor axis of the ellipse. Model dimensions: height from the pulleys to the plane of rotation of the flaps - 0.51 m, length of the flaps from the turbine axis to the chord of the working wings, equal to the radius of rotation - 0.404 m, length of the working blade (T - shaped mount) - 0.55 m, chord profile of the working blades and shoulders - 0.03m (NACA-0021 profile).
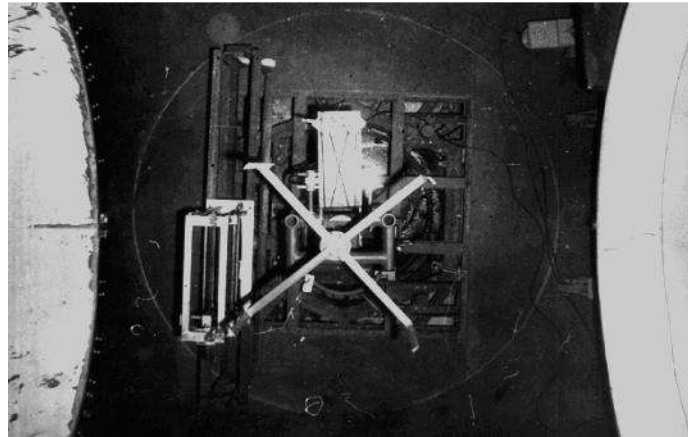
Fig.4. Operating laboratory of the Bidarrieus -1turbine model in the wind tunnel working section (top view).

The possibility of quantitative recording of the power developed by the turbine made it possible to carry out four series of experiments. We were interested in the repeatability of the results obtained, as well as the expansion of the experimental data with the variation of various elements of the electrical part. In each series of experiments, measurements were made with the rearrangement of electric generators, connecting them with a belt drive to one or another shaft. Similarly, the rheostats were interchanged during power removal, and the current and EMF measurements were carried out either with one device or with another. The data obtained are summarized in Table 1. The last column of the table (the rightmost column) shows the power received in the "darier" mode, and the total power of the two electric generators when the turbine is operating in the " Bidarrieus-1 " mode. As can be seen from the table, in all experiments, the total power of the " Bidarrieus-1 " was 30-40% higher than that of the "Darrieus".

At the end of the power tests, an aerodynamic experiment was carried out using a three-channel probe to analyze the distribution of the velocity and pressure field in front of the turbine, inside the cylindrical surface swept by the rotor blades, and also behind, behind the wind turbine.

Research was planned to measure the magnitude of the speed, as well as the distribution of pressure in front of and behind the wind turbine. In addition, measurements were taken inside a cylindrical cavity described by rotating working blades (sweeping surface). All measurements were carried out in the horizontal plane of rotation of the swings. Thus, the influence of the end effects of the working blades, which were sufficiently removed from the measurement plane, was excluded.

This made it possible to use a three-channel Pitot-Prandtl nozzle. The speed of the air flow in the working section of the wind tunnel was controlled by a conventional full-pressure tube. Since the working section of the wind tunnel was under rarefaction, the value of the latter was measured in each operating mode of the wind tunnel. In order to improve the accuracy of measurements, the main studies were carried out at a flow velocity in the working section of the wind tunnel equal to 17 m/s. In this case, the angular velocity of rotation of the turbine was 43.96 rad/s (n = 420 rpm). The measurement accuracy with a three-channel probe using a cup micromanometer was 1 mm of water. The limb of the three-channel probe, equipped with a vernier, made it possible to measure the angle of rotation of the measuring probe with an accuracy of $\sim 0.1^0$. The measuring probe was mounted on a coordinator, with the help of which it was possible to move in the horizontal direction with an accuracy of 0.1 mm. The coordinate was located below the cylindrical surface described by the rotating working blades of the turbine. The holder of the three-channel measuring probe was fixed vertically, parallel to the side surface of the swept cylindrical body so that the receiving openings of the measuring probe were directed towards the air flow and located in the plane of rotation of the swings. When measuring inside the swept cylindrical body, the receiving holes were located 50 mm below the swings.

The obtained experimental data were processed in dimensionless quantities:

$$\bar{P} = \frac{P_{cm} + P_\infty}{P_\infty}, \quad \bar{V} = \frac{V}{V_\infty}, \quad \bar{r} = \frac{r}{R}$$

where P_{str} is the static pressure according to the readings of the three-channel probe, P_∞ is the pressure in the working chamber, ρ is the air density determined from barometric readings, V_∞ is the air velocity in the working area when the Darrieus model is stationary, R is the radius of the swept cylindrical surface.

Table 1. The results of tests of wind turbines "Darrieus" and "Bidarrieus-1"

Expe-rience num-ber	MODE		No-load		Work with load				
			RPM	Genera-tor emf, V	RPM	Voltage of generator, V	Amperage, mA	Total power,W	Power, W
I-series of experiments									
1.	2-bladed "Darrieus"	(1 engine)	800		450	3	130	0.39	0.39
2.	«Bidarrieus»	(1 engine)	700		400	2.5	110	0.275	0.55
		(2 engine)	700		400	2.5	110	0.275	
II-series of experiments									
1.	2-bladed "Darrieus" rheostats 2.1	(1 engine)	500	5	450	3	100	0.3	0.3
2.	«Bidarrieus-1» rheostats 2,1	(1 engine)	400	3,8	350	2,2	95	0.21	0.386
		(2 engine)	400	3,8	350	2,2	80	0.176	
3.	«Bidarrieus-1» rheostats 1,2	(1engine)	400	3,8	350	2,4	80	0.19	0.41
		(2engine)	400	3,8	350	2,2	100	0.22	
III-series of experiments, swapped engines									
1.	«Bidarrieus-1» rheostats 1,2	(2 engine)	420	4	390	2.5	90	0.225	0.435
		(1 engine)	420	4	390	2.2	95	0.21	
2.	«Bidarrieus-1» rheostats 2,1	(1 engine)	450	4	390	2.4	85	0.204	0.468
		(2 engine)	450	4	390	2.4	110	0.264	
3.	"Bidarrieus-1" with tight springs rheostats 2.1	(2 engine)	400	3.4	300	2.0	70	0.14	0.338
		(1 engine)	400	3.4	300	2.2	90	0.198	
4.	2-bladed "Darrieus" rheostats 2,1	(2 engine)	500	4.5	400	2.9	125	0.36	0.36
5.	2-bladed "Darrieus" rheostats 1,2	(2 engine)	500	4.5	420	3	105	0.315	0.315
IV-series of experiments, swapped engines									
1.	«Bidarrieus-1» rheostats 2,1	(2 engine)	450	3.8	350	2.2	100	0.22	0.472
		(1 engine)	450	4	350	2.4	105	0.252	
2.	«Bidarrieus-1» rheostats 1,2	(1 engine)	450	3.8	380	2.2	120	0.264	0.498
		(2 engine)	450	4	380	2.6	90	0.234	
3.	"Bidarrieus-1" with tight springs rheostats 1.2	(2 engine)	400	3.2	350	2.0	120	0.24	0.465
		(1 engine)	400	3.4	350	2.5	90	0.225	
4.	"Bidarrieus-1" with tight springs rheostats 2.1	(2 engine)	400	3.2	320	2.2	90	0.198	0.438
		(1 engine)	400	3.4	320	2.4	120	0.24	
5.	2-bladed "Darrieus" internal shaft rheostats 1.2	(1 engine)	500	4.5	400	2.6	120	0.312	0.312
6.	2-bladed "Darrieus" internal shaft rheostats 2.1	(1 engine)	500	4.5	420	2.8	100	0.28	0.28

The main dimensions are shown in figure 5. Experimental plots are presented in dimensionless terms. The Figure 5 shows the experimental profiles $\bar{p}$ obtained in five sections (in front of the turbine, inside the rotating turbine, then in three sections after passing the turbine) in which the measurements were made. A

schematic representation of the cross sections of the airflow in the working area with a rotating model of the Darrieus wind turbine is shown in Figure 6.
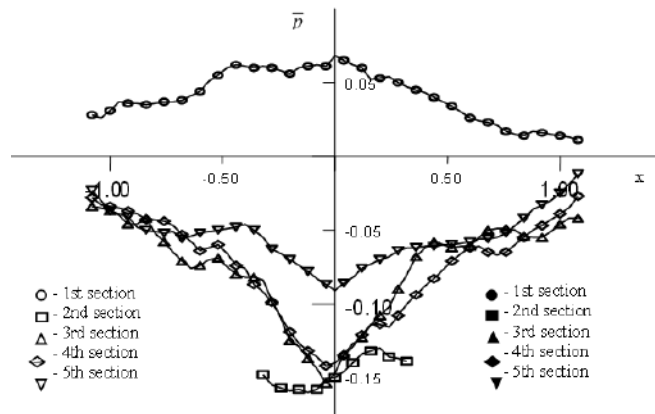
Fig. 5. Experimental data on the distribution of pressure in various sections of the air flow during turbine operation

As can be seen from the graph, the pressure in front of the rotating turbine is positive. Naturally, near the central line, the flow deceleration is significant; accordingly, the pressure is higher. As you move away from the center line on both sides, the flow deceleration weakens, and the pressure tends to the pressure inside the working chamber (P_∞). The lowest value of static pressure was shown by measurements in the next section, which was made inside a cylindrical cavity bounded by the swept surface. The next three sections, as seen in Fig. 3 were located in the wake of the rotating turbine. The data in Fig. 3 clearly shows the process of pressure recovery as you move away from the wind turbine; the results of measuring the static field reflect the physics of the phenomenon.
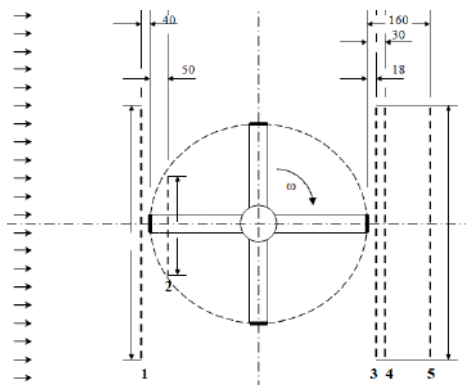
Fig. 6. Schematic representation of the cross sections of the air flow in the working area from the rotating model of the wind turbine Darrieus.

Finally, it is of interest to consider the nature of the curvature of the streamlines during the passage of an airflow through a wind turbine. The deviation of the flow from rectilinear motion is already observed when approaching the turbine. The streamlines begin to deviate slightly (2-2.5°) from straightness when they meet the rotating blades. Moreover, the greatest deviation takes place in the area of oncoming flow and blades (quadrant I in Fig. 8). In the area of the outgoing movement of the blades (quadrant II in Fig. 8), the deviations do not exceed (0.5-1)°, i.e. within measurement error. The same thing happens on the leeward side of the swept surface. The streamlines here in quadrant IV (Fig. 8) also deviate toward the moving working blades. However, it is noticeably stronger (5-6°). In quadrant III, the deviations are very weak.

On fig. Figure 7 shows the measurement data of the velocity field in the same five sections. In the upper part of the graph, there are velocity profiles (dark dots), below the values of their cubes are given in order to be able to estimate the loss of wind energy when passing through a rotating wind turbine (the notation is the same as in Fig. 5). In order to consolidate the illustrative material and provide an opportunity for a more detailed study of the experimental profiles, they are somewhat shifted relative to each other.
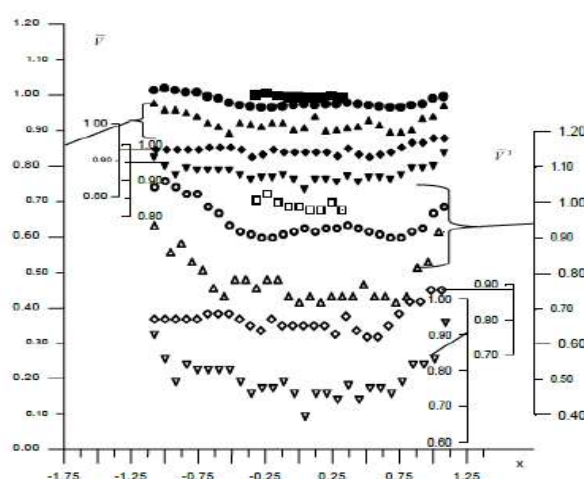
Fig.7. Plots of speeds and energy of the air flow in several sections during the operation of a four-bladed Darrieus wind turbine.
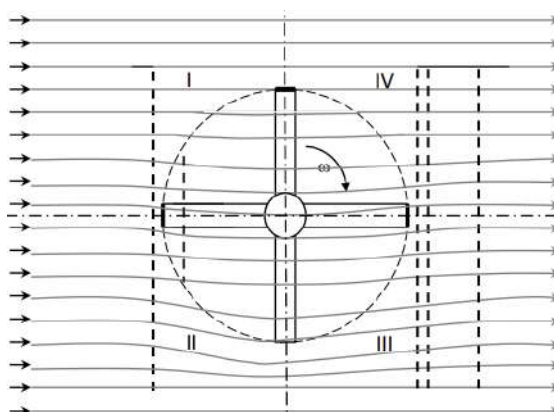
Fig.8. Streamlines plotted based on velocity direction measurement data

Otherwise, it is difficult to get a clear perception of the measurement results due to the overlap of measurement data of different cross-sections. It is easy to see that the air slows down in front of the wind turbine and accelerates somewhat in the second section, which is obviously due to a significant rarefaction of the leeward side of the working blade. As for the three sections behind the wind turbine, where the velocity field changes little (see coordinate scales), which is associated with the use of part of the energy of the airflow by the rotating turbine. This can be seen from the data $\overline{V}^3$ characterizing the energy of the airflow. Then the streamlines are straightened, going into the receiving part of the wind tunnel. Similar patterns should be observed in natural conditions, the wind flow deviates to one side when it meets the turbine, and to the other on the leeward side. The streamlines then apparently take the general direction of the wind.

Conclusions

The universal laboratory model of a carousel-type wind power plant made it possible to study both in the "Darrieus", and "Bidarrieus" modes. In this regard, the following tests were carried out:

1. Testing the model in the Darrieus mode at idle to determine the nature of its rotation in the airflow.

2. Tests of the Darier model with current generators.

3. Several series of experiments were carried out with the model in the "Darrieus", and "Bidarrieus" modes in order to obtain comparative characteristics, which is the main task of the tests.

4. At the end of the power tests, an aerodynamic experiment was carried out using a three-channel probe to analyze the distribution of the velocity and pressure field in front of the turbine, inside the cylindrical surface swept by the working blades, and also behind, behind the wind turbine

5. On the basis of a direct physical experiment, experimental data on the distribution of velocity, pressure and the nature of the change in the streamline near the operating wind turbine were obtained.

6. Despite the fact that this is a good indicator of the efficiency of the Darrieus turbine, the authors have developed a new version of the turbine, which allows increasing the effective value of this coefficient up to 1.5 times

REFERENCES

1   Darrieus F.M. *Turbine Having in Rotation Transverse to the Flow of Current*, US Patent 1.834/ 018 Dec. USA, 1931, 3 p.

2   Tjiu W., Marnoto T., Mat S., Ruslan M.H., Sopian K. Darrieus vertical axis wind turbine for power generation I: Assessment of Darrieus VAWT configurations. *Renewable Energy*. 2015. Vol.75, pp. 50 –67.

3   Tjiu W., Marnoto T., Mat S., Ruslan M.H., Sopian K. Darrieus vertical axis wind turbine for power generation II: Challenges in HAWT and the opportunity of multi-megawatt Darrieus VAWT development. *Renewable Energy*. 2015. Vol.75, pp. 560–571.

4   Paraschivoiu I. *Wind turbine design e with emphasis on darrieus concept.* Quebec: Presses Internationales Polytechnique; 2002, 483 p.

5   Yershina A. K., Yershin Sh. A., Zhapbasbayev U.K. *Fundamentals of the theory of Darreus wind turbines*. Almaty, Kazgos INTI. 2001, 104 p. [in Russian]

6   Wang Y., Shen S., Li G., Huang D., Zheng Z. Investigation on aerodynamic performance of vertical axis wind turbine with different series airfoil shapes. *Renewable Energy*. 2018. Vol. 126, pp. 801–818.

7   Gorelov N.D. Energy characteristics of the Darrieus rotor (review). *Thermophysics and Aeromechanics*, 2010. Vol.17, pp. 301 – 308.

8   Yershin Sh., Yershina A.K., Ydyryssova A.A. Vertical–axial two–rotor wind power units Bidarrieus-1. *Eurasian Physical Technical Journal*. 2017. Vol. 14, No. 2(28), pp. 108 – 112.

9   Kumar R., Raahemifar K., Fung A.S. A critical review of vertical axis wind turbines for urban applications. *Renew. Sustain. Energy Rev.* 2018. Vol. 89, pp. 281 – 291.

THE METHOD OF CORIUM COOLING IN A CORE CATCHER OF A LIGHT-WATER NUCLEAR REACTOR

Skakov M.K.[1], Toleubekov K.O.[2,3], Baklanov V.V. [2], Gradoboev A.V. [4], Akayev A.S. [2], Bekmuldin M.K. [2,3]

[1] National Nuclear Center of the Republic of Kazakhstan, Kurchatov, Kazakhstan
[2] Institute of Atomic Energy NNC RK, Kurchatov, Kazakhstan, toleubekov@nnc.kz
[3] Shakarim University, Semey, Kazakhstan
[4] National Research Tomsk Polytechnic University, Tomsk, Russia

During the development of a severe accident at nuclear power plant with a core melting, corium is formed. One of the main barriers preventing outflow of corium into the environment is a melt localization device or a melt trap. The melt trap must accept and prevent the corium parameters from exceeding critical values, ensuring its retention in a controlled volume and cooling. For this reason, melt traps are subject to serious requirements regarding cooling methods to ensure effective containment of the melt in the core of a nuclear reactor. In the presented article, experimental studies of the interaction between corium and water, which was supplied to the surface of the corium in a melt trap for its cooling, were analyzed. As a result of the work, a number of significant problems associated with the low efficiency of this cooling method were identified, and possible ways to eliminate them were considered. A solution is proposed for optimizing the method of corium cooling in a melt trap, as well as for the scope of research on the possibility of implementing the proposed method in practice and analyzing its effectiveness using the VCG-135 test-bench and the Lava-B facility.

Introduction

One of the main directions of research in the field of operation of nuclear power plants is the issues of its safety, in particular, the localization and cooling of the melt from the structural materials of the core (corium) during the development of a severe accident with loss of coolant. At the same time, this process is carried out in the so-called melt localization device (MLD) of the core, located under the power vessel of the reactor. The main task of the melt localization device is to accept and cool the corium in the localization volumes as quickly as possible in order to prevent its heating, outflow of non-volatile fission products and prevent the formation of re-criticality [1].

To date, there are several options of the under-reactor melt trap [2], among which the most well-known are the so-called "crucible" options of the melt trap for trapping molten materials from the core. These traps are already used at existing nuclear power plants, such as the Taiwan NPP in China, and at power units currently under construction with the latest Russian-made water-water energetic reactor (WWER) [3].

Corium is a mixture of two components that are immiscible with each other: metal and oxide. The metal component of the corium is formed as a result of the melting of steel internals and the wall of a nuclear reactor, and the oxide component is formed as a result of the melting of pellets with nuclear fuel and the dissolution of metal zirconium and zirconium oxide in this melt, formed as a result of oxidation of metal zirconium by water vapor and atmospheric oxygen. The density of the metal part of the corium is less than that of the oxide part, which causes stratification of these melts in the joint presence [4].

To cool the corium and prevent it from leaving the trap, the concept of cooling the corium in a crucible trap was developed. The concept is based on filling the under-reactor space with blocks of cassettes filled with sacrificial material. The sacrificial materials, interacting with the corium, change its properties, thereby creating conditions for the reliable operation of the MLD. The role of sacrificial materials is to dilute the heat-producing oxide part of the corium in order to create conditions for the gravitational inversion of parts of the corium and reduce its high temperature [5]. The melt formed in the trap is cooled by heat removal to the cooling

water through the shell, as well as by water supplied directly to the melt surface. The described system is operable, however, in the course of further research, it was found that the corium-water interaction has serious negative phenomena: the formation of explosive hydrogen during steam-metal reactions and the threat of steam explosions as a result of a batch outflow of corium from the reactor pressure vessel [6].

Obviously, in order to prevent negative consequences during the development of a severe accident at a nuclear power plant, it is necessary to conduct experimental studies on the interaction of corium with cooling water in order to better understand the ongoing processes. For example, such experiments are in demand in studies that have been and are being carried out as part of the development of the concept and the creation of severe accident control systems by cooling down, controlled movement and localization of the core melt outside.

The purpose of this article is to review previous experimental studies of the interaction between corium and cooling water. As a result of the work, problems were identified that arise when water is directly supplied to the melt pool, an analysis of existing methods for eliminating the identified problems was made, and an optimization solution was proposed to minimize these disadvantages.

1. Interaction of water with corium

A feature of the localization of the core melt in the melt trap is the portioned outflow of the corium from the reactor pressure vessel. In this case, water for cooling the corium is supplied immediately after the first portion of the corium enters the trap. This leads to the fact that at outflowing of the second portion of the corium (approximately 0.5 - 1 hour after the outflow of the first portion), a water pool is formed on the surface of the melt. In this case, when a high-energy melt falls into a container filled with water, there is a possibility of a steam explosion, as a result of which not only the device for trapping the molten materials of the core, but also the concrete burden with a sealed zone can be destroyed [7].

The first major studies on the conditions for the occurrence of steam explosions during severe accidents at nuclear power plants were conducted at the Sandiev Laboratories (USA) in the well-known series of FITS experiments. As a result of research, steam explosions occurred with water volumes from 44 l to 0.25 m^3 with a melt mass of 3 to 20 kg. At the same time, the contact of some melts with the coolant did not lead to an explosion, and a clear effect of the composition of the melt on the explosion hazard is also traced. With an open geometry, in most experiments with Al_2O_3-Fe, a spontaneous explosion was observed ($\eta\infty$ from 0.2% to 3% of the total thermal energy of the melt), while no explosions were observed when using an A + R corium mixture [8]. Similar experiments conducted at the Premix test-bench in Karlsruhe showed that the fall of, for example, only 20 kg of melt into a 0.5 m3 container with water leads to steam explosions with a pressure increase above 2 MPa, which ultimately destroyed the installation [9].

However, the opposite pattern was observed as a result of nine experiments conducted in a series of WUMT experiments, where a 24 kg melt was poured by gravity through a washer into a tank of water. In this series of experiments, a steam explosion took place in only two out of nine experiments. In experiment 03, the explosion occurred before the melt reached the base of the vessel. In this case, the subcooling of the water was 80 K, and this large subcooling can be considered responsible for the spontaneous initiation of the explosion that took place. In experiment 09, an explosion occurred in water that was on the saturation line 0.5 seconds after the melt reached the base of the vessel [10].

In a similar series of HPTR experiments, in which 5 kg of the melt was poured into a water volume (1 l) located in a pressure vessel, the only initiator of a steam explosion that had an effect was a large flow of water. In experiment 05, it initiated a steam explosion, and in experiments 13 and 14, it led to enhanced vaporization. The steam explosion in experiment 05 took place at a pressure in the vessel of 5.8 MPa (the pressure increase before the explosion was caused by the mixing of water and melt in a closed volume) [11]. Typical out-of-vessel steam explosion conditions occurring during a severe accident were simulated in the COTELS project experiments (Series A). In all these experiments, there was no pressure surge typical for a steam explosion. The largest pressure peak was recorded in the A8 experiment, where the corium fell at the highest rate [12].

During the experimental studies on the interaction of water with melts, additional features were noticed. Thus, as a result of the FARO experiments, information was obtained that a significant amount of hydrogen is produced during the corium-water interaction. Since the composition of the melt in this case was the same as in the KROTOS experiments, it is likely that hydrogen was also formed in them. Although during the described

KROTOS experiments there were no devices for detecting the appearance of hydrogen during mixing of water and melt, its presence can be concluded from calculations based on the results of the KROTOS 41 and KROTOS 45 experiments using the COMET code [13–14].

These results have led to the emergence among specialists of scenarios of a hydrogen explosion during the supply of water to the corium. There is evidence that corium is a system of two immiscible liquid phases—oxide and metal. Due to the difference in densities of the two systems, the metal part of the corium is located above the oxide one, that is, water is directly supplied to this system of the corium to cool it.

Experiments on the interaction of water with steel melts have shown that even at temperatures above 1300 K, intense interaction of metals with water and steam occurs with the formation of hydrogen. Experimental studies have confirmed the importance of the processes of hydrogen formation during high-temperature oxidation with water and water vapor of steel melt as an additional source of hydrogen, which should be taken into account in hydrogen safety [15].

In this regard, it can be assumed that with the active interaction of water with the metal part of the corium, there is a possibility of the formation of a critical concentration of hydrogen, which can lead to its detonation, which, in turn, means that the conditions for hydrogen safety cannot be met, which means, containment integrity cannot be met as well. An additional problem of interaction with water of the metal part of the corium (especially zirconium) is the release of a large amount of heat caused by chemical reactions, as well as the combustion of the resulting hydrogen and oxygen [16].

Thus, as a result of the analysis of previous studies of the interaction between corium melt and water, the following conclusions can be drawn:

- In major part of experiments, steam explosions have not been observed, but nevertheless, under certain conditions, it occurs. This means that when corium falls into the water pool in the melt trap, the probability of a steam explosion is not zero, so further work should be done to prevent steam explosions that threaten the integrity of the melt receiving device;

- During experiments to study steam explosions, it was found that during the corium-water interaction, a significant amount of hydrogen is generated. At the same time, in many experiments there were no sensors for detecting hydrogen, however, the fact of the presence of hydrogen in the gaseous medium is confirmed by subsequent experiments and the created calculation codes.

2. Fundamental solution to the identified problems

Minimizing the formation of hydrogen and reducing the threat of a steam explosion in a crucible-type melt trap is expected by applying the concept of gravitational inversion of parts of the corium. Sacrificial materials are the central object in the implementation of this concept. Sacrificial materials are used to dilute the heat-generating oxide part of the corium in order to create conditions for the gravitational inversion of parts of the corium and reduce its high temperature.

In crucible devices for localizing the melt, it is assumed that, being melted when heated from the melt, sacrificial materials form a composition with the uranium-containing oxide part of the fuel melt, the specific density is lower compared to the metal part of the corium, which, in turn, will allow the oxide phase to float to the top part of the trap. When liquid oxides enter the surface, the cooling water does not create a threat of steam explosions, which is associated with the thermophysical features of liquid oxides, and does not enter into chemical reactions with them to form hydrogen, does not undergo thermal decomposition due to the relatively low temperature of the melt mirror [17].

To substantiate the possibility of implementing this concept, a series of experiments was carried out to study the interaction of candidate sacrificial materials and corium in a crucible-type melt trap within the framework of numerous series of experiments, among which Melt, Vesta, CORMIT [18–20]. As a result of experimental studies of the interaction of candidate sacrificial materials with corium, it was found that ceramic materials are the most optimal sacrificial materials. For example, ceramics based on hematite and alumina were chosen as the sacrificial material for the melt trap of the WWER-1000 reactor. The experiments showed that the mutual dissolution of the sacrificial material and the melt occurs at a rate sufficient to implement the inversion of the oxide and metal layers in <1 h [21]. Thus, the possibility of implementing the concept of

gravitational inversion was experimentally confirmed, and after its implementation, the generation of hydrogen will significantly decrease, and the probability of a steam explosion will be minimal.

3. Optimization of the method for cooling corium in a melt trap

The comparison table summarizes all the information about the issues that have arisen during using water as cooling for the corium in the core catcher and possible solutions, Table 1.

Table 1. The comparison table about the issues and their possible solutions

The issue	Consequences of interaction with water	Way to solve the problem
Two-phase composition of the corium	Hydrogen explosion	Use of sacrificial materials to create conditions for gravitational inversion
The portioned output of corium from vessel	Steam explosion	Delay water supply to the core catcher

The core catcher of a light water reactor of the WWER type was chosen as the object of study in this work. For the first time, such a core catcher was installed during the construction of power units with WWER-1000 reactors at the Tianwan NPP. To date, the core catcher of the new WWER-1200 reactor, although it differs by minor structural changes and the materials used [22], the concept of corium cooling remains unchanged. It consists in diluting the corium with sacrificial materials for its further oxidation and the rise of the oxide part in order to reduce the intensity of hydrogen generation, reduce the volumetric energy release and increase the heat exchange surface with the trap casing while simultaneously supplying water to the surface of the corium.

Elimination of the problem of hydrogen generation in melt traps is planned due to inversion of the metal and oxide layers of the corium when sacrificial materials are dissolved in them. However, its implementation takes a certain amount of time, and the water supply should be started immediately at the moment the corium enters the trap due to the danger of the system going beyond the permissible limits (the beginning of the boiling of uranium dioxide) due to residual heat release in the corium [23]. As a result, during the period of time when the metal part is on the surface of the melt, water is supplied to it, which increases the process of increasing the generation of hydrogen, and given the portioned release of corium from the reactor pressure vessel, steam explosions.

On the basis of the foregoing, methods of melt cooling become very relevant, excluding the direct supply of water to the surface during the period of portioned release of the corium and until the completion of the gravitational inversion of the corium layers to prevent the likelihood of steam explosions and the generation of a large amount of hydrogen.

For this reason, the idea arose to use a non-aqueous coolant until the end of the gravitational inversion process to prevent steam explosions and generate a large amount of hydrogen. The proposed concept is based on the idea that when the corium enters the trap, the cooling material will move to its surface due to the density difference and will remove heat from the corium during the time period when water supply to the corium is undesirable. After the complete release of the corium and the completion of the process of inversion of its layers, water will begin to flow to its surface, and the selected material should undergo a phase transition of boiling and leave the trap. Thus, when using the proposed concept of corium cooling, it is supposed to reduce the probability of a steam explosion in the trap, as well as to reduce the intensity of hydrogen formation to a safe level.

In this regard, as candidate materials for the implementation of the proposed concept, materials with a lower density relative to the corium and having phase transition points significantly below the corium formation temperature should be considered.

One of the most optimal materials for cooling corium are metals. This article proposes to consider low-melting metals as a non-aqueous coolant. Since there is a possibility of accidental ingress of water into the area of melt localization, then when choosing a metal as a heat-removing material, in the first approximation, one should consider metals that are in the electrochemical series of metals to the right of hydrogen. However, few metals to the right of hydrogen in the activity series can be used as a cooling material not only in terms of

physicochemical properties, but also for economic reasons. In this regard, metals were also considered, standing in the activity series on the left side of hydrogen.

To determine the most suitable candidate material, an analysis of the physicochemical properties of various metals was carried out, which were based on information from sources [24-25]. Table 2 lists some metals with a density below or approximately equal to the average corium density ($\rho \sim 7315$ kg/m3 [26]) that can be used as a cooling material. During analyzing the properties of metals, alkali metals were not considered due to their extremely high chemical activity.

Table 2. Properties of Candidate Metals

Name	Atomic number	Densityρ, kg/m^3	Melt temperature T_{melt}, °C	Boiling temperature T_{boil}, °C	Specific heat of melting λ, kJ/mol	Specific heat of boiling$L$, kJ/mol
Beryllium	4	1848	1278	2970	12.21	309
Magnesium	12	1739	650	1090	9.2	131.8
Calcium	20	1540	839	1484	9.2	153.6
Strontium	38	2630	769	1384	9.2	144
Barium	56	3760	729	1637	7.66	142
Aluminum	13	2698	660	2518	10.75	284
Titanium	22	4505	1670	3287	18.8	422.6
Antimony	51	6691	631	1635	20.08	195.2
Zinc	30	7133	420	906	7.28	114.8
Chromium	24	7190	1857	2672	21	342
Manganese	25	7210	1243	1961	13.4	221
Tin	50	7310	232	2620	7.19	296

According to the data given in Table 1, the most optimal metals for cooling the corium that meet the above requirements (the temperature of the corium can reach 2400 °C in the first hours after melting [27]) are antimony, alkaline earth metals (magnesium, calcium, strontium, barium), zinc and manganese.

The chemical activity of alkaline earth metals increases with increasing serial number. In this regard, among the noted alkaline earth metals for use in a melt trap, metals with a lower atomic number are considered the most acceptable, among which magnesium is the most optimal. The chemical activity of magnesium is much lower compared to other alkaline earth metals. This is because magnesium shares some chemical properties with the alkaline earth metals, but is otherwise markedly different from them. Nevertheless, magnesium remains a fairly active metal, so it should be considered as a last candidate.

Alternatives to magnesium are zinc and manganese. Zinc is more preferred as a candidate coolant due to the most optimal parameters (melting and boiling points), as well as its abundance in nature. In addition, zinc is inferior in chemical activity to alkaline earth metals, including magnesium, which is also an advantage. Another candidate material is antimony, which in its properties occupies an intermediate position between metals and nonmetals. The experiments are supposed to use the metallic modification of antimony. Antimony is distinguished by its low reactivity, acceptable melting and boiling points (more favorable relative to manganese), and unique chemical properties inherent in the so-called metalloids, which are of particular interest for their study when interacting with corium.

The use of zinc, and especially antimony and manganese, as possible coolants can cause difficulties in the sense that there is a possibility of their incomplete boiling out from the melt at the end of the inversion of corium parts. However, it is assumed that, being melted when heated from the corium, the sacrificial materials form a composition with a specific density of less than 6.4 kg/m^3 with the uranium-containing oxide part of the corium [28]. This means that due to the higher density, the rest of the coolant volume will also exchange position with the new mixture of sacrificial materials and the oxide part of the corium, thereby preventing dangerous hydrogen formation processes after the start of water supply to the melt.

4. Experimental studies of the proposed optimization of the corium cooling method

Based on the above, we can draw conclusions about the potential feasibility of the proposed cooling method. To confirm which, it is necessary to obtain information on the nature of the interaction of the selected materials with the corium, the efficiency of heat removal, etc. These issues require computational - theoretical and experimental study.

Thus, it seems appropriate to conduct a series of small- and large-scale experimental studies of the interaction between corium and candidate metal coolants in order to further develop recommendations on the possible use of the proposed cooling method in existing and future melt traps at nuclear power plants.

The method of physical modeling is the most effective way to confirm the operability of the proposed method, since it will allow simulating the situation of corium entering the melt trap from the reactor pressure vessel during a severe accident with a core meltdown. At the same time, experimental studies will be carried out on the VCG-135 test-bench and the Lava-B facility, created at the Institute of Atomic Energy Branch, RSE NNC RK [29]. The VCG-135 test-bench is designed to perform small-scale high-temperature material science studies of small-sized samples. The main components of the test-bench are a high-frequency electric lamp generator, a sealed, water-cooled working chamber with an inductor, a system for supplying and removing working gases into the working chamber, and an information-measuring system (IMS) of the test-bench. The appearance of the test-bench is shown in Figure 1.

Fig.1. Outer view of the VCG-135 test-bench.

The VCG-135 test-bench allows controlled heating of any small-sized samples in the working chamber to high temperatures (~ 3000 °C). At the same time, various studies are carried out at the test-bench to study the interaction of corium components with each other and with other structural elements, as well as its physicochemical and thermophysical properties. The scheme and outer view of the working chamber of the VCG-135 test-bench are shown in Figure 2.

In this case, VCG-135 is usually used mainly for small-scale experiments in addition to large-scale experiments performed at the Lava-B facility. Thus, the goal of future small-scale experiments on the test-bench is to determine the most optimal metal coolant for its testing at the Lava-B facility. Lava-B experimental facility includes two main functional units: an electric melting furnace (EMF) for preparing the melt of the prototype corium and a melt receiver (MR), which houses the experimental section for modeling the processes under study. The prototype corium, which consists of uranium dioxide, zirconium dioxide, zirconium and steel with a total mass of up to 60 kg, is melted in an induction electric melting furnace (EMF), and then merges into a melt trap equipped with a special heater to simulate residual energy release, which is placed in melt receiver (MR). The outer view and layout of the Lava-B facility is shown in Figure 3.

In experimental studies of severe accidents, a corium simulator, the so-called "prototype corium", is used, a substitute whose characteristics are assumed to be quite close to the true ones. The essential difference between the prototypical and real corium is that the former is not a source of heat, that is, there is no self-sustaining radioactive decay in the prototypical corium [30].

a   *b*
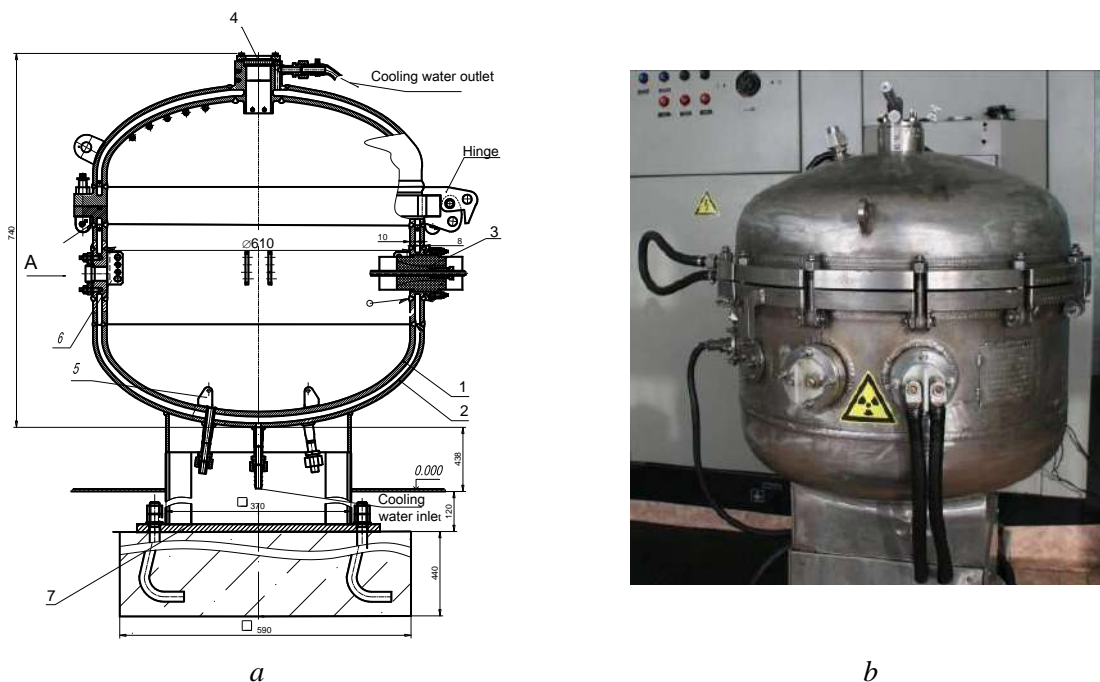
Fig.2. Outer view and scheme of the VCG-135 working chamber:
1 – inner casing of the pressure vessel; 2 – outer casing of the pressure vessel; 3 – inductor current lead; 4 – optical window; 5 – brackets for mounting the experimental assembly; 6 – electrode holders; 7 – base
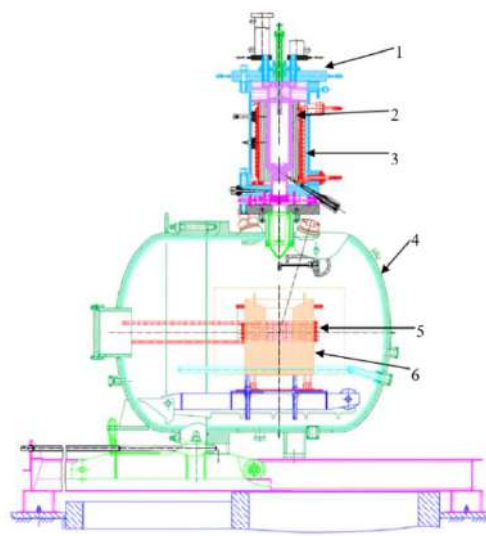
Fig.3. Outer view and scheme of the Lava-B facility: 1 – EMF (electric melting furnace), 2 – graphite crucible, 3 – EMF inductor, 4 – MR (melt receiver), 5 – MR inductor, 6 – concrete trap.

Therefore, to ensure conditions as close as possible to real ones, not only the correspondence of the composition of the prototype corium to the real corium should be taken into account, but also the presence of energy release in the melt to simulate a heat source in the corium. The importance of simulating the residual energy release is determined by the fact that the energy release in the melt significantly affects the nature of the interaction of its elements. At the Lava-B facility, depending on the goals and conditions, both induction and plasmatron heaters are used [31-32]. Many experiments are being carried out at the Lava-B facility to study the processes that accompany a severe accident in a light water power reactor [33–36]. The result of the work already carried out is the obtained valuable information on the possibility of managing a severe accident at different stages of its development.

Conclusion

The concept of a melt trap crucible device is predominantly the main choice in the construction of NPP passive safety systems. The operability of this concept was confirmed by both computational and experimental methods. However, this concept still has disadvantages associated with the initial stage of corium localization in the core catcher: the formation of explosive hydrogen during steam-metal reactions and the threat of steam explosions as a result of a batch outflow of corium from the reactor vessel.

In the scenario when water for cooling the corium is supplied immediately after the first portion of the corium enters the trap. This leads to the fact that at outflowing of the second portion of the corium (approximately 0.5 - 1 hour after the outflow of the first portion), a water pool is formed on the surface of the melt. In this case, when a high-energy melt falls into a container filled with water, there is a possibility of a steam explosion, as a result of which not only the device for trapping the molten materials of the core, but also the concrete burden with a sealed zone can be destroyed.

The second challenge is that corium is a mixture of two components that are immiscible with each other: metal and oxide. Due to the density difference between the two systems, the metal part of the corium is above the oxide part. This means that water is supplied directly to the metal part of corium. In that regard, it can be supposed that with the active interaction of water with the metal part of the corium, there is a possibility of the formation of a critical concentration of hydrogen and its detonation in the end. This means that the conditions of hydrogen safety and integrity of the containment cannot be reached.

To solve the above-mentioned disadvantages, part of the core catcher is filled with sacrificial material. Sacrificial materials are used to dilute the heat-generating oxide part of the corium in order to create conditions for the gravitational inversion of parts of the corium and reduce its high temperature. The experiments showed that the mutual dissolution of the sacrificial material and the melt occurs at a rate sufficient to implement the inversion of the oxide and metal layers in <1 h. Thus, the possibility of implementing the concept of gravitational inversion was experimentally confirmed, and after its implementation, water is supplied to the melt to cool it.

On the basis of the foregoing, methods of melt cooling become very relevant, excluding the direct supply of water to the surface during the period of portioned release of the corium and until the completion of the gravitational inversion of the corium parts. As a result, authors have the idea arose - to use a non-water cooler until the end of the gravitational inversion process to prevent steam explosions and generate a large amount of hydrogen. The most optimal coolants in this case are fusible metals with melting and boiling points, as well as a density below corium. The literature analysis of the physicochemical properties of known metals made it possible to select candidate metals that meet these requirements and can be used in melt localization devices during a severe accident at NPP.

Based on the above, we can draw conclusions about the potential feasibility of the proposed cooling method. To confirm which, it is necessary to obtain information on the nature of the interaction of the selected materials with the corium, the efficiency of heat removal, etc. These issues require computational - theoretical and experimental study. The method of physical modeling is the most effective way to confirm the operability of the proposed method, since it will allow simulating the situation of corium entering the melt trap from the reactor pressure vessel during a severe accident with a core meltdown. At the same time, experimental studies will be carried out on the VCG-135 test-bench and the Lava-B facility, created at the Institute of Atomic Energy Branch, RSE NNC RK.

Thus, it seems appropriate to conduct a series of small- and large-scale experimental studies of the interaction between corium and candidate metal coolants in order to further develop recommendations on the possible use of the proposed cooling method in existing and future core catchers at nuclear power plants.

REFERENCE

1   Kukhtevich I.V., Bezlepkin V.V., Khabensky V.B., et al. The concept of localization of the corium melt in the exvessel stage of a severe accident at a nuclear power station with a WWER -1000 reactor, *Proceeding of the conf. "Safety Issues of NPP with WWER"*, St. Petersburg, 2000, Vol.1, pp. 23 – 36. [in Russian]

2   Molchanov I.A., Shumilin M.P. Retention of the core melt inside the containment during severe accidents of nuclear power units, *Eastern-European journal of enterprise technologies*. 2011. No.2(8), pp. 65 – 67. [in Russian]

3   Sidorov A.S., Rogov M.F., Novak V.P., et al. Core catcher of the Tianwan NPP. Design and functioning, *Proceeding of the Conf. "Safety Issues of NPP with WWER"*, St. Petersburg, 2000, Vol.1, pp. 37 – 66. [in Russian]

4   Udalov Ju.P., et al. Special materials for passive control of over project accidend of nuclear reactor during out of tank stage of active zone melt localization. Part I, *Bulletin of St PbSIT(TU)*. 2010. No.8(34), pp.17 – 24. [in Russian]

5   Gusarov V.V., Almyashev V.I., Beshta S.V., et al. Sacrificial materials for the safety system of nuclear power plants - a new class of functional materials. *Thermal Engineering*. 2001. No.9, pp.22–24. [in Russian]

6   Sehgal B.R., et al. *Melt-Structure-Water Interactions During Severe Accident in LWRs*. NPSD, Royal Institute of Technology, Annual Report, Sweden, Nov. 2000, 147 p.

7   Sidorov A.S., Nosenko G.E., Granovsky V.S., et al. *The containment protection system of a water-cooled reactor plant*, RF Patent No. 2165108, 2001, 10 p. [in Russian]

8   Mitchell D.E., Evans N.A. *Steam explosion experiments at intermediate scale: FITS B Series*. NUREG/CR-3983, SAND 83-1057, R3, Sandia Natl. Lab., Albuquerque, NM, 1986, 89 p.

9   Kuczera B. Leichtwasserreaktor-Sicherheitsforschung. *Atomwirtschaft*, 1996, Bd.41, No.12, pp.783 – 787. [in German]

10   Fletcher D.F. A Review of the Available Information on the Triggering Stage of Steam Explosion, *Nuclear Safety*. 1994. Vol.35, No.1, pp.36-57.

11   Fletcher D.F. Steam explosion triggering: a review of theoretical and experimental investigations, *Nuclear Engineering and Design*. 1995. Vol.155, No.1-2, pp.27-36

12   Kato M., Nagasaka H., Vasilyev Y. Fuel Coolant Interaction Tests using UO2 corium under EX-vessel Conditions, *JAERI-Conf.*, 1999, p. 304.

13   Annunziato A. Progresses of the FARO/KROTOS Test Programme. *CSARP*, 1995, 13 p.

14   Huhtiniemi I., Magallon D., Hohmann H. Results of recent KROTOS FCI tests alumina Versus corium melts, *Nuclear Engineering and Design*. 1999. Vol. 189 (1- 3), pp. 379-389.

15   Muradov N.Z. *Obtaining concentrated hydrogen by thermal contact method*. VANT, AVE&T, 1987, 40p. [in Russian]

16   Stolyarevsky A. Does the trap save? *Atomic strategy XXI*. 2014. No.89, pp.16–18. [in Russian]

17   Nedorezov A.B. *Localization and cooling system of the core melt of a water nuclear reactor*, RF patent No.2576517, 2016. [in Russian]

18   Gusarov V.V., et al. Sacrificial materials for the safety system of nuclear power plants - a new class of functional materials. *Thermal Engineering*. 2001. No.9, pp. 22 – 24. [in Russian]

19   Jin Ho Song, Hwan Yeol Kim, Seong Wan Hong, Sangmo An. A use of prototypic material for the investigation of severe accident progression, *Progress in Nuclear Energy,* 2016, Vol. 93, pp. 297-305

20   Project "Cormit-II" *(Jan30, 2020).* Available at*:* https://www.nnc.kz/ru/news/show/215

21   Asmolov V.G. et al. Choice of Buffer Material for the Containment Trap for WWER -1000 Core Melt, *Atomic Energy*. 2002. Vol. 92, pp. 5–14 [in Russian]

22   Sidorov I.A. The core catcher for nuclear power plants with WWER -1200. *Proceedings of the 7th ISTC "Ensuring the safety of nuclear power plants with* WWER *" OKB «GIDROPRESS»*. 2011, 13 p. [in Russian]

23   Stolyarevsky A.Y. Nuclear power plants: now with a "trap", *Energy*, 2002, No.4, pp. 9–17

24   Perelygin Yu.P., Yakovleva E.G., Firulina L.M. et al. *Metals. General chemical and physical properties,* Penza: PSU Publishing House, 2016, 114 p. [in Russian]

25   Chirkin V.S. *Thermophys.properties of nuclear engineering materials*. Atomizdat. 1968, 356 p. [In Russian]

26   Asmolov V.G., Zagryazkin V. N., Astakhova E.V. et al. Density of UO2–ZrO2 melts. *High Temperature*. 2003. Vol. 41(5), pp. 714 – 719. [in Russian]

27   Wood J. Nuclear Power. *Institution of Engineering and Technology. Nuclear power,* IET, 2007, 256 p.

28   Stolyarevsky A.Y. The problem of fuel melt retention in the containment of WWER. *Alternative Energy and Ecology (ISJAEE)*. 2014. No.6, pp. 25-35. [In Russian]

29   Nazarbayev N.A., Shkolnik V.S., Batyrbekov E.G., et al. *Scientific, Technical and Engineering Work to Ensure the Safety of the Former Semipalatinsk.* Kurchatov, 2016, Vol.3, pp. 320 – 356. [In Russian]

30   Christophe Journeau *Contribution des essais en matériaux prototypiques sur la plate-forme PLINIUS à l'étude des accidents graves de réacteurs nucléaires. Sciences de l'ingénieur* , Université d'Orléans, 2008, 29p. [In French]

31   Maruyama Y., Tahara M., Nagasaka H. et al. Recent results of MCCI studies in COTELS project. *Proceedings of the NTHAS3: Third Korea-Japan Symposium on Nuclear Thermal Hydraulics and Safety Kyeongju*, Korea, 2002, 6 p.

32   Zhdanov V., Baklanov V., Bottomley P.W.D. et al. Study of the processes of corium-melt retention in the reactor pressure vessel (INVECOR), *Proceedings of the "ICAPP 2011"*. Nice, France. 2011, pp.1300 – 1308.

33   Tomohisa Kurita, Isao Sakaki, Fumiyo Sasaki et al. Test and evaluation plan for passive debris cooling system. *Proceedings of the 9th Intern. Conference nuclear and radiation physics,* Almaty, 2013 pp. 19 – 29.

34   Shohei Kawano, et al. Characterization of fuel debris by large-scale simulated debris examination for Fukushima Daiichi nuclear power station, *Proc. of ICAP 2017*, Fukui and Kyoto, 2017, pp. 1105 - 1110.

35   Vasiliev Yu.S., Vurim A.D., Zhdanov V.S., Zuyev V.A. et al. Experimental studies carried out in IAE on simulation of process typical for reactor severe accidents, *NNC RK Bulletin*. 2009. Vol.40, pp.26-54. [In Russian]

36   Bekmuldin M.K., Skakov M.K., Baklanov V.V et al. Heat-resistant composite coating with a fluidized bed of the under-reactor melt trap of a light-water nuclear reactor. *Eurasian phys. tech. j.* 2021. Vol.18, No.3(37), pp. 65-70.

FEATURES OF ESTIMATION WEARPROOFNESS TRIBOJOINTS BY WORK OF ELECTRON OUTPUT

Tsyganov V. V.[1]*, Sheiko S.P.[2], Sakipov K.E.[3], Kassymov S.S.[4]

[1] Zaporizhzhia Polytechnic National University, Zaporozhie, Ukraine, tsyganov705@gmail.com
[2] Zaporizhzhia National University, Zaporozhie, Ukraine, sheyko.s@mail.ru
[3] L.N. Gumilyov Eurasian National University, Nur-Sultan, Kazakhstan
[3] E.A. Buketov Karaganda University, Karaganda, Kazakhstan

The wear is considered and power - producing state of a surface stratum exemplar after friction with a difficult dynamic loading. The estimation of work destruction and wearproofness tribojoints are analysed. It is shown that the change of character of loading tribojoints is determined the power - producing state of superficial layer and can be appraised in size works of electron output on a surface. The analysis of distribution magnitude work of electron output determines influence of conditions contact interaction to a wear resistance and condition of a superficial layer. It allows determining sites of a surface, which have received a different degree of plastic deformation

Keywords: wear, tribojoints, works of electron output, friction, superficial layer

Introduction

Despite the significant progress achieved in tribology, many problems related to improvement of wear resistance and reduction of friction losses are still not fully understood. This is due to the wide range of mechanical and physicochemical phenomena that occur in the contact zone. Simultaneous analysis of all such phenomena is hardly possible. It is advisable to consider a limited set of informative parameters, which may be sufficient to comprehensively characterize a tribosystem. Moreover, in testing on a friction machine, the tribocontact loading conditions should correspond as closely as possible to the real conditions of tribojoint operation. It is a matter of general experience that a variety of wear mechanisms exist. Variation in any given factor, or the appearance of a new one, can result in changes in the wear mechanism.

Functioning of tribojoints and exit on the optimal mode of wear is determined by the complex of external and internal factors. To the external factors, as is generally known, loading, speed of the relative moving, environment, physical and mechanical properties of materials belong. To internal, it is necessary to take the processes of electric nature. One of basic power-producing descriptions of metals is work of electron output (WEO). It is known that a sum volume and superficial constituents determine WEO. By volume, part of WEO depends on energy of Fermi this metal and very poorly change at deformation. The superficial constituent of WEO can suffer considerable changes at deformations, because determined by the local superficial gallops of potentials, variations of that depend on micro geometry and co-ordination of superficial atoms. Researches by means of the complex independent methods is showed, that changes of WEO were corollary of fatigue processes flowing in relatively thick subsuperficial layer and can be used for the analysis of kinetics flowing of processes fatigue destruction at a friction.

The surface is the most important component of metal parts and it is necessary to control its condition at all stages of the life cycle of the part - during its production, operation and repair. To carry out reliable non-destructive testing of metal parts, specially developed tools and methods for its use are necessary, including WEO [1, 2]. At the same time, it is possible to use both theoretical and experimental studies.

In obedience to a structural and energy theory, fundamental conformity to law of friction and wear shows up due to a main physical mechanism - phenomenon of structural and energy adapt of materials at mechanical and thermo mechanical processes. Initial period of work tribojoints from positions of structural and energy approach presents the process absorption energy of contact layers, as a result more power-hungry

structure is formed as compared to initial one, but with less energy absorbing ability and higher dissipative properties [3, 4].

1. Theoretical part

Mechanical and chemical an effect most strongly shows up on the stage of the deformation workhardening, when intensive formation of dislocation accumulations in a metal, resulting in the height of thermodynamics and chemical potential, is. In thermodynamic chemical potential is energy that can be absorbed or disengaged because of change the number particles of this kind. Chemical potential plays an especially important role in physics of solid and closely related to conceptions of work output, energy of Fermi (or simply level of Fermi).

Essence of application laws classic thermodynamics to the non-equilibrium systems consists in supposition about a local equilibrium into the small elements areas of the system. An idea about a local equilibrium allows to study large number practically important non-equilibrium systems to that with the complete founding it is possible to take and tribojoints. Thus, all equalizations save the value in relation to small areas and community of the conformities to law described by them. So, equation of Gibbs, showing dependence of internal energy U on entropy S, volume V and chemical potentials μ components of the system consisting of different components, it is possible to write down for a small area in a form [5]

$$dU = TdS - pdV + \Sigma \mu \, dC, \tag{1}$$

where U, S, V pertaining to the small area (local values); C – concentrations of components.

However, there are difficulties at the calculations of local values of internal energy, entropies etc., because these values change depending on the coordinates of area and time.

A level of Fermi essentially is electrochemical potential of electron in a metal. In particular, in a zone theory the relative electrons and holes amount in a semiconductor is characterized by the level of energy of Fermi that makes sense chemical potential of electron in a semiconductor. What higher level of Fermi, the anymore stake of particles bearing a negative charge.

It is set [6, 7], that the coefficient friction of k is proportional to efficiency of destruction of contacts

$$k = C \cdot T \cdot \frac{A}{\mu} \cdot \overline{N}, \tag{2}$$

where A – work (energy) of destruction, T – temperature, μ – chemical potential of metal, $\overline{N}$ – middle number of elementary carriers destruction (is proportional to the number of contacts), C – permanent.

It ensues from equalization, that coefficient of dry friction the less, than anymore chemical potential. For clean metals chemical potential coincides with energy of Fermi. In addition, [8] it is educed, that wear proofness higher at those metals that have a large size of superficial energy, and the power state of surfaces metals suffers a substantial change during their work in the knots of friction. With that, a power (thermodynamics) surface tension is specific work of increase surface at her tension on condition of constancy temperature. In case of dry friction with introduction of coefficient proportion of C_0, for a surface tension an analogical formula is got [6, 7]:

$$\sigma = C_0 \cdot T \cdot \frac{A}{\mu} \cdot \overline{N} . \tag{3}$$

Formula that binds the size of work electron output to superficial energy of metal looks like [9]:

$$\sigma \cong 1{,}15 \cdot 10^3 \left(z \frac{D}{A} \right)^{5/6} \varphi , \tag{4}$$

where σ – superficial energy; z – an amount of valency electrons on an atom; D – density; A – atomic weight; φ – work of output.

However, general lack of mathematical models molecular - mechanical, molecular, atomic - molecular and other theories consists of that they do not take into account structural changes and related to this change of mechanical, physical, chemical, and other properties of superficial layer, influencing on tribotechnical

descriptions of pair friction. Experimental data allow to suppose that accordance is between in size WEO and by the structure of superficial layer of metal, which characterizes the mode of friction set for these conditions. In the process of treatment surface details and at friction superficial layers change the structure and properties. These changes affect size of WEO as most structure - sensitive parameter [10], characterizing the level of superficial energy of solid.

In addition, to works of electron output the features of roughness surface influence substantially. As the preliminary conducted researches showed [11-13], complication of dynamics loading in tribojoints is characterized by the decline of roughness equilibrium. At a two - dimensional (blow with slipping) and three - dimensional loading (blow and slipping in two mutually perpendicular directions) with the increase of amplitude of the transversal slipping a from 0 to 0,2 mm grows by volume intensity of wear and the roughness of surface goes down, her homogeneity rises. The presence of the transversal slipping at a three - dimensional ladening results in formation of surface of less roughness without obvious longitudinal scratches of with a augmentation value WEO.

Taking into account the change of WEO by the friction of superficial layer with different structural state of and roughness equilibrium, we get the size of work destruction tribojoints:

$$A = C \cdot \varphi \cdot \gamma \cdot \frac{k}{T \cdot R \cdot \overline{\overline{N}}}, \tag{5}$$

where φ – works of electron output, γ – structure-sensitive coefficient, R – roughness of surface.

The set correlation between works of electron output, structural state of superficial layer, roughness and wearproofness of surface allows to offer the method of determination wearproofness steels and alloys. Because intensity of wear steels and alloys substantially changes depending on the terms of friction, determination of their wearproofness it maybe to conduct on the state a superficial layer. Thus, to produce the estimation of structural homogeneity of superficial layer on the change of size or distribution of WEO on the surface of details.

2. Experimental part

The state of the real surface of metals is related to forming on the surface of electric dipole moments that determine the size of electrostatic barrier in-process electron output. Because of the heterogeneous state of metallic surface, there is corresponding relief of electrostatic barrier that predetermines divergence works of electron output for the different areas of surface. Thus, for this surface of metal there are characteristic power relief and distribution of WEO on a surface. Comparison power relief of standard material with relief of material that is tested gives an opportunity to estimate the change of the structural state of superficial layer. Thus, as such material can be used the standard of the investigated steel or alloy with known wearproofness, state of superficial layer and conditions of loading in tribojoints. By the change of the structural state of superficial layer it's possible to determine wearproofness.

In particular, the terms of difficult dynamic loading in tribojoints result in formation of the certain structural state of superficial layer of details and level of his wearproofness. Tests of the friction unit model are not always possible due to the duration of the tests and the high cost of carrying out a full-cycle experiment. The required amount of information on wear resistance can be obtained in a shorter time in the methods of accelerated tests of friction pairs. Obviously, the test method for simulating full-scale conditions on a dynamic stand may be the most acceptable.

Techniques and a number of special instruments that allow the implementation of complex contact loading and test specimens in conditions close to full - scale were developed. Realization of the offered method of estimation wearproofness tribojoints we will consider on a concrete example with the use of standards 60S2A (XC60 - AFNOR) and alloy of KhTN-61(Standard of Ukraine), by the friction with a two-dimensional and three-dimensional loading on the special setting on the methodology presented in work [14-15]. The samples were plates 2 mm thick, 14 mm wide and 30 mm long. Friction of the end face of flat samples made it possible to provide constant contact conditions during tests with various dynamic loads. The volume of the worn-out material of the samples was determined through linear wear and the contact area.

Testing terms: amplitude of the transversal slipping a from 0 to 0,2 mm; amplitude of the longitudinal slipping is a 0,1 mm; frequency of the transversal slipping is 30 Hertzs; frequency of the longitudinal slipping is 66 Hertzs; normal loading 20 H, time of tests to 4 hours. The results of tests are presented in a table 1. Measuring works of electron output was conducted with the use of method dynamic condenser of

Kelvin, in that measuring of WEO is carried out on the difference of potentials, which arises up between a measureable surface and surface of electrode – standard [1].

Table 1. Results of tests at a two-dimensional and three-dimensional loading

Material of standard	A_{trs}, mm	V, mm^3	R_z, μm	R_{max}, μm	L, m	$I_v \cdot 10^{-3}$, mm^3/m
KhTN-61	0	0.041	6.5	11.0	960	0.04
	0.01	0.099	10.0	26.0	1164	0.09
	0.05	0.139	8.5	16.0	1368	0.10
	0.10	0.112	8.0	11.0	1056	0.11
60S2A	0	0.052	3.0	9.7	1920	0.03
	0.03	0.090	5.0	9.5	2496	0.04
	0.06	0.033	3.0	4.0	1104	0.05
	0.08	0.071	1.0	1.5	1920	0.05

Note: A_{trs} – amplitude of the transversal slipping; R_{max}, R_z – parameters of roughness; V – volume wear; L – way of friction; I_v – volume intensity of wear.

Thus, a measureable standard and electrode - standard form a flat condenser and does not contact inter se, but here possible is an effective exchange by electrons under the action difference works of electron output of the used metals. Between the surface of standard and electrode due to the pin difference of potentials the variable electric field is formed. Measuring of tension indemnification of this field allows to define difference of potentials between a standard and electrode, to obtain information about the state of layer of sub nanosize thickness.

Frequency of vibrations of electrode-standard from gold made 500 Hertzs, diameter 1,4 mm. Determined distribution WEO a scan-out with a step a 0,2 mm on one line in the center of working surface of standards within 1 meV. Standards before measuring wiped an alcohol and maintained during twenty-four hours to establishment thermodynamics of the equilibrium state of surface. The got distribution works of electron output is presented on Figure 1 and 2.
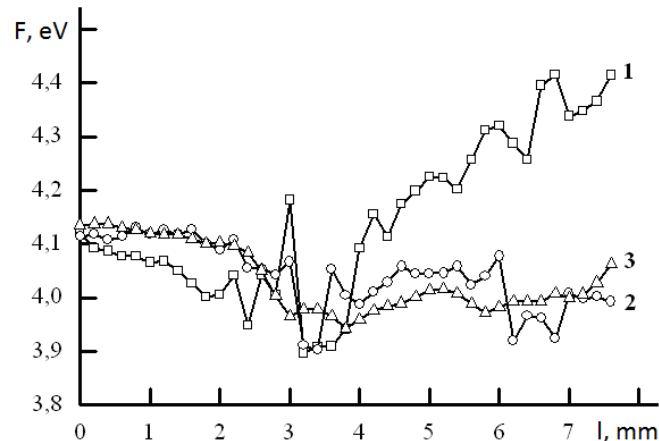
Fig.1. Distribution works of electron output along the surface of standards from the steel KhTN-61 after a wear with different amplitude of the transversal slipping: (*1*) $A_{trs} = 0$ mm; (*2*) $A_{trs} = 0.05$ mm; (*3*) $A_{trs} = 0,1$ mm.

As follows from a Figure 1, state of superficial layer standards alloy of KhTN-61 before the friction approximately identical and WEO is determined about 4.1 eV. As a result of friction with different amplitude of the transversal slipping the state of superficial layer standards changed. A friction with a two-dimensional loading ($A_{trs} = 0$) results in the receipt of superficial layer with enhanceable and large variation of WEO from 3.90 to 4.40 eV. It is possible to suppose that the new structural state of surface, near to amorphous, attended with the increase of WEO, is.

A presence and increase amplitude of the transversal slipping result in diminishing of size and variation of WEO. At tests on a friction with $A_{trs} = 0,05$ mm of WEO droningly diminishes from 4.10 to 4.00 eV, variation in the values of WEO here makes the interval of 3.90…4.10 eV. Superficial layer of standards after a friction with a three-component loading with $A_{trs} = 0,1$ mm provides WEO from 3.95 to 4.05 eV. The

increase amplitude of the transversal slipping results in diminishing dispersion of WEO specifies on the increase homogeneity of the structural state superficial layer, which is accompanied by the decline of wearproofness.
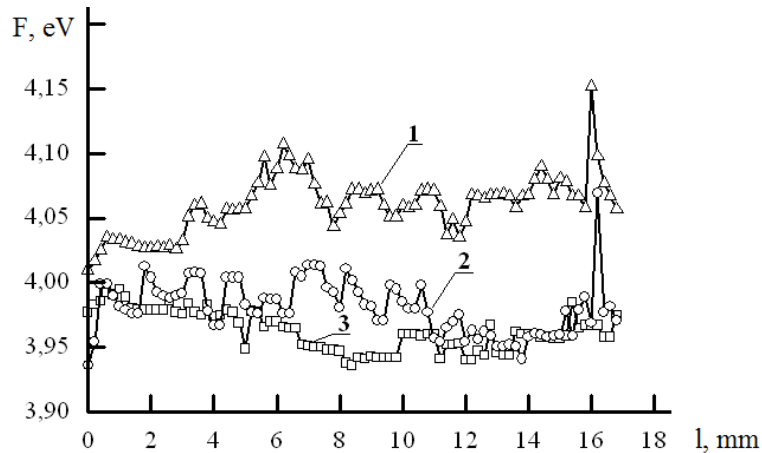
Fig.2. Distribution works of electron output along the surface of standards from the steel 60S2A after a wear with different amplitude of the transversal slipping: (*1*) $A_{trs} = 0$ mm; (*2*) $A_{trs} = 0.06$ mm; (*3*) $A_{trs} = 0,2$ mm.

Analogical results were got for standards from steel of brand of 60S2A (see Figure 2). Enhanceable by volume intensity of wear is marked at presence of the transversal slipping and characterized by the increase of homogeneity superficial layer, decline size of WEO.

Decline of WEO at the increase amplitude of the transversal slipping it is possible to explain as follows. At tests on a friction under act of external variables tensions takes place origins of dislocations that move in the systems of skidding. Part from them outcrops metal and dislocation steps appear. It is known that these steps carry an electric charge and, consequently, form electric doublets. The increase of amount doublets distributions results in diminishing of WEO and decline wearproofness of the investigated surfaces. In the deformed material at a difficult dynamic loading a basic role is played by interaction of dislocations that appear at the shock loading and as a result of cyclic deformation. It results in difficulty of plastic deformation and conditions are created for the facilitation of origin of fragile crack.

Conclusions

Presently plenty of different technological methods to increase resource and reliability of work parts of machines are used in practice. However, their application is not always possible. Most often, the expected efficiency is not ensured due to the lack of formation of optimal parameters of the surface layer during the manufacture or operation of parts.

Work of electron output can be used for research of electronic structure of surface. Deformation of metals at a friction with the different terms of contact results in structural alterations, certain microgeometries of surface, and accordingly to the change of power relief of surface. Comparing initial power relief before deformation with relief after deformation it is possible to define areas surfaces that got different degree of plastic deformation.

Expansion of practical application of results estimation size of WEO domain maybe by control of wearproofness tribojoints, which exploited in the conditions of difficult dynamic loading with the presence of vibrations operating in different directions. Possibility to promote efficiency appears of estimation wearproofness with to confront the change of the structural state of superficial layer of details tribojoints.

This makes it possible to purposefully develop (or choose from among the existing ones) highly efficient structural and technological methods of increasing the performance of parts in extreme conditions, to create designs of new friction devices and significantly reduce the time of their production.

In this case, it is possible to derive and analyze the friction and wear characteristics of a pair's materials, evaluate friction pairs by comparison, and physically model the processes in actual tribocouplings.

Our further work will consist in the development of a technique for measuring the WEO on the surface of machine parts.

REFERENCES

1. Makeeva O.V., Oleshko V.S., Fedorov A.V., Yurov V.M. Development of a device for determining work electron output. *Eurasian Physical Technical Journal*. 2020. No.1, pp. 127 – 131.

2. Yurov V.M., Oleshko V.S. The impact of the environment on the contact potential difference of metal machine parts. *Eurasian Physical Technical Journal*. 2019. Vol. 16, No.1 (31), pp. 99 – 108.

3. Kim V.A. *Self organization of is in the processes work - hardening, friction and wears of toolpiece*. Vladivostok, Dalscience, 2001, 203 p. [in Russian]

4. Shejko S., Sukhomlin G., Mishchenko V., Shalomeev V., Tretiak V. Formation of the Grain Boundary Structure of Low-Alloyed Steels in the Process of Plastic Deformation. *Materials Science and Technology Conference and Exhibition, MS and T,* 2018, Part 1, pp. 746 – 753.

5. Mashkov Yu. T. *Tribophysicist of metals and polymers*. Omsk, OmGTU, 2013, 240 p. [in Russian]

6. Eremin E.N., Yurov V.M., Guchenko S.A. Wear resistance and tribological properties of high entropy coatings CrNiTiZrCu. *Eurasian Physical Technical Journal*. 2020. No.1, pp. 13 – 18.

7. Yurov V.M., Laurinas V.Ch., Gurchenko S.A., Vertyagina E.N., Zavatskaya O.N. *Structure and properties of multiphase ion-plasma coverages*. Karaganda, 2012, 148 p [in Russian]

8. Markov A.A. Change work of electron output at a friction. *Electric phenomena at a friction, cutting and greasing of hard tel*. 1973. pp. 28-34. [in Russian]

9. Zadumkin S.N., Egiev V.G. Work of output and superficial energy of metals. *Physicist of metals and physical metallurgy*. 1966**.** Vol. 1, No 2, pp. 121-122. [in Russian]

10. Shpenkov G.P. *Physikochemistry of friction*, Minsk, BGU, 1978, 208p. [in Russian]

11. Tsyganov V., Ivschenko L., Byalik H., Mokhnach R., Sakhniuk N. Creation of wearproof eutecticum composition materials for the details of the high temperature dynamic systems. *MS and T 2019 - Materials Science and Technolog*. 2019. pp. 450-456.

12. Tsyganov V., Naumik V., Ivschenko L., Byalik H., Mokhnach R. Steel-copper nano composited materials. *MS and T 2019 - Materials Science and Technology*. 2019. pp. 439-443.

13. Tsyganov V.V., Mokhnach R.E., Sheiko S.P. Increasing Wear Resistance of Steel by Optimizing Structural State of Surface Layer, *Steel in Translation*. 2021. Vol.51, No.2, pp.144-147.

14. Tsyganov V.V., Sheyko S. Features of engineering the wear-resistant surface of parts with the multicomponent dynamic load, *Wear*. 2022. 494-495, 204255.

15. Ivshenko L.I., Tsyganov V.V., Zakiev I.M. Features of the wear of tribolojoints under three-dimensional loading, *Journal of friction and wear*. 2011. Vol. 32, No.1, pp.8–16.

CLUSTER ROUTER BASED ON ECCENTRICITY

Zhanabaev Z.Zh, Akhtanov S.N., Turlykozhayeva D.A.*, Ussipov N.M., Ibraimov M.K.

Department of Solid State Physics and Nonlinear Physics, Al-Farabi Kazakh National University,
Almaty, Kazakhstan, turlykozhayeva.dana@kaznu.kz

In this paper, a cluster router based on eccentricity was worked out, related to the field of telecommunications, especially, to the field of message transmission. Messages in this router are transmitted as packets along the route specified in it between devices connected to the network. Each node in this network is assigned a unique address, thanks to which routing can be accelerated. Each router forms a routing map, thanks to the calculated eccentricity of nodes, with which the physical route of the packet is selected at the logical address of the cluster. In addition, the routing map is stored in the register and non-volatile memory of the device to prevent information loss. To analyze this cluster device, a fractal analysis of the UV-flower model network was carried out and the information dimensions of Tsallis and Renyi were calculated.

Keywords: cluster router, eccentricity, complex networks, box covering algorithms, Tsallis and Renyi dimensions.

Introduction

With the development of Internet technology and telecommunications, research is being actively carried out in the field of routing complex networks, which raises the question of developing effective routers [1-2]. In addition, the number of mobile device users is growing, which complicates the network and routing between subscribers. In addition, a large increase in traffic is observed in complex networks such as the Internet [3], as well as in various social networks. It is known that complex networks form a large number of links between subscriber nodes that cover a large physical area. Energy efficiency optimization and fast routing are among the most intelligent and relevant tasks today [4,5].

Routing protocols play an important role in the life and power consumption of sensor nodes. Since each node is powered by a battery and has a limited resource. An optimized routing protocol saves these node resources [6, 7]. There are many routing protocols for a wireless sensor network [8, 9]. The main ones are (1) flat [10], (2) location based [11] and (3) hierarchical [12]. With flat routing, each sensor node interacts with each other. Location-based routing information is only transmitted in a specific area. Particular attention is paid to routing protocols of a hierarchical type, which provide the best results in terms of energy efficiency, throughput and routing [4].

Cluster routing protocols divide a network into several clusters by determining the network eccentricity. Each cluster consists of one main cluster node and several nodes. Each node collects information and forwards it to the main node. Further, data is sent from the main node to the central pre-determined station. These operations are performed in order to cover the network with a minimum number of cells. To solve these problems, it is necessary to use box-covering algorithms, such as CIEA, MEMB, GC, etc. [13-18]. These algorithms are used to calculate the fractal dimension of large-scale networks by covering the network with the minimum possible number of network cells. The minimum number of cells allows you to use base stations less and find the shortest paths to nodes or cells faster. After the network has been covered by various algorithms, we analyzed this cluster router by calculating different information dimensions of the routing map [19, 20].

The classical dimension is fractal dimension that mainly focuses on the relationship between the number and the size of boxes. However, fractal dimension does not consider the information inside the box. To review the information in each box Wei at al. proposed a classical information dimension, where boxes with a large number of nodes have a maximum impact on the information dimension. However, in some cases, the boxes containing a small number of nodes are significant in the network. And moreover, classical information dimension cannot decide which box has greater influence on the fractal property. Considering these cases, Zhang et al. proposed the Tsallis information dimension based on Tsallis entropy [21, 22]. This is because entropy can focus on different information within the box. The Tsallis entropy is one of the

general forms of the Shannon entropy [23, 24], which is controlled by the parameter q. It should be noted that Tsallis entropy is currently used in many areas of human activity, for example, in the analysis of medical images, stellar polytropes, community detection and physics of the cardiovascular system. Closely related to Tsallis entropy is the Renyi entropy, which is considered as the non-extensive statistical mechanics. Based on Renyi entropy, Renyi information dimension was proposed by Duan et al. In Renyi information dimension, the presence of the parameter α makes the proposed method more flexible and expands the possibilities of its use in many areas. For example, we can realize the importance of Renyi entropy in ecology and statistics as index of diversity. In addition, the Renyi entropy is important in quantum information, where it is used as a measure of entanglement.

In this work we proposed a new cluster router based on CIEA, which can divide the network into clusters. Then we calculated the Renyi and Tsallis information dimensions by partitioning the network into boxes. The use of various box covering algorithms for calculating the information dimension has been insufficiently explored in scientific sources. In addition, the CIEA has not previously been used in the calculations of the Renyi and Tsallis information dimensions [25-27].

1. Cluster router based on eccentricity

The cluster router based on eccentricity is equipped with a controller with a switching matrix, bidirectional ports for connection to a control machine and a programmable logic integrated circuit (FPGA) with non-volatile memory, made with the possibility of routing through multiple subnets. Figure 1 shows a block diagram of a cluster router. The cluster router contains a controller with a switching matrix 1, bidirectional ports 2 for connection to a control automaton 3 and a programmable logic integrated circuit (FPGA) 4 with non-volatile memory 5.
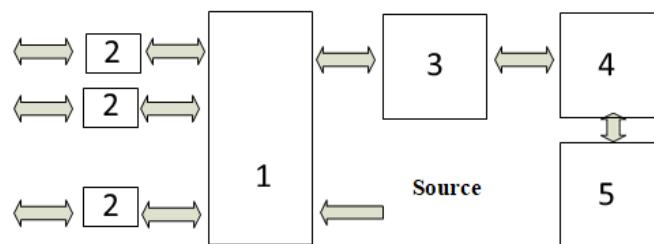
Fig. 1. Block diagram of cluster routing based on eccentricity.

Well-known routers build a route across the entire network and are based mainly on Dijkstra's algorithm. However, these routers are not effective because they contain a large number of network nodes. In contrast, a cluster router divides the network into clusters by calculating the eccentricity, which reduces the number of operations to find the shortest path in the network topology.

To describe a clustered router, we denote the network cluster size as l_b and the cluster radius as r_b, where $l_b = 2r_b+1$. And G is a network (Figure 2) containing a set of nodes $N = \{1, 2, ..., n\}$ and edges $E = \{1, 2, ..., m\}$, in which the distances between routers must be strictly less than l_b.
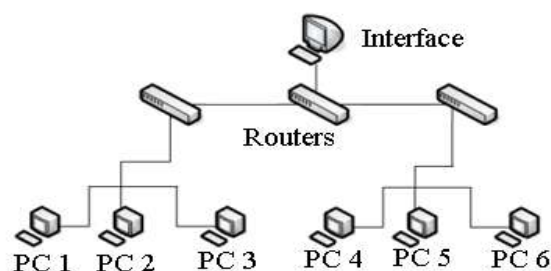
Fig. 2. Network topology example.

Next, we determine the eccentricity $e(v)$ of the nodes v of the connected network G by the formula:

$$e(V) = max\{d(v, u|u \in V(G)\}$$ (1)

The eccentricity $e(v)$ of node v in the connected network G is the maximum distance between nodes u and v. Thus, the eccentricity of the network is the maximum distance between network nodes [28].

Further in the figure. 3 we present an implementation for dividing the network into clusters using network eccentricity. For example, the network includes 13 nodes and 12 edges, as shown in Figure 3.
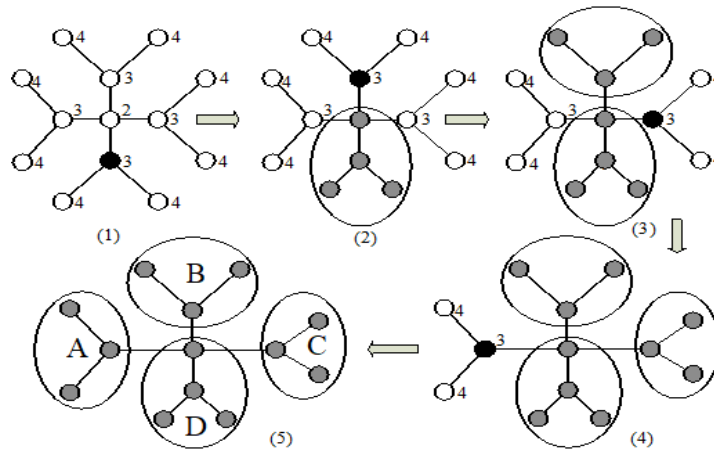
Fig. 3. Division of the network G into clusters (A, B, C, D) based on eccentricity (r_b=1). White nodes are uncovered nodes, gray nodes are covered, black nodes are centers. Numbers nodes indicate eccentricities.

At the first stage, we find the eccentricity $e(v)$ of the nodes and the central node. As the central node, we choose the node located at a distance r_b from the node with the maximum eccentricity. At the second stage, nodes located at a distance r_b from the central node are covered by one cluster with the central node. In the next steps, we continue operations as in the previous steps until the entire network is covered. After the entire network is covered with clusters with radius r_b, the shortest path between clusters is first determined (Figure 4), and then between nodes (Figure 5).

After the entire network is covered with clusters with radius r_b, the shortest path between clusters is first determined (Figure 4), and then between nodes (Figure 5). The cluster routing process includes the following phases: first, we need to find the shortest path from node 1 to node 2 (Figure 5). To do this, the network is divided into four clusters (A, B, C, D) using the cluster routing algorithm, and the nodes in each cluster are covered with lines.
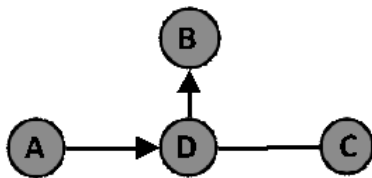
Fig. 4. The shortest path between clusters of the network from FIG.
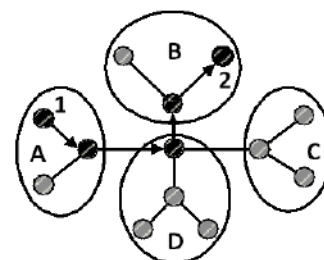
Fig. 5. Illustration of the global shortest path with r_b=1.

Second, we represent each cell as a single node. If there is an edge between two nodes in two different cells, we consider these two cells to be connected. The network shown in fig. 4 consists of four different blocks formed by the network shown in fig. 3. It is obvious that the size of the network has decreased significantly. Thirdly, we find the shortest path between nodes 1 and 2 (arrows) as shown in Fig. 5.

Thus, the number of operations performed to find the shortest path between nodes is reduced. All of the above operation for the compilation of cluster routing is carried out on the FPGA 5 (Fig. 1).

2. Entropy and the Renyi, Tsallis information dimensions of cluster router

To calculate the uncertainty of a probability distribution, Shannon first proposed the concept of Shannon's entropy. In modern communication theory the Shannon entropy has become one of the best known measures of uncertainty, and it is used mainly to describe uncertainty relations and predictions of quantum mechanics. The Shannon entropy [23] is determined by the following formula:

$$H(X) = \sum_{k}^{n} p_k \log_2 \frac{1}{p_k}, \tag{2}$$

where $X = (p_1, p_2, \quad p_k)$ is finite discrete probability distribution, which means $p_k \geq 0 \ (k = 1, 2 \dots .. n)$ и $\sum_{k=1}^{n} p_k = 1$.

With the development of information theory, the Shannon entropy in some cases may not meet all the requirements for application in various fields. To further apply entropy and other options for calculating the uncertainty of a generalized distribution, Alfred Renyi introduced a new entropy inspired by Shannon's entropy. The Renyi entropy is a family of entropies that can be used in special cases by changing the parameter α. This entropy also can preserve additivity. The Renyi entropy [18] of order α is defined as:

$$(X) = \frac{1}{1-\alpha} \log \sum_{k=1}^{n} p_k{}^{\alpha}. \tag{3}$$

For $\alpha \in (0, 1) \cup (1, \infty)$ and the corresponding limit for $\alpha \in \{0, 1, \infty\}$. For $\alpha = 1$, the limit of the Renyi entropy can correspond to the Shannon entropy; therefore, the Renyi entropy is a generalization of the Shannon entropy. The Tsallis' entropy of order q can be defined as follows:

$$S_q = k \frac{1 - \sum_{i=1}^{N} p_i^q}{q - 1}, \tag{4}$$

where N is the total number of elements in the set of probabilities, and p_i are the corresponding probabilities. When the order of q is 1, the Tsallis entropy corresponds to the Shannon entropy. The order of α in Renyi entropy is usually compared with the order q in the Tsallis' entropy to analyze their stability in rapidly and slowly changing situations [22].

As for the information dimension, it was first used to estimate the information load and measure strange attractors. For the first time, Wei et al. defined an information dimension [26] based on the information entropy and the box covering algorithm. The information contained in a complex network can be defined as follows:

$$I = -\sum_{i=1}^{N_B} p_i \ln p_i, \tag{5}$$

where p_i is the probability of nodes in any box, and can be defined as follows:

$$p_i = \frac{n_i}{n}, \tag{6}$$

where n_i is the number of nodes in any box, and n is the total number of nodes in any network. And the

information dimension of the network can be calculated as follows:

$$d_I = -\lim_{l \to 0} \frac{I}{\log l_B} = \lim_{l \to 0} \frac{\sum_{i=1}^{Nl_B} \frac{n_i(l_B)}{n} \log\left(\frac{n_{i(l_B)}}{n}\right)}{\log l_B}, \tag{7}$$

where l_B is the length of the box needed to cover the network, $\frac{n_i(l_B)}{n}$ is the probability of nodes in any box, and the edge of the box is equal to l_B [20].

The informational dimension of Tsallis was proposed by Zhang [23] to explain the complexity of the structure of networks and to reflect the degree of self-similarity and fractal properties. The Tsallis information dimension can be calculated as follows:

$$d_T = -\lim_{l_B \to 0} \frac{\frac{1-\sum_{i=1}^{N_B} p_i (l_B)^q}{q-1}}{\ln l_B}, \tag{8}$$

According to equation (7), the Tsallis entropy information can be found as follows:

$$l_T = \frac{\sum_{i=1}^{N_B} p_i (l_B)^q - 1}{1-q}, \tag{9}$$

where l_B is the length covering the box and p_i is the probability associated with the box coverage results. q is the limiting parameter of the generalized entropy.

There are many dimensions to describe the complexity and uncertainty of a network, but many of them have fixed formulas and are not flexible. And the Renyi information dimension has a parameter α, which can change and affect the measurement itself. The Renyi dimension is defined as follows:

$$d_R = -\lim_{l_B \to 0} \frac{\frac{1}{1-\alpha} \log \sum_{k=1}^{n} p_k{}^\alpha}{\log l_B}, \tag{10}$$

where l_B is the box size of the box covering algorithm. For $\alpha = 1$, the Renyi dimension corresponds to the information dimension, which is easily proved using the L'Hospital equation. When $\alpha = 0$, the dimension is exactly the classical Hausdorff dimension [26].

3. Calculation of the Renyi and Tsallis information dimensions of for the UV-flower model network

UV-flower is a model network that has a certain structure [24]. In the first generation ($n=1$) we start building a circular graph $U+V$, where U and V are network parameters. In the next generation ($n=2$) we replace each node with two parallel edges U and V. These operations are shown in Figure 6.
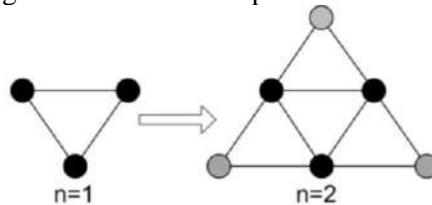
Fig. 6. The first two generations of the UV-flower model network.

In Table 1 below, we present the Renyi and Tsallis information dimensions of the UV-flower model network by dividing this network with different box covering algorithms.

Table 1. Reniy and Tsallis information dimensions of the UV-flower model network

Box covering algorithms	Reniy information dimensions (α=0.5)	Reniy information dimensions (α=2)	Tsallis information dimensions (q=0.5)	Tsallis information dimensions (q=2)
MEMB	1.820	1.674	1.821	1.674
GC	1.823	1.783	1.820	1.798
RS	1.992	1.946	2.042	1.945
CIEA	2.160	2.170	2.158	2.169

The theoretical fractal dimension of the UV-flower network is determined by the following formula:

$$D = \frac{\ln(U+V)}{\ln U}, \quad U > 1 \tag{11}$$

According to formula 10, the theoretical fractal dimension [17] of the UV-flower model network is $D = 2.321$, which can be compared with the experimental data in Table 1 and reveal the most accurate result.

Figure 7 (a, b) below shows the Renyi information dimension for the UV-flower model network, partitioned using the CIEA.
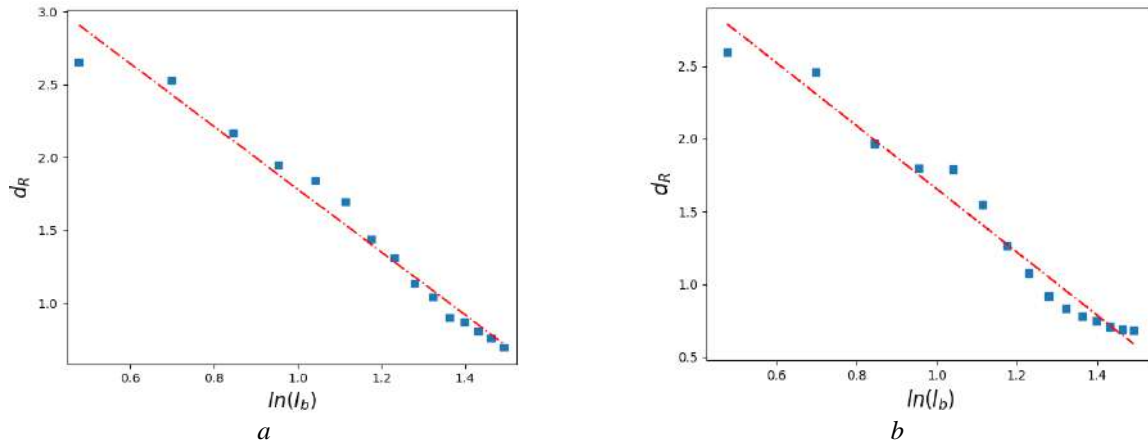
Fig. 7. Renyi dimension (dR = 2.16) when separating the UV-flower network by the CIEA:
a) dR = 2.16, $\alpha = 0.5$; b) - dR = 2.17, $\alpha = 2$.

Figure 8 (a, b) below shows the Tsallis information dimension for the UV-flower model network, partitioned using the CIEA.
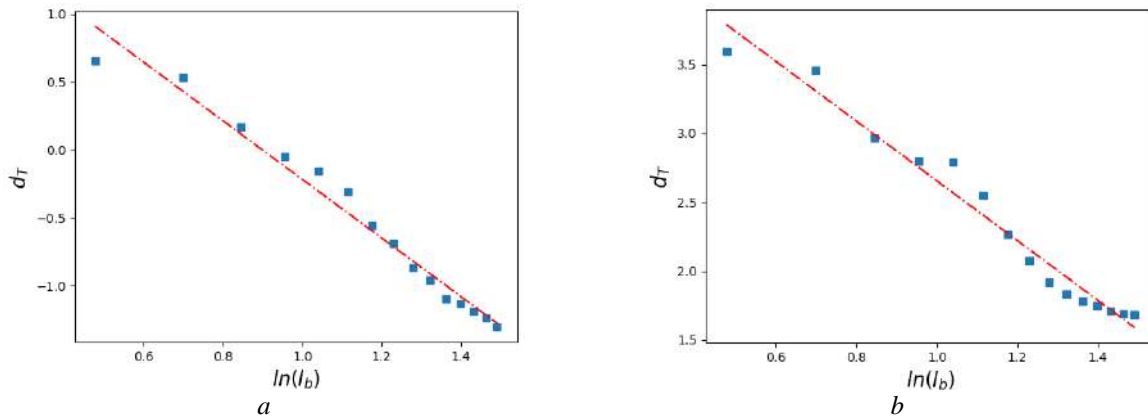
Fig. 8. Tsallis dimension when separating the UV-flower network by CIEA:
a) dT = 2.158, $q = 0.5$; b) dR = 2.16, $q = 2$:

According to Figure 7, 8 the power rule for the cluster size is satisfied, which reflects the fractal property. Since we know that the theoretical dimension of the UV flower model network is 2.32, we get closer value when parameters q and α equal to 2 (dT = 2.169 and dR = 2.17) and slightly less when the parameters equal to 0.5.

Conclusion

In this paper, a cluster router was proposed that performs rapid route construction by clustering the network based on eccentricity, which ensures the autonomy of the device in case of failures. This router, unlike other routers based on the Dijkstra algorithm, builds a route first between clusters and then between network nodes, which allows you to significantly succeed in speed. To analyze this router we calculated the Tsallis and Renyi information dimensions of the UV flower model network using box covering algorithms. The values closest to the theoretical values were obtained when the network was covered by the CIEA and the information dimension of Tsallis was $D_T = 2.158$ (for $q = 0.5$) and $D_T = 2.169$ (for $q = 2$), and the Renyi dimension $D_R = 2.16$ (for $\alpha = 0.5$) and $D_R = 2.17$ (for $\alpha = 2$).

REFERENCES

1   Mazloomi N., Gholipour M., Zaretalab A., Efficient configuration for multi-objective QoS optimization in wireless sensor network. Ad Hoc Networks. 2022, 125 p.

2   Mehbodniya A., Bhatia S., Mashat A., et al. Proportional fairness based energy efficient routing in wireless sensor network. *Computer Systems Science and Engineering*. 2022. Vol. 41(3), pp. 1071-1082.

3   Nasri M., et al. Energy-efficient fuzzy logic-based cross-layer hierarchical routing protocol for wireless internet-of-things sensor networks. *International Journal of Communication Systems*. 2021.Vol.34(9), pp. 4808.

4   Khan M.K., et. al., Hierarchical routing protocols for wireless sensor networks: functional and performance analysis. *Journal of Sensors*. 2021. pp. 1-18.

5   Al-Zubi R. T., et al. Solution for intra/inter-cluster event-reporting problem in cluster-based protocols for wireless sensor networks. International *Journal of Electrical and Computer Engineering*. 2022. Vol. 12(1), pp. 868-879.

6   Daanoune I., Abdennaceur B., Ballouk A. A comprehensive survey on LEACH-based clustering routing protocols in wireless sensor networks. *Ad Hoc Networks*, 2021, Vol.114, pp.102409.

7   Blazevic L., Le Boudec J.Y., Giordano S. A location based routing method for mobile ad hoc networks. *IEEE Transactions on Mobile Computing*. 2005. Vol.4, pp. 97–110.

8   Sarkar A., Murugan T.S., Cluster head selection for energy efficient and delay-less routing in wireless sensor network. *Journal of Wireless Networks*. 2019. Vol. 25, No. 1, pp. 303– 320.

9   Soni V., Mallick D.K. Location-based routing protocols in wireless sensor networks: A survey. *International Journal of Internet Protocol Technology*. 2014. Vol. 8(4), pp. 200 – 213.

10   Huang R., Cui X., Pu H. Wireless sensor network clustering routing protocol based on energy and distance. *Lecture Notes in Electrical Engineering*. 2020. Vol. 675, pp. 1735 – 1745.

11   Song C., et al. How to calculate the fractal dimension of a complex network: the box covering algorithm. *Journal of Statistical Mechanics: Theory and Experiment*. 2007. Vol. 2007, No.03, pp. P03006.

12   Schneider C.M., et al. Box-covering algorithm for fractal dimension of complex networks. *Physical Review E.* 2012. Vol. 86, No.1, pp. 016707.

13   Song C., Havlin S., Makse H.A. Origins of fractality in the growth of complex networks. *Nature physics*. 2006. Vol.2, No.4, pp. 275 – 281.

14   Gallos L.K., Song C., Makse H.A. A review of fractality and self-similarity in complex networks. *Physica A: Statistical Mechanics and its Applications.* 2007. Vol. 386, No.2, pp. 686 – 691.

15   Wen T., Cheong K. H. The fractal dimension of complex networks: A review. *Information Fusion*. 2021. Vol. 73, pp.87 – 102.

16   Akhtanov S. et al. Centre including eccentricity algorithm for complex networks. *Electronics Letters*. 2022. Vol. 58, No. 7, pp. 283 – 285.

17   Kim J.S., et al. Fractality in complex networks: Critical and supercritical skeletons. *Physical Review E.* 2007, Vol.75. No.1, pp. 016110.

18   Long G.U.O., Cai X.U. The fractal dimensions of complex networks. *Chinese Physics Letters*. 2009, Vol.26. No.8, pp. 088901.

19   Zhang Q., et al. Tsallis information dimension of complex networks. *Physica A: Statistical Mechanics and its Applications*. 2015. Vol. 419, pp. 707 – 717.

20   Ramirez-Arellano A., Hernandez-Simon L.M., Bory-Reyes J. A box-covering Tsallis information dimension and non-extensive property of complex networks. *Chaos, Solitons & Fractals*. 2020. Vol.132, pp. 109590.

21   Bromiley P. A., Thacker N. A., Bouhova-Thacker E. Shannon entropy, Renyi entropy, and information. *Statistics and Inf. Series* (2004-004). 2004. Vol. 9, pp. 2 – 8.

22   Zyczkowski K. Renyi extrapolation of Shannon entropy. *Open Systems & Information Dynamics*. 2003. Vol.10, No.03, pp. 297 – 310.

23   Wei D., et al. A new information dimension of complex networks. *Physics Letters A.* 2014. Vol.378, No.16-17, pp.1091 – 1094.

24   Farmer J.D. Information dimension and the probabilistic structure of chaos. *Zeitschrift für Naturforschung A.* 1982. Vol. 37, No.11, pp. 1304 – 1326.

25   Geiger B.C., Koch T. On the information dimension of stochastic processes. *IEEE transactions on information theory*. 2019. Vol.65, No. 10, pp. 6496 – 6518.

26   Barth A., Baumann G., Nonnenmacher T. F. Measuring Renyi dimensions by a modified box algorithm. *Journal of Physics A: Mathematical and General*. 1992. Vol. 25, No.2, pp. 381.

27   Zhang Q. et al. Tsallis information dimension of complex networks. *Physica A: Statistical Mechanics and its Applications*. 2015. Vol. 419, pp. 707 – 717.

28   Duan S., Wen T., Jiang W. A new information dimension of complex network based on Rényi entropy. *Physica A: Statistical Mechanics and its Applications*. 2019. Vol.516, pp. 529 – 542.

FOCUS CPM SOFTWARE FOR TRAJECTORY ANALYSIS OF REAL AXIALLY SYMMETRIC ELECTROSTATIC MIRRORS: METHODS AND ALGORITHMS

Sautbekova Z.S.[1], Trubitsyn A.A.[2*]

[1] Al-Farabi Kazakh National University, Almaty, Kazakhstan
[2] Ryazan State Radio Engineering University named after V.F. Utkin, Ryazan, Russia, assur@bk.ru

The problem of studying the influence of electron mirrors design features, in particular, the gaps between the electrodes on their electron-optical characteristics is solved. A method to solve the problem that combines the advantages of analytical paraxial and numerical approaches is described. FOCUS CPM software developed by the authors of the work that implements the method described is presented. Calculation accuracy is estimated using the example of a three-electrode mirror. A focus position as a function of gap width between cylindrical electrodes is calculated and analyzed.

Introduction

A theoretical basis for modern analytical instrumentation is electron optics. The success in the use of mathematical tools to design precision electron- and ion-optical systems is reflected in the achievement of record-breaking parameters of diagnostic equipment: mass spectrometers, electron spectrometers, electron microscopes, micro-computer X-ray tomographs, etc.

Two approaches in modeling systems of electronic and ion optics are widely used: numerical and analytical. A numerical approach makes it possible to carry out a high-precision analysis of system parameters with almost arbitrary configuration of electrodes. Complex real systems are studied with high accuracy by numerical methods. SIMION [1], CPO [2], FOCUS [3] and other software for numerical-solution of electron optics problems are known and widely used in practice. In contrast to solving problems of analysis, the possibilities of synthesizing new designs by numerical methods are severely limited. Synthesis problems are effectively solved using the mathematical apparatus of classical paraxial electron optics.

One of the areas in mass spectrometry of matter is associated with the development of multielectrode mirrors [4], which have unique focusing properties in temporal and spatial domains. The designs of such mirrors are successfully developed using the analytical methods of paraxial optics [5]. But since an analytical expression of potential distribution function is used when designing systems in paraxial approximation, some important issues remain unresolved. Firstly, these are uncontrolled errors in calculating output electron-optical characteristics of real (not idealized) electron mirrors, secondly, the impossibility of taking into account the influence of edge fields, and thirdly, fundamental restrictions on design complexity.

The aim of this work is to combine the advantages of numerical and analytical approaches to the design of electronic mirror schemes. The technique presented here uses the unique analytical approach developed earlier by the authors [5] to the synthesis and optimization of electron-optical parameters of mirrors, but already under conditions of high-precision numerical simulation of electrostatic field. Along with the development of a technique for synthesizing electron mirror schemes, the practical problem of developing a ready-made tool for such synthesis, FOCUS CPM software, is solved.

1. Analytical modeling of paraxial mirrors

The essence of analytical approach in the modeling of electron lenses, mirrors, etc. is to find partial solutions to the basic equation of paraxial optics. Knowing the partial solutions of the equation is the clue to calculating all electron-optical characteristics of the simulated system. In particular, cognition of particular

solutions makes it possible to construct a general solution (the trajectory of central particle), to define cardinal elements of an electron-optical system, and so on.

The paraxial equation in the case of axial symmetry has the form

$$\Phi r'' + \frac{1}{2}\Phi' r' + \frac{1}{4}\Phi'' r = 0, \tag{1}$$

where $\Phi = \Phi(z)$ is axial distribution of a potential, and the primes denote differentiation with respect to z. Equation (1) is an ordinary linear differential equation of the second order, therefore, it has two linearly independent partial solutions $p=p(z)$ and $g=g(z)$, which form a fundamental system of solutions, the linear combination of which allows us to find a general solution (trajectory equation)

$$r(z) = ap(z) \pm bg(z), \tag{2}$$

where a and b are arbitrary constants determined from the initial conditions in the initial (subject) plane $z=z_0$:

$$a = -\frac{2\sqrt{\Phi_0}}{\Phi_u'}(g_0 r_0' - g_0' r_0),$$

$$\tag{3}$$

$$b = \frac{2\sqrt{\Phi_0}}{\Phi_u'}(p_0 r_0' - p_0' r_0),$$

and indices "0" and "u" mark functions values in the plane $z=z_0$ and in the turning plane $z=z_u$, for which $\Phi(z_u)=0$ and $\Phi'(z_u)\neq0$. In formula (2), sign "+" refers to a direct path branch, and sign "-" refers to a reverse one.

As for the fundamental system of solutions, one of the solutions $p=p(z)$ is an analytic function that satisfies equation (1), which we rewrite as

$$\Phi p'' + \frac{1}{2}\Phi' p' + \frac{1}{4}\Phi'' p = 0, \tag{4}$$

and the solution g=g(z) can be represented as [5]

$$g(z) = \sqrt{\Phi(z)}q(z), \tag{5}$$

where $q=q(z)$ is an analytic function that satisfies the equation

$$\Phi q'' + \frac{3}{2}\Phi' q' + \frac{3}{4}\Phi'' q = 0. \tag{6}$$

In the case of electronic mirrors, the functions $p=p(z)$ and $q=q(z)$ must satisfy the following initial conditions [5]

$$p_u = q_u = 1, p_u' = q_u' = -\frac{\Phi_u''}{2\Phi_u'}. \tag{7}$$

The fulfillment of the following equality for the Wronsky determinant

$$W = \sqrt{\Phi(z)}[p(z)g'(z) - p'(z)g(z)] = \frac{1}{2}\Phi_u' \tag{8}$$

is a guarantee of linear independence of solutions.

Within the framework of the analytical approach, a more or less accurate approximation of electric field axial distribution is used as a function $\Phi(z)$, most often expressed by a combination of elementary mathematical functions.

Formula (2) describes the trajectory of the particle launched from a point with coordinates z_0, r_0 at an angle α_0 $(tan(\alpha_0) = r_0')$ with energy $E_0 = \Phi_0$.

As we have already noted, particular solutions make it possible to find cardinal elements of electron mirror [5]. The position of mirror focus and its focal length are determined by equalities

$$z_F = \frac{1}{2}(z_V + z_C), f = \frac{1}{2}(z_V - z_C), \tag{9}$$

where z_V and z_C are vertex coordinates and center of mirror curvature which can be determined from the following considerations. In case when an object and its image are placed in field-free space, particular solutions $p=p(z)$ and $g=g(z)$ are linear functions and therefore can be written as

$$p = (z - z_C)p', g = (z - z_V)g'. \tag{10}$$

Using the fact that the plane $z=z_0$ is located outside the field, from (10) we obtain the desired values

$$z_C = z_0 - \frac{p_0'}{p_0}, z_V = z_0 - \frac{g_0'}{g_0}. \tag{11}$$

2. Algorithm for Numerical Simulation

Numerical approach to solving the problem under consideration methodologically repeats the abovementioned analytical one. The fundamental difference lies in the fact that the function $\Phi(z_i)$ calculated in the array of nodes z_i by the Boundary Element Method [6] is used here as the axial distribution of the potential $\Phi(z)$. This method of determining $\Phi(z)$ is a guarantee of high simulation accuracy and, most importantly, allows one to study the systems with almost arbitrary electrode configuration. The first $\Phi'(z)$, the second $\Phi''(z)$ and the third $\Phi'''(z)$ (we will need it later) derivatives are also spline approximations of corresponding derivatives found at nodes z_i using numerical differentiation formulas [7]. We should note that in standard approaches to the numerical solution of a field problem, the potential distribution and its gradient must be calculated over the entire working region of an electron-optical system [8, 9].

Another advantage of the approach proposed lies in the fact that the trajectory analysis of simulated systems is based on the numerical solution of paraxial equation (1) and finding particular solutions $p=p(z)$ and $g=g(z)$, which in turn allow us to estimate a wide a set of electron-optical characteristics. Here we note that standard non-paraxial numerical methods represent as a result only particle trajectories in the form of a numerical set of two-dimensional coordinates.

A detailed algorithm for electron mirrors numerical simulation in paraxial approximation is as follows. Having found spline approximations of axial distribution of the potential $\Phi(z)$ we are capable to find turning plane position $z=z_u$ by solving the equation

$$\Phi(z_u)=0. \tag{12}$$

Numerical integration by the Runge-Kutta method of equations (4) and (6), written in the form

$$p'' = f_1(z, p, p'), \tag{13}$$
$$q'' = f_2(z, q, q'), \tag{14}$$

taking into account initial conditions (7) allows finding paraxial equation particular solutions $p(z)$ and $g(z) = \sqrt{\Phi(z)}q(z)$ (see (5)).

Integration is performed from the starting point $z=z_u$ with a negative integration step. In the vicinity of this point $z=z_u$ on the right side of equations (13) and (14) there is a singularity (uncertainty of type 0/0), however, removable. After elimination of the singularity, right-hand sides take the forms

$$f_1(z, p, p') = p'^2(z) - \frac{1}{6}\frac{\Phi'''(z)}{\Phi'(z)}, \ \ z \rightarrow z_u, \tag{15}$$

$$f_2(z, q, q') = \frac{9}{5}\left(q'^2(z) - \frac{1}{6}\frac{\Phi'''(z)}{\Phi'(z)}\right), z \rightarrow z_u. \tag{16}$$

When moving away from the singular point, i.e. when the condition $|z - z_u| > \varepsilon$ is satisfied, regular expressions are used as the right parts (see (4) and (6))

$$f_1(z, p, p') = -\frac{2\Phi'(z)p'(z) + \Phi''(z)p(z)}{4\Phi(z)}, \tag{17}$$

$$f_2(z, q, q') = -\frac{6\Phi'(z)q'(z) + 3\Phi''(z)q(z)}{4\Phi(z)}. \tag{18}$$

Here ε is some small value, which, as calculation practice shows, can be quite large. In numerical integration, it suffices to take one first step, at which right-hand sides are calculated using special formulas (15) and (16). After finding particular solutions, the particle trajectory (2) is constructed as a set of forward and backward branches, and focus position and focal length (9) are determined.

3. "FOCUS CPM" software

FOCUS CPM author's software is designed to simulate axially symmetric electron mirrors with almost arbitrary configuration of electrodes in paraxial approximation. The software consists of several modules (graphic editor, electric field calculation module, trajectory analysis modules), the exchange of information between which is carried out using data files.

3.1 Graphic editor (Design)

Graphics editor module is designed to form the meridional section of electrode system with the supply of appropriate potentials to them. The cross section of each electrode is represented as a closed contour oriented counterclockwise with respect to any of its internal points. At the stage of formation, an electrode can be

formed as a combination of the following elements: straight line segments, arcs of circles, parabolas, hyperbolas, ellipses and splines.

3.2   *Module for calculating potential distribution function (FieldE).*

The module implements the Boundary Element Method (BEM) with the technique developed for calculating singular and quasi-singular integrals [6]. Based on BEM, external Dirichlet problem is solved, which, unlike internal Dirichlet problem, makes it possible to simulate EOS, the designs of which are as close as possible to real ones [8].

The ability to simulate electron-optical systems with the elements of different scales (for example, in case of small gaps between extended electrodes) is another advantage of BEM, in contrast to widely used finite difference methods (FDM) and finite element methods (FEM). In addition, BEM requires no calculation of potentials at all points of a discrete grid covering the simulated area, and allows you to get potential distribution in any subdomain, for example, on the axis of the system.

3.3   *Module for modeling the trajectories of charged particles (PathS).*

The module makes it possible to calculate the set of trajectories of positively charged particles emitted either by a point or by an extended source in a certain range of initial angles (see (2), (3)). Based on the results of calculating the trajectory of a central particle, cardinal elements of electron mirror (9) are calculated.

4 Simulation results

To begin with, the accuracy of path calculations in FOCUS CPM was assessed using the example of modeling the parameters of classical electron lenses with rotational symmetry. It is known [10] that the optical power of weak lenses is represented by an integral of some combination of axial potential distribution function and its derivative. It was noted in [10] that precise calculations are performed with the help of different techniques, also the comparison with the results of numerical simulations show that a given integral expression approximates the optical power of weak lenses with surprisingly good accuracy. The comparison of the results of einzel and immersion lenses optical power calculation using FOCUS CPM software and the integral expression mentioned above showed their guaranteed coincidence within 1%.

One of the ways to significantly increase the resolution of time-of-flight mass spectrometers [11] is the use of electrostatic mirrors of rotational symmetry, e.g., three-electrode ones [5], whose electrodes are coaxial cylinders with equal diameters. In [5], the modes of operation of such mirrors were studied in detail. However, since the authors routinely used an analytical expression of axial potential for an infinitely small gap between cylindrical electrodes, the question for the influence of actual dimensions of these gaps remained open. FOCUS CPM software makes it possible to quantify this impact.

Fig. 1 shows ion-optical scheme of a three-electrode mirror containing all sizes and potentials necessary for modeling. It demonstrates also the picture of electrostatic field equipotentials and a central particle path for "parallel-point" mode of the mirror in case of small but finite gap between the electrodes $\Delta=0.0002d$, where d is the inner diameter of cylinders.
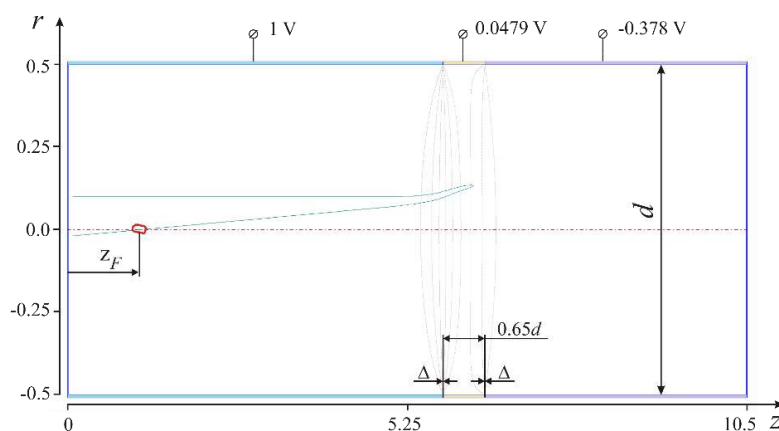
Fig.1. Ion-optical scheme of a three-electrode mirror: results of FOCUS CPM trajectory analysis

Fig. 2 shows the axial distribution of the potential $\Phi(z)$, as well as its first $\Phi'(z)$ and second $\Phi''(z)$ derivatives. The focus position, in accordance with (9), turns out to be equal to $z_F = 1.18d$. The results obtained in FOCUS CPM when modeling mirrors were additionally verified using FOCUS Pro software [3] developed

for numerical analysis of real (not paraxial) EOS/IOS. Once again, we note that in this case it is necessary to calculate the field in the entire working area of EOS and a set of particle trajectories. Fig. 3 shows the results of calculation for 10 particle trajectories in the mirror with $\Delta=0.0002d$ having different radial start coordinates r. Based on the set of trajectories, the position and the order of spatial focus are estimated using a numerical method [12]. The result of the estimate is as follows: a mirror provides second-order focusing in terms of the initial coordinate r at the point $z_F = 1.12d$. To be able to conduct a comparative analysis, the results of calculations of the focus position z_F by different methods are collected in Table 1.
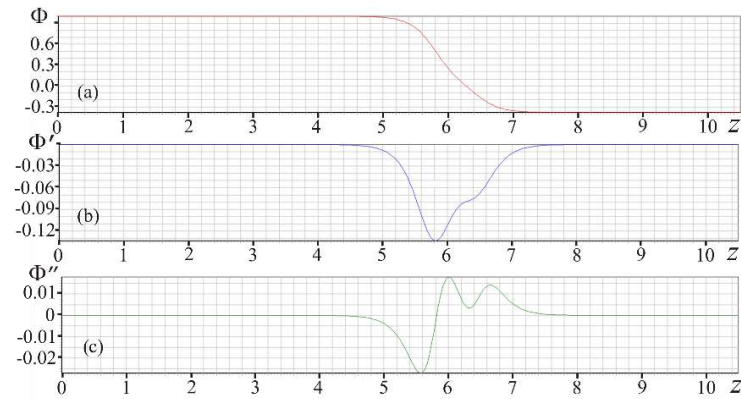
Fig.2. Axial distributions of (a) the potential $\Phi(z)$, (b) the first $\Phi'(z)$ and (c) the second $\Phi''(z)$ derivatives of the potential in a three-electrode mirror
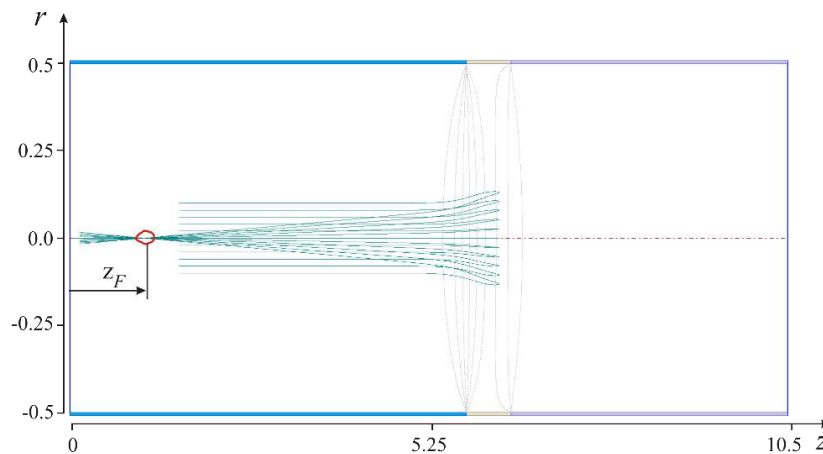
Fig.3. Results of numerical simulation of a three-electrode mirror using FOCUS Pro software in a "parallel-point" mode

Table 1. Focus position z_F

	Method		
	Analytical	FOCUS CPM	FOCUS Pro
Position z_F	1.01d	1.18d	1.12d

An analysis of tabular data allows us to conclude that the error in calculating the parameters of an electron mirror in the case of an analytical expression of the potential [5] is about 10%; while the numerical solution of field problem improves calculation error by about an order of magnitude. At the same time, the time for solving the problem in a paraxial approximation by means of new FOCUS CPM software is reduced by thousands of times compared to the case of using FOCUS Pro numerical simulation software [3]. In terms of its main characteristics (counting speed and accuracy), the FOCUS CPM software presented is ideal for optimizing designs, e.g., electronic mirrors and studying the effect of their geometric features on output electron-optical parameters. Fig. 4 demonstrates the dependence of a focus position z_F on the size of a gap between cylindrical electrodes Δ, which must be taken into account when manufacturing a real device.
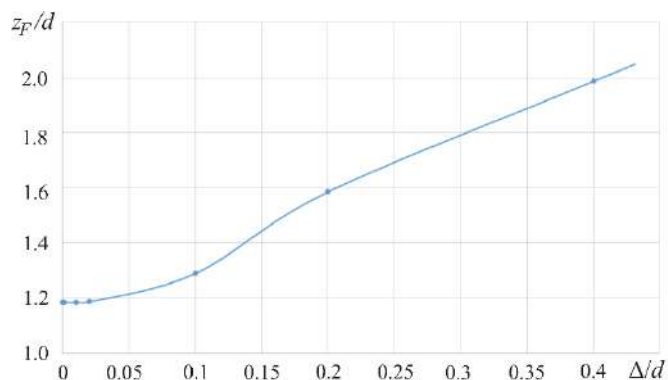
Fig. 4. Dependence of a focus position on the size of a gap between cylindrical electrodes

It follows from the last dependence that in the range of small gaps up to about 5% of d, a focus position is almost constant and approximately doubles with a further increase in the gap to 40% of d.

Conclusion

In this paper for the first time a unique analytical technique for modeling the parameters of multielectrode electron mirrors [5] is combined with an original technique for numerical solution of an external field problem using the Boundary Element Method [6, 8]. The developed approach implemented in the form of FOCUS CPM software application makes it possible to design electron mirrors with a practically arbitrary electrode configuration at a high counting rate. The high accuracy (on the order of a few percent) of the calculations of charged particle trajectories and electron-optical parameters of multielectrode mirrors in FOCUS CPM is established. A practically important dependence of a focus position on the size of a gap between the electrodes is obtained for a three-electrode mirror.

REFERENCES

1   The field and particle trajectory simulator. Industry standard charged particle optics software. Available at: https://simion.com (Apr19, 2022).
2   CPO "BEM" Charged Particle Optics Simulation Software. Available at: https://www.sisweb.com/software/cpo.htm (Apr19, 2022).
3   Trubitsyn A., Grachev E., Gurov V., Bochkov I., Bochkov V. CAE «FOCUS» for Modelling and Simulating Electron Optics Systems: Development and Application. *Proceedings of SPIE*. 2017. Vol. 10250, pp. V-1 – V-7.
4   Berger C. Design of rotationally symmetrical electrostatic mirror for time-of-flight mass spectrometry. *Journal of Applied Physics*. 1983. Vol**.** 54, pp. 3699-3703.
5   Bimurzaev S., Aldiyarov N., Sautbekova Z. High Dispersive Electrostatic Mirrors of Rotational Symmetry with the Third Order Time-of-Flight Focusing by Energy. *Technical Physics*. 2020. Vol. 65, pp. 1150–1155.
6   Trubitsyn A.A. Calculation of the Singular Integrals Arising in the Boundary-Element Method for the Dirichlet Problem. *Comp. Maths Math. Phys.* 1995. Vol.35, No.4, pp. 421-428.
7   Burden R.L., Faires J.D. Numerical Analysis. 7th Ed. USA, Boston: Brooks/Cole, 2000, pp. 174-191.
8   Gurov V.S., Saulebekov A.O., Trubitsyn A.A. Analytical, Approximate-Analytical and Numerical Methods in the Design of Energy Analyzers. In *Advances in Imaging and Electron Physics*. Hawkes, Ed. London: Academic Press, 2015, 209p.
9   Plies E.Electron optics of low-voltage electron beam testing and inspection. Part I: Simulation tools. *Advances in Imaging and Electron Physics*. 2018. Vol. 205, pp. 139 – 267.
10 Yavor M. Optics of Charged Particle Analyzers. In *Advances in Imaging and Electron Physics*. P.W. Hawkes, Ed. London: Academic Press, 2009, 375 p.
11 Mirsaleh-Kohan N., Robertson W. D., Compton R. N. Electron ionization time-of-flight mass spectrometry: Historical review and current applications. *Mass Spectrometry Reviews*. 2020. Vol. 27, No. 3, pp. 237–285.
12 Trubitsyn *A.A.* A Correlation Method of Search for Higher-Order Angular Focusing. *Technical Physics*. 2001. Vol.46, pp. 630-631.

SUMMARIES	ТҮСІНІКТЕМЕЛЕР	АННОТАЦИИ

Смирнов В.Ю., Қадір М.Ф., Алпысбаева Б.Е., Немкаева Р.Р.
Мыс оксиді қабыршақтарының морфологиясына анодтау режимдерінің әсерін зерттеу

Берілген жұмыста бір сатылы электрхимиялық анодтау әдісімен алынған Cu_2O қабыршақтарының беткі морфологиясы туралы тәжірибелік мәліметтер келтірілген. Процесс фосфор қышқылы негізіндегі электролитте 90 секунд бойы 13°C температурада 50В тұрақты потенциалмен жүргізілген. Тәжірибелік жұмыс барысында синтездің оптималды параметрлері анықталды. Мыс кеуекті қабыршақтардың морфологиясы Ntegra Therma (NT-MDT) атомды-күштік микроскопияның көмегімен зерттелген. Тәжірибелік жұмыстардың нәтижелері бойынша анодтау процесінің параметрлеріне байланысты мыс оксидінің кеуек диаметрі бірнеше ондаған нанометрден жүздеген микронға дейін өзгеруі мүмкін екендігі анықталған.
Кілт сөздері: нанокеуекті, мыс оксиді, электрхимиялық анодтау, фосфор қышқылы, атомды-күштік микроскопия.

Смирнов В.Ю., Кадыр М.Ф., Алпысбаева Б.Е., Немкаева Р.Р.
Исследование влияния режимов анодирования пленок оксида меди на их морфологию

В настоящей работе представлены экспериментальные данные по морфологии поверхности пленок Cu_2O, полученных одностадийным электрохимическим анодированием. Процесс проводили при постоянном приложенном потенциале 50В и температуре 13°C (90 секунд) в электролите на основе фосфорной кислоты. В ходе экспериментальной работы были определены оптимальные параметры синтеза. Морфологию пористых пленок меди исследовали с помощью атомно-силовой микроскопии Ntegra Therma. Было исследовано влияние основных параметров анодирования на морфологию нанопористой пленки Cu_2O. По результатам экспериментальных работ установлено, что в зависимости от параметров процесса анодирования можно варьировать диаметр пор оксида меди от нескольких десятков нанометров до сотен микрон, при этом также имеется возможность изменения толщины пленки.
Ключевые слова: нанопористый, оксид меди, электрохимическое анодирование, фосфорная кислота, атомно-силовая микроскопия.

Шишулин А. В., Потапов А. А., Шишулина А. В.
ФРАКТАЛДЫ ПІШІНДІ НАНОБӨЛШЕКТЕРДІҢ ЖЫЛУ ӨТКІЗГІШТІК КОЭФФИЦИЕНТІНІҢ ТОРЛЫ ҚҰРАУШЫСЫ ТУРАЛЫ СҰРАҚҚА.

Нанобөлшектерден көлемді наноқұрылымды материалдарды алу үшін аддитивті технологияларды пайдалану тиімді және коммерциялық қол жетімді термоэлектрлік энергия түрлендіргіштерін құрудың ең перспективті бағыттарының бірі болып табылады. Наноқұрылымдау термоэлектрлік материалды анықтайтын тасымалдау қасиеттерін іріктеп өзгертуге мүмкіндік береді. Берілген жұмыста кристалдық тордың тербелістер үлесінің (іс жүзінде оны азайту қажет) таза зат нанобөлшегінің жылу өткізгіштік коэффициентіне оның морфологиясына айтарлықтай тәуелділігінен тұратын тағы бір әсер ұсынылып көрсетілген. Нанобөлшектің морфологиясы оның тиімді диаметрінің, фракталдық өлшемінің және бетінің кедір-бұдырының шамаларымен берілген. Төмен температурадағы таза висмут нанобөлшектерінің мысалында бөлшек морфологиясының "күрделенуімен" тордың жылу өткізгіштігінің айтарлықтай төмендеуі көрсетілген. Жұмыстың қорытқы бөлімінде нанобөлшектер ансамбльдерінің бірқатар сипаттамаларын есептеу әдістері ұсынылған, сонымен қатар фракталды өлшемді эксперименттік анықтау әдістемесі талқыланған.
Кілт сөздері: термоэлектрлік материалдар, жылу өткізгіштік, нанобөлшектер, фонондар, фракталдық өлшемділік.

Шишулин А.В., Потапов А.А., Шишулина А.В.
К ВОПРОСУ О РЕШЕТОЧНОЙ СОСТАВЛЯЮЩЕЙ КОЭФФИЦИЕНТА ТЕПЛОПРОВОДНОСТИ НАНОЧАСТИЦ ФРАКТАЛЬНОЙ ФОРМЫ.

Использование аддитивных технологий для получения объемных наноструктурированных материалов из наночастиц является одним из наиболее перспективных направлений создания эффективных и коммерчески доступных термоэлектрических преобразователей энергии. Наноструктурирование позволяет осуществлять выборочную модификацию транспортных свойств, определяющих термоэлектрическую материала. В настоящей работе представлен еще один эффект, заключающийся в существенной зависимости вклада колебаний кристаллической решетки (практически требуется его уменьшение) в коэффициент теплопроводности наночастицы чистого вещества от ее морфологии. Морфология наночастицы задавалась величинами ее эффективного диаметра, фрактальной размерности и шероховатости поверхности. На примере наночастиц чистого висмута при низких температурах продемонстрировано существенное понижение теплопроводности решетки при «усложнении» морфологии частицы. В заключительной части работы

представлены методы расчета ряда характеристик ансамблей наночастиц, а также обсуждается методика экспериментального определения фрактальной размерности.
Ключевые слова: термоэлектрические материалы, теплопроводность, наночастицы, фононы, фрактальная размерность.

Агельменев М.Е., Братухин С.М., Поликарпов В.В.
ӨЛШЕМДІК ӘСЕРЛЕРДІҢ ГРАФЕН НАНОЛЕНТАЛАРЫНДА ОРНАЛАСҚАН СҰЙЫҚ КРИСТАЛДАРДЫҢ РЕТТІЛІГІНЕ ӘСЕРІ

Графен нанолентасының бетіндегі полярлы нематикалық фенил пропаргил эфирлерінің парахлорфенилдердің тәртібін компьютерлік модельдеу эксперименттері бірқатар заңдылықтарды анықтауға мүмкіндік берді. Графеннің өлшемдері электр өрісі мен температураның әсерінен өзгерген кездегі молекулалардың динамикасы зерттелген. Зерттеу әдісі ретінде сұйық агрегаттық күйді жақындауда молекулалық динамика әдісі қолданылған. Модельдеу атомдық әдіс-тәсілмен жүргізілген. Графен наноленртасы мен электр өрісі биаксиалды күйдегі нематикалық сұйық кристалл молекулаларының өздігінен жиналуын анықтайтыны көрсетілген. Бұл күйлер графен нанолентасының енінің оның ұзындығына қатынасы өзгерген кезде пайда болады. Жарықтану облысында парахлорфенилдердің реттілігі ені мен ұзындығының қатынасы 3: 1 мәні кезінде өсе бастайтыны анықталды.
Кілт сөздері: нематикалық сұйық кристалдар, графен нанолентасы, компьютерлік модельдеу.

Агелменев М.Е., Братухин С.М., Поликарпов В.В.
ВЛИЯНИЕ РАЗМЕРНЫХ ЭФФЕКТОВ НА УПОРЯДОЧЕНИЕ ЖИДКИХ КРИСТАЛЛОВ, РАСПОЛОЖЕННЫХ НА НАНОЛЕНТАХ ГРАФЕНА

Эксперименты по компьютерному моделированию поведения полярных нематических фенилпропаргиловых эфиров парахлорфенилов на поверхности графеновой наноленты позволили выявить ряд закономерностей. Изучается динамика молекул при изменении размеров графена под действием электрического поля и температуры. В качестве метода исследования использовался метод молекулярной динамики в приближении жидкого агрегатного состояния. Моделирование проводилось в атомистическом подходе. Показано, что графеновая нанолента и электрическое поле определяют самосборку молекул нематических жидких кристаллов в биаксиальном состоянии. Эти состояния возникают при изменении отношения ширины графеновой наноленты к ее длине. Установлено, что в области просветления упорядоченность парахлорфенилов начинает возрастать при значении отношения ширины к длине 3:1.
Ключевые слова: нематические жидкие кристаллы, графеновая нанолента, компьютерное моделирование.

Рымжанов Р.А., Волков А.Е., Ибраева А.Д.
Жылдам ауыр иондармен сәулелендіргеннен кейінгі итрий-темір гранатының электрондық кинетикасы

Монте-Карло TREKIS моделі жылдам ауыр иондармен сәулелендіргеннен кейінгі итрий-темір гранаты электрондық жүйешесінің уақыттық кинетикасын зерттеу үшін қолданылды. Зарядталған бөлшектердің нысанамен өзара әрекеттесу қималары күрделі диэлектрлік функцияның формализмі – динамикалық құрылымдық фактор аясында анықталды. Электрондық қозудың кеңістіктік таралуының екі режимі табылды: жылдам дельта электрондар қозудың бастапқы фронтын құрайды, ал тректе пайда болған плазмондардың ыдырауынан пайда болатын электрондар келесі екінші фронтты құрайды. Тордың қызу процестерін талдау барысында ион трегінде пайда болатын валенттік кемтіктердің рекомбинациясы арқылы бөлінетін потенциалдық энергияның басым үлесі анықталды. Моттың қималарымен сипатталатын электрондар мен кемтіктердің серпімді шашырауы тордың артық энергиясының шамалы өсуіне әкеледі, ал күрделі диэлектрлік функцияның формализмі бұл процестердің торды қызуына айтарлықтай үлесін көрсетеді.
Кілт сөздері: жылдам ауыр ион трегі, электрондық қозу, күрделі диэлектрлік функция, иондардың энергия шығыны, Монте-Карло модельдеу.

Рымжанов Р.А., Волков А.Е., Ибраева А.Д.
Электронная кинетика железо-иттриевого граната после облучения быстрыми тяжелыми ионами

Монте-Карло модель TREKIS применялась для изучения временной кинетики электронной подсистемы железо-иттриевого граната после воздействия быстрыми тяжелыми ионами. Сечения взаимодействия заряженных частиц с мишенью определялись в рамках формализма комплексной диэлектрической функции – динамического структурного фактора. Обнаружены два режима пространственного распространения электронного возбуждения: быстрые дельта-электроны формируют первичный фронт возбуждения, а электроны, возникающие за счет распада плазмонов, генерируемых в треке, формируют второй фронт, следующий за первым. Анализ процессов нагрева решетки мишени выявил доминирующий вклад потенциальной энергии, выделяемой за счет рекомбинации валентных дырок, генерируемых в треке иона. Упругое рассеяния электронов и дырок, описываемое сечениями Мотта, приводит лишь к незначительному

увеличению избыточной энергии решетки, в то время как формализм комплексной диэлектрической функции демонстрирует значительный вклад этих процессов в нагрев решетки.

Ключевые слова: трек быстрого тяжелого иона, электронные возбуждения, комплексная диэлектрическая функция, потери энергии ионов, моделирование Монте-Карло.

Матвеев Н.Н., Лисицын В.И., Архипов В.В.
Біртексіз температура өрісіндегі балқыма-кристалл ауысуларында полиэтилен оксидінің поляризациясын анықтаудың конформациялық тәсілі

Қазіргі заманғы технологияларда полиэтилен оксидін (ПЭО) кеңінен қолдануға байланысты жақында оның молекулалық құрылымы мен қасиеттерінің модельдеу әдістерімен байланысын зерттеу жанданды. Әдетте, икемді тізбекті полимерлердің супрамолекулалық құрылымындағы термополяризациялық әсерді модельдеу кезінде сызықтық бір өлшемді кристалдар жиынтығы болып көрінеді. Бұл әдіс-тәсіл аясында полимерлер құрылымының конформациялық ерекшеліктері ескерілмейді. Мақаланы мысал ретінде (ПЭО) полимер молекуласының конформацияларының оның дипольдік моментінің орташа квадратының температураға тәуелділігіне әсерін есептеу әдісі негізделген.

Кілт сөздері: молекулалық конформациялар, икемді тізбекті полимерлер, полиэтилен оксиді, супрамолекулалық құрылым, термиялық поляризация әсері, біртексіз температура өрісі.

Матвеев Н.Н., Лисицын В.И., Архипов В.В.
Конформационный подход к определению поляризованности полиэтеленоксида при переходах расплав-кристалл в неоднородном температурном поле

В связи с широким использованием в современных технологиях полиэтиленок – сида (ПЭО) в последнее время активизировались исследования взаимосвязи его надмолекулярной структуры и свойств методами моделирования. Обычно при моделировании термополяризованного эффекта в надмолекулярной структуре гибкоцепных полимеров представляется набором линейных одномерных кристаллов. В рамках такого подхода не учитываются конформационные особенности строения полимеров. В статье на примере (ПЭО) обосновывается способ расчета влияния конформаций молекулы полимера на зависимость усредненного квадрата дипольного момента его молекул от температуры.

Ключевые слова: конформации молекул, гибкоцепкие полимеры, полиэтиленоксид, надмолекулярная структура, термо-поляризационный эффект, неоднородное температурное поле.

Бердибеков А.Т., Лауринас В.Ч., Доля А.В., Грузин В.В., Гученко С.А., Твардовский А.Н.
Жаңа технология бойынша дайындалған көп элементті нысаналарды пайдалануымен бұйымдар мен құралдардың беттерінің бөліктеріне қорғаныс жабындарын магнетронды тозаңдату

Соңғы уақытта қорғаныс жабындарын алу үшін арналған магнетронды тозаңдатқышты қолдану қарқынды дамуда. Бұл әдісті қолданудың үлкен болашағы - бір мезгілде жоғары температураға, агрессивті орталарға және әртүрлі тозуға ұшырайтын беттерді қорғау үшін қолданылатын жоғары энтропиялы жабындарды қолдану мүмкіндігіне байланысты. Берілген жұмыста, технологиялық тізбегі егжей-тегжейлі сипатталған, магнетронды тозаңдатуға арналған нысаналардың жаңа түрлерін жасау әдісі ұсынылған. Зерттеу жаңалығы бір ғана нысананы пайдалану арқылы көп элементті жабындарды алу мүмкіндігінде жатыр. Бұл нысанадағы әртүрлі элементтердің саны ондаған болуына негізделген. Сондай-ақ, мақалада магнетронды тозаңдату кезінде бес түрлі металды бар нысананы пайдалану арқылы алынған оң нәтиже келтірілген.

Кілт сөздері: магнетронды тозаңдату, қорғаныш жабыны, көп элементті нысаналар.

Бердибеков А.Т., Лауринас В.Ч., Доля А.В., Грузин В.В., Гученко С.А., Твардовский А.Н.
Магнетронное напыление защитных покрытий на детали поверхностей изделий и инструментов с использованием изготовленных по новой технологии многоэлементных мишеней.

В последнее время использование магнетронного напыления для нанесения защитных покрытий интенсивно развивается. Большая перспектива использования этого метода обусловлена за счет возможности нанесении высокоэнтропийных покрытий, которые используются для защиты поверхностей, подвергающих одновременному воздействию повышенных температур, агрессивных сред и различным видам износа. В данной работе предложен способ изготовления новых видов мишеней для магнетронного напыления, с подробно описанной технологической цепочкой их изготовления. Новизна заключается в возможности при использовании одной мишени нанесения многоэлементных покрытий. Это обусловлено тем, что количество различных элементов в мишени может измеряться десятками. Также в работе приведен полученный положительный результат использования при магнетронном напылении мишени, в состав которой входило пять различных металлов.

Ключевые слова: магнетронное напыление, защитное покрытие, многоэлементные мишени.

Солдатхан Д., Амангелді Н., Балтабеков А.С., Ерғалиұлы Ғ.
$^{16}O+^{12}C$ ядролық жүйенің өзара әсерлесу потенциалдарының энергетикалық тәуелділігін жартылай микроскопиялық тәсілімен зерттеу.
Төмен энергияда ауыр иондардың жеңіл ядроларымен соқтығысу процесін зерттеу ядролық физикада, термоядролық энергетикада және астрофизикада маңызды. Кулондық тоскауылға жақын энергияда сипатталған ядролық жүйенің жоғары дәлдік мәндерін термосинтез ішіндегі жеңіл ядролар синтезін басқару үшін қолданады. Күн, плазма және жұлдыздардағы жеңіл ядролар реакциялардын қимасын анықтаған потенциалдармен, параметрлерімен зерттеуге мүмкіндік бар. Мақалада ядро-ядролық өзара әрекеттесу процесін сипаттайтын микроскопиялық тәсілі ұсынылған. Эмпирикалық мәндерін эксперименттік деректерге сәйкестіру негізінде анықтайтын феноменологиялық тәсілде қиманы жақсы сипаттайтын потенциалдармен параметрлер жиынтығын көптеп табуға болады. Бірақ олардың қайсысы шынайы деген сұрақ туындайды. Сондықтан микроскопиялық түрде құрылған фолдинг потенциалдармен оның параметрлерімен қосымша сипаттау қажет. Сол себептен ядролық потенциалдың жорамал бөлігі оптикалық модель негізінде, ал нақты бөлігі екілік фолдинг модельде сипаттайтын жартылай микроскопиялық талдау жасалды. Фолдинг потенциал әсерлесетін нуклондардың матрицалық элементіне негізделген тиімді нуклон-нуклондық өзара әрекеттесу және нуклондардың таралу тығыздығына тәуелді құрылады. Талдау нәтижесінде E_{Lab}=20, 24, 36 МэВ энергияларда $^{16}O+^{12}C$ ядролық жүйенің эксперименттік қималарын жақсы сипаттайтын дифференциалдық қималары және оңтайлы параметрлер анықталды. Нақты микрофолдинг потенциалдар негізінде сипатталған дифференциалдық қималардың нормалау коэффициентері N=0,85-1,0 аралығында анықталды..
Кілт сөздер: серпімді шашырау, фолдинг моделі, материя тығыздығының таралуы, NN өзара әсерлесу.

Солдатхан Д., Амангелды Н., Балтабеков А.С., Ерғалиұлы Ғ.
исследование энергетической зависимости потенциалов взаимодействия ядерной системы $^{16}O+^{12}C$ полу-микроскопическим способом.
Изучение процесса столкновения тяжелых ионов с легкими ядрами при низкой энергии имеет важное значение в ядерной физике, термоядерной энергетике и астрофизике. Высокоточные значения ядерной системы, описанные при энергии, близкой к кулоновскому барьеру, используются для управления синтезом легких ядер в термосинтезе. Сечение реакций легких ядер на солнце, плазме и звездах можно исследовать с помощью определенных нами потенциалов. В статье представлен микроскопический подход, описывающий процесс ядерно-ядерного взаимодействия. В феноменологическом подходе, определяющем эмпирические значения на основе сопоставления с экспериментальными данными, можно найти множество наборов параметров, характеризующих сечение. Но возникает вопрос, какие из них реальны. Поэтому необходимо дополнительно охарактеризовать его параметры микроскопически сформированными потенциалами фолдинга. Отсюда был сделан полу-микроскопический анализ, описывающий мнимую часть потенциала на основе оптической, а реальный часть на основе модели фолдинга. Потенциал фолдинга строится в зависимости от плотности распределения нуклонов и эффективного нуклонно-нуклонного взаимодействия на основе матричного элемента взаимодействующих нуклонов. В результате анализа были определены дифференциальные сечения и оптимальные параметры, хорошо характеризующие экспериментальные сечения ядерной системы $^{16}O+^{12}C$ при энергиях E_{Lab}=20, 24, 36 МэВ. Коэффициенты нормирования дифференциальных сечений, описанные на основе реальных потенциалов микрофолдинга, определялись в пределах N=0,85-1,0.
Ключевые слова: упругое рассеяние, модель фолдинга, распределение плотности материи, взаимодействие NN.

Загерис Г., Геза В., Якович А., Родин Л., Хомко А., Харитонов В., Рогулёва М.
Өнеркәсіптік декабонизацияға арналған модульдік типтегі метанол өндірісінің қондырғылары.
Құрамында көміртегі бар химиялық заттарды өндіру газ шығарындыларындағы көміртегі мөлшерін азайту әдісі болып табылады. Атап айтқанда, метанолды (CH_3OH) қазіргі уақытта алауда жағылатын ілеспе мұнай газынан алуға болады. Метанның парциалдық тотығуы сияқты көмірсутек газын синтез-газына айналдырудың қарапайым әдістерін мұнай-газ кен орындарында тікелей пайдалану үшін шағын модульдік қондырғыларды жасау үшін қолдану маңызды. Химиялық процестердің кинетикасы мен қондырғының құрылысын ескере отырып, парциалды тотығуды сандық модельдеу қарастырылады. Берілген жұмыста табиғи газдың ауамен парциалды тотығуын сипаттайтын бірнеше модельдер құрылды - масса мен энергияның тасымалдау құбылыстарын, сондай-ақ химиялық түрлендірулерді ескеретін тепе-теңдік және толық үш өлшемді модельдер. Модельдерді салыстырудың негізгі қорытындысы - толық сандық модель толық емес тотығуды жақсы болжайды, ал қарапайым тепе-теңдік моделі болжамайды. Болашақта оттегі-метан конверсиясының сандық модельдеу нәтижелері зерттеліп, ұсынылатын болады.
Кілт сөздері: декарбонизация, метанол өндірісінің қондырғылары, химиялық реакцияларды модельдеу, сандық гидродинамика, жану, парциалды тотығу.

Загерис Г., Геза В., Якович А., Родин Л., Хомко А., Харитонов В., Рогулёва М.
Установки производства метанола модульного типа для промышленной декабонизации.

Производство углеродосодержащих химических веществ является способом снижения содержания углерода в газовых выбросах. В частности, метанол (CH_3OH) можно получать из попутного нефтяного газа, который в настоящее время сжигается в факелах. Простые методы конверсии углеводородного газа в синтез-газ, такие как парциальное окисление метана, имеет смысл использовать для создания небольших модульных установок для непосредственной эксплуатации на нефтегазовых месторождениях. Рассматривается численное моделирование парциального окисления с учетом кинетики химических процессов и конструкции оборудования. В данной работе построено несколько моделей для описания парциального окисления природного газа воздухом - равновесная и полная трехмерная модели, которые учитывают явления переноса массы и энергии, а также химических превращений. Основной вывод сравнения моделей заключается в том, что полная численная модель достаточно хорошо предсказывает неполное окисление, а более простая равновесная модель — нет. В дальнейшем будут исследованы и представлены результаты численного моделирования кислородно-метановой конверсии.
Ключевые слова: обезуглероживание, установки производства метанола, моделирование химических реакций, вычислительная гидродинамика, горение, парциальное окисление.

Ибраев Н.Х., Селиверстова Е.В., Омарова Г.С., Ищенко А.А., Деревянко Н.А., Хамза Т.
Функционалды индодикарбоцианиндік бояғыштың фотоэлектрлік қасиеттері

Полиметин бояғыштарының химиялық құрылымының олардың спектрлік-люминесценттік және фотовольтаикалық қасиеттеріне әсері зерттелді. Бояғыш құрылымына функционалды топтарды енгізу жұтылу және флуоресценция жолақтарының батохромды ығысуына әкелетіні көрсетілген. Титан диоксидінің бетіне бояғыштарды адсорбциялау кезінде жартылай өткізгіш бетіндегі бояғыштардың агрегациясынан туындаған жолақтардың бір мезгілде кеңеюімен олардың спектрлерінің қызыл толқын ұзындығы аймағына ығысуы тіркелді. Молекулалардың қозған күйінің өмір сүру уақытының сәйкесінше 1 және 2 бояғыштар үшін 64 және 30%-ға төмендеуі тіркелді. Адсорбцияланған молекулалардың флуоресценциясының өмір сүру уақытын сөндіру электронның бояғыштан жартылай өткізгішке берілуінің нәтижесі болып табылады. Берілген қосылыстың TiO_2-де жақсы адсорбциялануына байланысты, зерттелетін бояғыштармен сенсибилизацияланған күн ұяшықтарының фотовольтаикалық параметрлерін өлшеу функционалды бояғыш үшін үлкен тиімділікті көрсетті.
Кілт сөздері: полиметиндік бояғыштар; функционалдық топтар; оптикалық қасиеттер; фотовольтаика.

Ибраев Н.Х., Селиверстова Е.В., Омарова Г.С., Ищенко А.А., Деревянко Н.А., Хамза Т.
Фотовольтаические свойства функционализированного индодикарбоцианинового красителя

Изучено влияние химического строения полиметиновых красителей на их спектрально-люминесцентные и фотовольтаические свойства. Показано, что введение функциональных групп в структуру красителя приводит к батохромному сдвигу полос поглощения и флуоресценции. При адсорбции красителей на поверхности диоксида титана был зарегистрирован сдвиг их спектров в область красных длин волн с одновременным уширением полос, вызванных агрегацией красителя на поверхности полупроводника. Зарегистрировано уменьшение времени жизни возбужденного состояния молекул на 64 и 30% для красителей 1 и 2, соответственно. Тушение времен жизни флуоресценции адсорбированных молекул является результатом передачи электрона от красителя к полупроводнику. Измерения фотовольтаических параметров солнечных ячеек, сенсибилизованных исследуемыми красителями показали большую эффективность для функционализированного красителя, что связано с более лучшей адсорбцией данного соединения на TiO_2.
Ключевые слова: полиметиновые красители; функциональные группы; оптические свойства; фотовольтаика.

Ершина А.К., Манатбаев Р.К., Байжұма Ж.Е.
Төрт қалақшалы Бидарье-1 турбинасынның жұмысы кезіндегі тұрақты ауа ағысының ағын өрісін тәжірибе арқылы зерттеудің нәтижелері

Жел қондырғыларының конструкцияларының алуан түрлілігі бар, бірақ жұмыс принципі бойынша оларды үш негізгі түрге бөлуге болады – желкенді (Savonius жел турбиналары), пропеллерлі және қанатты типті (Дарье аппараты). Қазіргі уақытта пропеллер типті жел турбиналары ең көп қолданылады. Олар өндірісте жақсы игерілген және көптеген елдерде шығарылады. Барлық басқа параметрлері тең болса, жел турбинасы өндіретін қуат жел дөңгелегі сыпыратын аумаққа пропорционалды. Сондықтан, мегаватттық пропеллерлі жел турбиналары ұзындығы 40 метр немесе одан да көп қалақтарға ие. Мұндай ұзын, нақты пішінді қалақтарды білікті инженерлік-техникалық персонал мен тиісті жабдықтары бар ұшақ зауыты ғана жасай алады. Жақында қанатты жел турбиналарына (Дарье жел турбиналары) қызығушылық пайда болды. Құрылымдық жағынан олар қарапайым және жел энергиясын алудың айтарлықтай жоғары коэффициентіне ие ($\xi=0.45$). Бұл жел қондырғыларының тиімділігінің жақсы көрсеткіші болғанымен, Әл-Фараби атындағы Қазақ Ұлттық

университетінің қызметкерлері осы коэффициенттің тиімді мәнін 1.3 – 1.6 есе арттыруға мүмкіндік беретін жел қондырғысының жаңа нұсқасын жасады. Бұл құрылғы Бидарье деп аталады. Бұл мақала Бидарье қондырғысының сипаттамасын, оның қалай жұмыс істеу принципін және жел қуатын пайдалану коэффициентін арттыру мүмкіндігін сипаттайды. Жұмыс істейтін зертханалық модельдің жел туннелінде сынау нәтижелері ұсынылған.

Кілт сөздері: жел турбинасы, Дарье, Бидарье, қос роторлы жел турбинасы, жел қуатын пайдалану коэффициенті.

Ершина А.К., Манатбаев Р.К., Байжума Ж.Е.
Результаты экспериментального исследования поля течения стационарного воздушного потока при работе четырехлопастной турбины Бидарье-1

Существует большое разнообразие конструкций ветротурбин, но по принципу работы их можно разбить на три основных типа – парусные (ветротурбина Савониуса), пропеллерные и крыловые (аппарат Дарье). В настоящее время наибольшее распространение получили ветротурбины пропеллерного типа. Они хорошо освоены производством и выпускаются во многих странах. При всех прочих равных условиях мощность, вырабатываемая ветротурбиной, пропорциональна ометаемой ветроколесом площади. Поэтому мегаватные пропеллерные ветротурбины имеют лопасти с длиной 40 и более метров. Изготовить такие длинные специфической формы лопасти под силу лишь авиационному заводу с квалифицированным инженерно-техническим персоналом и соответствующим оборудованием. В последнее время интерес появился к ветротурбинам крылового типа (ветротурбина Дарье). Конструктивно они более простые и имеют достаточно высокий коэффициент извлечения энергии ветра (ξ=0.45). Несмотря на то, что это неплохой показатель эффективности работы ВЭУ, сотрудники Казахского национального университета им. аль-Фараби разработали новую версию ветротурбины, которая позволяет увеличить эффективное значение этого коэффициента в 1.3-1.6 раза. Этот аппарат назван Бидарье. В настоящей статье излагаются описание конструкции Бидарье, принцип его работы и возможные методы увеличить коэффициент использования энергии ветра. Излагаются результаты испытания действующей лабораторной модели на аэродинамической трубе.

Ключевые слова: ветротурбина, Дарье, Бидарье, двухроторный ветродвигатель, коэффициент мощности ветра.

Скаков М.К., Толеубеков К.О., Бакланов В.В., Градобоев А.В., Акаев А.С., Бекмулдин М.К.
Жеңіл сулы ядролық реакторының балқымасының тұзағында кориумды салқындату әдісі

АЭС-тегі ауыр апаттың даму процесінде белсенді аймақтың балқуымен кориум пайда болады. Кориумның қоршаған ортаға шығуына кедергі келтіретін негізгі кедергілердің бірі - балқыманы оқшаулау құрылғысы немесе балқыманың тұзағы. Балқыманың тұзағы кориум параметрлерінің бақыланатын көлемде ұсталуын және салқындауын қамтамасыз ете отырып, сыни мәндерден шығуына жол бермеуі тиіс. Осы себепті балқыманың тұзақтарына ядролық реактордың активті аймағының балқымасын тиімді оқшаулауды қамтамасыз ету үшін салқындату әдістеріне қатысты елеулі талаптар қойылады. Ұсынылған мақалада кориумның сумен әрекеттесуі туралы эксперименттік зерттеулерге талдау жасалды, ол оны салқындату үшін балқытылған тұзақта кориум бетіне жіберілді. Жүргізілген жұмыстың нәтижесінде салқындатудың осы әдісінің төмен тиімділігіне байланысты бірқатар маңызды мәселелер анықталды, сонымен қатар оларды жоюдың мүмкін жолдары қарастырылды. Кориумды балқытылған тұзаққа салқындату әдісін оңтайландыру, сондай-ақ ұсынылған әдісті іс жүзінде жүзеге асыру және ВЧГ-135 стендін және «Лава-Б» қондырғысын қолдана отырып, оның тиімділігін талдау бойынша зерттеулер көлемі бойынша шешім ұсынылды.

Кілт сөздері: АЭС, ВВЭР, кориум, ауыр апат, балқыма тұзағы, ВЧГ-135 стенді, «Лава-Б» қондырғысы, қауіпсіздік, сутектің пайда болуы, бу жарылысы.

Скаков М.К., Толеубеков К.О., Бакланов В.В., Градобоев А.В., Акаев А.С., Бекмулдин М.К.
Способ охлаждения кориума в ловушке расплава легководного ядерного реактора

В процессе развития тяжелой аварии на АЭС с расплавлением активной зоны происходит образование кориума. Одним из главных барьеров препятствующим выходу кориума в окружающую среду является устройство локализации расплава или ловушка расплава. Ловушка расплава должна принять и не допустить выход параметров кориума за критические значения обеспечив его удержание в контролируемом объеме и охлаждение. По этой причине к ловушкам расплава предъявляются серьезные требования касательно методов охлаждения для обеспечения эффективной локализации расплава активной зоны ядерного реактора. В представленной статье проведен анализ экспериментальных исследований взаимодействия кориума с водой, которая подавалась на поверхность кориума в ловушке расплава для его охлаждения. В результате проведенной работы определен ряд существенных проблем, связанных с низкой эффективностью такого метода охлаждения, а также рассмотрены возможные способы их устранения. Предложено решение по оптимизации метода охлаждения кориума в ловушке расплава, а также по объему исследований по

возможности реализации предложенного способа на практике и анализа его эффективности с использованием стенда ВЧГ-135 и установки «Лава-Б».
Ключевые слова: АЭС, ВВЭР, кориум, тяжелая авария, ловушка расплава, стенд ВЧГ-135, установка «Лава-Б», безопасность, образование водорода, паровой взрыв.

Цыганов В. В., Шейко С. П., Сакипов К.Е., Касымов С.С.
Электрондық шығу жұмысы бойынша трибоқосылыстардың тозуға төзімділігін бағалау ерекшеліктері
Күрделі динамикалық жүктемемен үйкелістен кейінгі мысалда беткі қабаттың тозуы мен энергетикалық өнімділік күйі қарастырылған. Трибоқосылыстардың жұмыс істеу қабілетін және тозуға төзімділігін бағалауына талдау жүргізілген. Трибосимилярлық жүктеме сипатының өзгеруі беткі қабаттың энергия өндіретін күйін анықтайтындығы және электро ндарды бетке шығару жұмысының шамасы бойынша бағалануы мүмкін екендігі көрсетілген. Электрондардың шығуы жұмысының таралу шамасын талдау контактілі өзара әрекеттесу жағдайларының беткі қабаттың тозуға төзімділігі мен күйіне әсерін анықтайды. Пластикалық деформацияның әртүрлі дәрежесін алған беттің аймақтарын анықтауға мүмкіндік береді.
Кілт сөздері: тозу, трибошарнирлер, электрондардың шығу жұмысы, үйкеліс, беткі қабат.

Цыганов В. В., Шейко С. П., Сакипов К.Е., Касымов С.С.
Особенности оценки износостойкости трибосоединений по работе электронного вывода
Рассмотрено изнашивание и энергопроизводительное состояние поверхностного слоя на примере после трения со сложным динамическим нагружением. Проанализирована оценка работоспособности и износостойкости трибосоединений. Показано, что изменение характера нагружения трибосочленений определяет энергопроизводящее состояние поверхностного слоя и может быть оценено по величине работы вывода электронов на поверхность. Анализ величины распределения работы выхода электронов определяет влияние условий контактного взаимодействия на износостойкость и состояние поверхностного слоя. Позволяет определить участки поверхности, получившие разную степень пластической деформации.
Ключевые слова: износ, трибошарниры, работа выхода электронов, трение, поверхностный слой.

Жанабаев З.Ж, Ахтанов С.Н., Турлыкожаева Д.А., Усипов Н.М., Ибраимов М.К.
Эксцентриситеті талдау негізінде құрылған кластерлік маршрутизатор
Берілген жұмыста телекоммуникация саласына, атап айтқанда хабар тасымалдау саласына қатысты эксцентриситеттік кластерлік маршрутизатор ұсынылды. Бұл маршрутизатордағы хабарламалар желіге қосылған құрылғылар арасында онда көрсетілген маршрут бойынша пакеттер түрінде беріледі. Бұл желідегі әрбір түйінге маршруттауды тездететін бірегей мекенжай тағайындалады. Әрбір маршрутизатор түйіндердің есептелген эксцентриситеті арқасында маршруттау картасын құрайды, оның көмегімен кластердің логикалық мекен-жайы бойынша пакеттің физикалық бағытын таңдайды. Сонымен қатар, бағыттау картасы ақпараттың жоғалуын болдырмау үшін құрылғының регистрінде және жадыда сақталады. Осы кластерлік құрылғыны талдау үшін "UV-flower" модельдік желісіне фракталдық талдау жүргізілді және Цаллис пен Реньи ақпараттық өлшемдері есептелді.
Кілт сөздері: кластерлік маршрутизатор, эксцентриситет, күрделі желілер, кластерлерге бөлетін алгоритмдер, Цаллис және Реньи өлшемдері.

Жанабаев З.Ж, Ахтанов С.Н., Турлыкожаева Д.А., Усипов Н.М., Ибраимов М.К.
Кластерный маршрутизатор на основе анализа эксцентриситета
В данной работе разработан кластерный маршрутизатор на основе эксцентриситета, относящийся к области телекоммуникаций, в частности, к области передачи сообщений. Сообщения в этом маршрутизаторе передаются в виде пакетов по указанному в нем маршруту между устройствами, подключенными к сети. Каждому узлу в этой сети присваивается уникальный адрес, благодаря чему можно ускорить маршрутизацию. Каждый маршрутизатор формирует карту маршрутизации, благодаря рассчитанному эксцентриситету узлов, с помощью которого выбирается физический маршрут пакета по логическому адресу кластера. Кроме того, карта маршрутизации хранится в регистре и энергонезависимой памяти устройства для предотвращения потери информации. Для анализа этого кластерного устройства был проведен фрактальный анализ модельной сети 'UV-flower' и рассчитаны информационные размерности Цаллиса и Реньи.
Ключевые слова: кластерный маршрутизатор, эксцентриситет, сложные сети, алгоритмы делящие сети на кластеры, размерности Цаллиса и Реньи.

Саутбекова З., Трубицын А.

Реал осьті-симметриялы электрстатикалық айналардың траекториялық талдауының FOCUS CPM бағдарламасы: әдістер мен алгоритмдер

Электрондық айналардың конструктивті ерекшеліктерінің, атап айтқанда электродтар арасындағы саңылаулардың олардың электронды-оптикалық сипаттамаларына әсерін зерттеу есебі шешіледі. Аналитикалық параксиалды және сандық тәсілдердің артықшылықтарын біріктіретін есепті шешу әдісі сипатталған. Жұмыс авторлары әзірлеген және сипатталған әдісті жүзеге асыратын FOCUS CPM бағдарламалық қамсыздану ұсынылады. Үш электродты айна мысалында есептеулердің дәлдігін бағалау жүргізілген. Тоғыс орнының цилиндрлік электродтар арасындағы алшақтық шамасына тәуелділігі есептеліп, талданған.

Кілт сөздері: электрондық оптика, параксиалды оптика, электронды айна, сандық әдістер, траекториялық талдау.

Саутбекова З., Трубицын А.

Программа FOCUS CPM траекторного анализа реальных аксиально – симметричных электростатических зеркал: методы и алгоритмы.

Решается задача исследования влияния конструктивных особенностей электронных зеркал, в частности, зазоров между электродами на их электронно-оптические характеристики. Описывается способ решения задачи, сочетающий в себе преимущества аналитического параксиального и численного подходов. Представляется программное обеспечение FOCUS CPM, развитое авторами работы и реализующее описанный способ. Проводится оценка точности расчетов на примере трехэлектродного зеркала. Рассчитывается и анализируется зависимость положения фокуса от величины промежутка между цилиндрическими электродами.

Ключевые слова: электронная оптика, параксиальная оптика, электронное зеркало, численные методы, траекторный анализ.

INFORMATION
ABOUT AUTHORS

АВТОРЛАР ТУРАЛЫ
МӘЛІМЕТТЕР

СВЕДЕНИЯ
ОБ АВТОРАХ

Agelmenev, M.E. – Doctor of chem. sciences, Professor, E.A. Buketov Karaganda University, Karaganda, Kazakhstan. Scopus Authors ID: 6603494993, ORCID ID:0000-0002-4083-4443, amaxut58@gmail.com

Akayev, A.S. –Head of the Department of Non-reactor tests, Institute of Atomic Energy of the Branch NNC RK, Kurchatov, Kazakstan. Scopus Author ID: 57311044500

Akhtanov, S.N. – PhD, Researcher, teacher, al-Farabi Kazakh National University, Almaty, Kazakhstan. Scopus Author ID: 55672124000, ORCID iD: 0000-0002-9705-8000, sayat1986@gmail.com

Alpysbayeva, B.E. – PhD, Senior Lecturer, Department of Plasma Physics, Nanotechnology and Computer Physics, al-Farabi Kazakh National University, Almaty, Kazakhstan. ORCID ID: 0000-0001-7383-0708. Balausa.alpysbayeva@kaznu.kz

Amangeldi, N. – PhD, Associate Professor, L.N. Gumilyov Eurasian National University, Institute of Nuclear Physics, Kazakhstan. Scopus Author ID: 37065699200, ORCID ID: 0000-0002-9416-5425

Arkhipov, V.V. - Candidate of phys. and math. sciences, Associate Professor, General Physics Department, Moscow Institute of Physics and Technology (National Research University), Dolgoprudny, Russian Federation, ORCID ID:0000-0002-2148-1988, midav_73@mail.ru

Baizhuma, Zh.E. - Master (Eng.), PhD student, al-Farabi Kazakh National University, Almaty, Kazakhstan, Scopus Author ID: 57205433240, ORCID iD: 0000-0003-3692-2245, zhandos.baizhuma@kaznu.edu.kz

Baklanov, V.V. – PhD, First Deputy Director, Institute of Atomic Energy of the Branch NNC RK, Kurchatov, Kazakstan. SCOPUS Author ID: 1631518110

Baltabekov, A.S. - Candidate of technical sciences, Associate Professor, E.A. Buketov Karaganda University, Karaganda, Kazakhstan. Scopus Author ID: 35193461600, ORCID ID: 0000-0001-8829-2527

Bekmuldin, M.K. – PhD student, Semey University named after Shakarim; Head of the Laboratory of Experimental Thermophysics group, Institute of Atomic Energy of the Branch NNC RK, Kurchatov, Kazakstan. Scopus Author ID: 57321072600, ORCID ID: 0000-0002-6895-536X

Berdibekov, A.T. - PhD, Associate Professor, Colonel, Head of the Research Institute of Weapons and Military Equipment of the Military Research Center of the National Defense University named after the First President of the Republic of Kazakhstan – Elbasy, Nur-Sultan, Kazakhstan

Bratukhin, S.M. – Candidate of chem. sciences, Head of Information Security Department, E.A. Buketov Karaganda University, Karaganda, Kazakhstan, Scopus Authors ID: 24176883000, x86f@yandex.kz

Derevyanko, N. – Senior Researcher, Institute of Organic Chemistry, National Academy of Sciences of Ukraine, Kiev, Ukraine. Scopus Author ID: 35428560600, ORCID ID: 0000-0001-6474-9254

Dolya, A.V. - Master (Sci.), Major, Head of the Research Service of the Engineering and Technical Department of the Research Institute of Weapons and Military Equipment of the Military Research Center of the National Defense University named after the First President of the Republic of Kazakhstan – Elbasy, Nur-Sultan, Kazakhstan

Geza, V. – Doctor of phys.-math. sciences, Leading Researcher, Laboratory of multiphysical processes of the Institute of Numerical Modeling, University of Latvia, Riga, Latvia. Scopus Author ID: 25723093300, ORCID iD: 0000-0001-9395-0205, vadims.geza@lu.lv

Gradoboev, A.V. – Doctor of techn. sciences, Professor, Professor, Control and Diagnostics Department, Tomsk Polytechnic University (TPU), Tomsk, Russia. SCOPUS Author ID: 6506370250, ORCID ID: 0000-0002-2803-5972

Gruzin, V.V. Doctor of techn. sciences, Professor, Senior Researcher, Research Institute of Weapons and Military Equipment of the Military Research Center of the National Defense University named after the First President of the Republic of Kazakhstan – Elbasy, Nur-Sultan, Kazakhstan. Scopus Author ID: 57191036631, ORCID ID: 0000-0002-1128-5246

Guchenko, S.A. - Master (Sci.), Junior researcher, Research center "Ion-plasma technologies and modern instrumentation", E.A. Buketov Karaganda University, Karaganda, Kazakhstan. Scopus Author ID:5666979200, ORCID ID:0000-0002-9954-5478

Homko, A. – Master (Eng.), Leading Technologist- ENCATA LLC, Riga, Latvia. aleksandrs.homko@gmail.com

Ibraimov, M.K. - PhD, Professor, Head of the Solid State Physics and Nonlinear Physics Department, al-Farabi Kazakh National University, Almaty, Kazakhstan. Scopus Author ID: 57189617696, ORCID iD: 0000-0002-8049-3911, margulan.ibraimov@kaznu.kz

Ibrayev, N.Kh. - Doctor of phys.-math. sciences, Professor, Director of the Institute of Molecular Nanophotonics, E.A. Buketov Karaganda University, Kazakhstan. Scopus Author ID: 9333698600, ORCID ID: 0000-0002-5156-5015, niazibrayev@mail.ru

Ibrayeva, A. - PhD, Researcher, Institute of Nuclear Physics, Almaty, Kazakhstan; Nelson Mandela University, Port Elizabeth, South Africa. Scopus Author ID: 55637013100, a.d.ibrayeva@gmail.com

Ishchenko, A.A. – Doctor of chem. sciences, Professor, Corresponding member of the National Academy of Sciences of Ukraine, Head of the Department of Color and Structure of Organic Compounds, Institute of Organic Chemistry, National Academy of Sciences of Ukraine, Kiev, Ukraine. Scopus Author ID: 8338223800, ORCID ID: 0000-0003-2722-3944, al.al.ishchenko@gmail.com

Jakovics, A. – Doctor of phys.-math. sciences, Professor, Head of the Laboratory of multiphysical processes of the Institute of Numerical Modeling, University of Latvia, Riga, Latvia. Scopus Author ID: 8338223800, ORCID ID: 6602503350, 0000-0003-3410-5081; andris.jakovics@lu.lv

Kadir, M.F. – PhD student, Department of Plasma Physics, Nanotechnology and Computer Physics, al-Farabi Kazakh National University, Almaty, Kazakhstan. ORCID ID: 0000-0002-3976-5110, kadir.meruyert@gmail.com.

Kassymov, S.S. - Candidate of of phys.-math. sciences, Associate Professor, E.A. Buketov Karaganda University, Karaganda, Kazakhstan; Scopus Author ID: 57191039180, ORCID iD: 0000-0003-4979-9127, skasymov@mail.ru

Khamza, T. – Learner, Nazarbayev Intellectual School of Karaganda, Kazakhstan. takhminakhamza@gmail.com

Kharitonov, V. - Master (Eng.), Researcher - University of Latvia, Riga, Latvia. victorkharitonov1861@gmail.com

Laurinas, V.Ch. - Candidate of phys.-math. sciences, Associate Professor, Physical-Technical Faculty, E.A. Buketov Karaganda University, Karaganda, Kazakhstan. Scopus Author ID: 6504426206, ORCID ID: 0000-0001-7079-254X, vitas-laurinas@rambler.ru

Lisitsyn, V. - Candidate of phys. and math. sciences, Associate Professor, Professor General and Applied Physics Department, Voronezh State Forestry University named after G.F. Morozov**,** Voronezh**,** Russian Federation. ORCID ID: 0000-0002-2148-1988

Manatbaev, R.K. - Candidate of techn. sciences, Associate Professor, al-Farabi Kazakh National University, Almaty, Kazakhstan. Scopus Author ID: 55848346700, ORCID iD: 0000-0003-2151-2606, rustemmanatbayev@gmail.com

Matveev, N. - Doctor of Phys.-Math. Sciences, Professor, General and Applied Physics Department, Voronezh State Forestry University named after G.F. Morozov**,** Voronezh**,** Russian Federation. Scopus Author ID: 7006850538, ORCID ID: 0000-0001-9195-9580

Nemkayeva, R.R. – Master, Senior researcher, Al-Farabi Kazakh National University, Almaty, Kazakhstan. ORCID ID: 0000-0002-8782-703X, quasisensus@mail.ru

Omarova, G.S. - PhD, E.A. Buketov Karaganda University, Kazakhstan; Scopus Author ID: 56669661100, ORCID ID: 0000-0003-2900-2168, guldenserikovna@mail.ru

Polikarpov, V.V. - Master (Inf.), Leading Specialist, Ltd "NTL Kazakhstan*"*, Karaganda, Kazakhstan, ORCID ID: 0000-0003-0034-5458, bbprivet@rambler.ru

Potapov, A.A. – Doctor of phys.-math. sciences, Professor, Chief researcher, V.A. Kotel'nikov Institute of Radio Engineering and Electronics, Russian Academy of sciences, Moscow, Russia; IREE joint laboratory of fractal method & signal processing, Jinan University, Guangzhou, China. Scopus AuthorID: 56375460400, 56375460400; ORCID: 0000-0001-9864-3546

Rodin, L. – Doctor of chem. sciences, Leading Researcher, ENCATA LLC, Riga, Latvia. info@encata.eu

Rogulyova, M. – Graduated Engineer, Researcher, University of Latvia, Riga, Latvia. mrogulyova@gmail.com

Rymzhanov, R.A. - PhD, Senior Researcher, Institute of Nuclear Physics, Almaty, Kazakhstan; Joint Institute for Nuclear Research, Dubna, Russia. Scopus Author ID: 55648728100, r.a.rymzhanov@gmail.com

Sakipov, K.E. - Candidate of techn. sciences, Associate Professor, L.N. Gumilyov Eurasian National University, Nur-Sultan, Kazakhstan. Scopus Author ID: 57197722422, ORCID iD: 0000-0003-2477-3879, ksakipov@mail.ru

Sautbekova, Z.S. – PhD student, Al-Farabi Kazakh National University, Almaty, Kazakhstan. Scopus Author ID: 55946640100, edrez@inbox.ru

Seliverstova, E. – PhD, Senior Researcher, Institute of Molecular Nanophotonics, E.A. Buketov Karaganda University, Kazakhstan. Scopus Author ID: 35323255400, ORCID ID: 0000-0002-9507-8825, genia_sv@mail.ru

Sheyko, S.P. - Candidate of techn. sciences, Associate Professor, Zaporizhzhia National University, Zaporozhie, Ukraine. Scopus Author ID: 23095863300, ORCID iD: 0000-0001-5761-4263, sheyko.s@mail.ru

Shishulin, A.V. – Master (Sci.), Junior Researcher, Pleiades Publ., Ltd, Moscow, Russia. Scopus AuthorID: 57191571862; ORCID: 0000-0003-2370-5313; chichouline_alex@live.ru

Shishulina, A.V. – PhD, Associate Professor, R.E. Alekseev Nizhny Novgorod State Technical University, Nizhny Novgorod, Russia; N.I. Lobachevsky Nizhny Novgorod State University, Nizhny Novgorod, Russia. Scopus AuthorID: 6602952373

Skakov, M.K. – Doctor of phys.-math. sciences, Professor, Academician of the KazNANS, Chief Researcher of NNC RK, Kurchatov, Kazakstan. SCOPUS Author ID: 6506859122

Smirnov, V.– PhD, Senior researcher, Forschungszentrum Jülich (FZJ), Jülich, Germany. Scopus Author ID: 35594115900, v.smirnov@fz-juelich.de

Soldatkhan, D. – PhD student, OP «Nuclear physics», L.N. Gumilyov Eurasian National University, Nur-Sultan, Kazakhstan. Scopus Author ID: 57768566200, ORCID ID: 0000-0001-7981-4100, soldathan.dauren@mail.ru

Toleubekov, K.O. – PhD student, Semey University named after Shakarim; Engineer of the Laboratory of Experimental Thermophysics, Institute of Atomic Energy of the Branch NNC RK, Kurchatov, Kazakstan. ORCID ID: 0000-0001-8731-363X

Trubitsyn, A.A. – Doctor of phys.-math. sciences, Professor, Department of Industrial Electronics, Ryazan State Radio Engineering University, Russia. Scopus Author ID: 6604053991, WoS ResearcherID: A-6806-2014, assur@bk.ru

Tsyganov, V.V. - Doctor of techn.sciences, Academician of the Academy of Technical Sciences of Ukraine, Corresponding Member of the Ukrainian Academy of Tribotechnics, Associate Professor, Metal cutting machines and tools Department, Zaporizhzhia Polytechnic National University, Zaporozhie, Ukraine. ORCID iD: 0000-0001-5682-7005, tsyganov705@gmail.com

Turlykozhayeva, D.A. – Master (Phys.), Researcher, Lecturer, al-Farabi Kazakh National University, Almaty, Kazakhstan. ORCID iD: 0000-0002-7326-9196, abdikumarovna.d@gmail.com

Tvardovsky, A.N. – Master (Eng.), Engineer, Research center "Ion-plasma technologies and modern instrumentation", E.A. Buketov Karaganda University, Karaganda, Kazakhstan

Ussipov, N.M. - Master (Phys.), Researcher, Lecturer, al-Farabi Kazakh National University, Almaty, Kazakhstan. Scopus Author ID: 57226319348, ORCID iD:0000-0002-2512-3280, unurzhan55@gmail.com

Volkov, A. – Candidate of phys.-math. sciences, Leading Researcher, Lebedev Physical Institute of the Russian Academy of Sciences, Moscow, Russia; Joint Institute for Nuclear Research, Dubna, Russia. Scopus Author ID: 55938916900, a.e.volkov@list.ru

Yergaliuly, G. – PhD, Senior lecturer, L.N. Gumilyov Eurasian National University, Nur-Sultan, Kazakhstan. Scopus Author ID: 57216951648; ORCID ID: 0000-0002-7443-8561

Yershina, A.K. – Doctor of phys.-math. sciences, Professor, Kazakh National Women's Pedagogical University, Almaty, Kazakhstan. Scopus Author ID: 55849381800, ORCID iD: 0000-0002-6811-3904, 123ainakul.yershina@gmail.com

Zageris, G. – Master (Phys.), Researcher, Laboratory of multiphysical processes of the Institute of Numerical Modeling, University of Latvia, Riga, Latvia. Scopus Author ID: 57203135033; ORCID iD: 0000-0002-1419-311X, girts.zageris@lu.lv

Zhanabaev, Z.Zh. – Doctor of techn. sciences, Professor, al-Farabi Kazakh National University, Almaty, Kazakhstan. Scopus Author ID: 15840905700, ORCID iD: 0000-0001-5959-2707

GUIDELINES FOR AUTHORS

Eurasian Physical Technical Journal (Eurasian phys. tech. j.) is a peer-reviewed open access international scientific journal publishing original research results on actual problems of technical physics and other related fields. Since 2004 «Eurasian phys. tech. j.» is published in English.

Acceptance of the manuscript for publication in the Eurasian phys. tech. j. is carried out online through website - https://phtj.buketov.edu.kz/index.php/EPTJ. Authors should check that their submissions meet all of the following requirements, as submissions may be returned to authors that do not comply with these guidelines.

Scientific article topic and content

A scientific article should contain the results of original scientific research previously unpublished and not intended for publication in other publications.

Manuscript of the article should contain at least 75% of the original text.

All articles are published **in English in 4 scientific areas of physics: Energy, Engineering, Materials Science, Physics and Astronomy.**

Publication Ethics and Malpractice Statement

Submission of an article to the Eurasian phys. tech. j. implies that the paper described has not been published previously, that it is not under consideration for publication elsewhere, that its publication is approved by all authors and tacitly or explicitly by the responsible authorities where the paper was carried out, and that, if accepted, it will not be published elsewhere in the same form, in English or in any other language, including electronically without the written consent of the copyright holder. In particular, translations into English of papers already published in another language are not accepted.

For information on Ethics in publishing and Ethical guidelines for journal publication see http://www.elsevier.com/publishingethics and http://www.elsevier.com/journal-authors/ethics.

The Eurasian phys.tech.j. strictly adheres the Code of Conduct of the Committee on Publication Ethics (COPE), and follows the COPE Flowcharts for Resolving Cases of Suspected Misconduct (http://publicationethics.org/files/u2/New_Code.pdf).

To verify originality, your article may be checked by the originality detection service Cross Check http://www.elsevier.com/editors/plagdetect.

Pre-publication process

Authors are responsible for the content of their publications. No other forms of scientific misconduct are allowed, such as plagiarism, falsification, fraudu-lent data, incorrect interpretation of other works, incorrect citations, etc. Authors are obliged to participate in peer review process and be ready to provide corrections, clarifications, retractions and apologies when needed. All authors of a paper should have significantly contributed to the research.

Reviewers should provide objective judgments and should point out relevant published works which are not yet cited. Reviewed articles should be treated confidentially. The reviewers will be chosen in such a way that there is no conflict of interests with respect to the research, the authors and/or the research funders.

Editors have complete responsibility and authority to reject or accept a paper, and they will only accept a paper when reasonably certain. They will preserve anonymity of reviewers and promote publication of corrections, clarifications, retractions and apologies when needed.

The acceptance of a paper automatically implies the copyright transfer to the Eurasian phys. tech. j.

All submitted papers will the sent for reviewing to leading experts in the given area.

The Editorial Board of the Eurasian phys. tech. j. will monitor and safeguard publishing ethics.

The editors reserve the right to accept or reject manuscripts.

The article and all documentation must be identified by the name of the 1st author: Akhmetov AA_et al_paper; Akhmetov AA_et al_fig.1; Akhmetov AA_et al_Cover letter; …

The article text must be formatted according to the **Template**, font - Times New Roman, size -11 pt; line spacing-single; alignment-in width, see https://phtj.buketov.edu.kz/index.php/EPTJ/about/submissions#authorGuidelines

An article should consist:

Title: includes a separate line on the left the **UDC** index, Title of the article, information about the authors-surname and initials, name of institution, city, country, e-mail of a corresponding author. The author* who submitted an article for publication will be considered as a corresponding author.

Abstract should consist of at least 5-6 sentences, not exceeding 200-250 words without formula, references, abbreviations. An abstract is a short and powerful summary that describes the focus and subject of a research paper. It could contain the information about why the research study was done, background, what the methodology was and something about the findings of the author(s).

Keywords: at least 3-10 basic terms or short phrases used in the article.

The text should be divided on structural parts: Introduction, Main part (Theoretical part, Methods and materials or Experimental technique), Results and Discussion, Conclusions.

Conclusions: formulating main results; a comparison of the results with the existing data on this topic; assessment of scientific novelty and practical value of the results.

Acknowledgments or Funding may be shown at the end of the article text, before References.

References: a bibliographic list is compiled according to the requirements:
- Books, abstracts, patents: Surname and initials of the authors (it is enough to indicate the first three or one surnames, et al), *Title of the book* in italics, publish house or city, year and total number of pages.
- Journals, collections of papers, conference proceedings - Surname and initials of the authors (the first three are enough), the title of the article, the *Title of the journal* in italics (you can use the abbreviated title), city and / or country, year, volume, issue number, pages of the "begining and end" (pp. … - … .).
- Internet links also must to indicated the authors, the title and URL

The authors should represent References according to the requirements of international journals on physics, but should to consult preliminarily for standard abbrevi¬ations of journal's names. More information on references guidelines for journal publication you can see in Harvard reference system - http://www.emeraldgrouppublishing.com/authors/guides/write/harvard.htm?part=2/

All references must be numbered in the text (for example, [1], [2-4]) and listed in numerical order.

All abbreviations and acronyms, with the exception of obviously well-known, should be deciphered at first use in the text.

Equations in your paper have to be written using the Microsoft Equation Editor or the MathType.

Tables, numbered and titled, should be inserted into the text (Times New Roman, size - 10 pt) or have been presented as an appendix at the end of the article.

Figures should be prepared in a digital form suitable for direct reproduction. Figures shall be submitted on the separate sheets or can be included into the text.

The manuscript volume, including text, formulas, figures, bibliography, should not exceed 12 pages including tables, figures (no more than 8-10) and references (no more than 30-35) of text typed on a computer using Microsoft Word editor. The overview article should not exceed 20 pages with no more than 15 figures.

List of required documents

The following files must be uploaded to the journal's website:

1. Text of the article, with pictures (*.doc);
2. Figure, Picture, Photo (fig1.jpg, fig2.pcx, …);
3. Figure captions (*.doc);
4. A **Cover letter** - from a university, research institute or an organization licensed to conduct research activities, must be issued on an official letterhead and / or certified by the organization seal. The management officially confirms by this letter that the article (the title of the article and the names of the authors are indicated in English) doesn't contain any information constituting state or commercial secrets, and the article can be published in the Open Press. Authors must upload a copy of the signed Cover Letter in PdF format to the Journal website.

It's necessary to upload by separately 2 files in English (and in Russian for authors from Russia, and in Kazakh for authors from Kazakhstan):

5. **Article's data**: Surname and initials of the authors, the article title, abstract, keywords.
6. **Information about each co-author**: full name, academic degree, academic title, place of work or study, title of organization, city, country, SCOPUS Author ID or ORCID iD; and contact details (e-mail, phone).

7. **Receipt of payment.** Authors should pay for the publication only after receiving notification about a positive decision of the reviewers.